final report

Project code: A.TEC.0123

Prepared by: Jonathan Cook, Fiona Anderson
Scott Automation and Robotics, Murdoch University

Date published: 18 May 2017

PUBLISHED BY
Meat and Livestock Australia Limited
Locked Bag 991
NORTH SYDNEY NSW 2059

Beef and Lamb OCM with CT in situ further development

Final Report – For Public Release

Meat & Livestock Australia acknowledges the matching funds provided by the Australian Government to support the research and development detailed in this publication.

Abstract

A CT scanner was purchased and installed into a purpose-built room situated in a beef and lamb processing facility. A range of red meat industry applications were then evaluated to understand how the technology fits into the industry's automation and objective carcase measurement sensing framework. CT technology offers an opportunity for tasks requiring the 3D information that can't be found with standard x-ray imaging. This involved initial trials of lamb, beef and viscera, before focussing on beef grading and automation. Trials were conducted and algorithms written to predict the intramuscular fat content in beef striploins with high precision (R^2 = 0.86, RMSE = 2.01). These trials investigated a number of different scanning protocols to understand what would be required from an industrial, on-line CT scanner. There was no significant drop in precision between the 'high-speed' and 'high-quality' scan protocols used and between thin (0.6mm) and moderate (3mm) slice widths. There was also a significant ($p<0.05$) difference in intramuscular fat content between the cranial and caudal ends of the striploins. This presents a possible value proposition in CT's ability to grade along the entire length of a muscle. Algorithms were also written for a number of beef automation tasks, including rib 1 junction identification, spine cut location, chine removal and fat trim profiling. The knowledge obtained in this project will now be used to inform the specifications for an on-line CT scanner capable of operating in an abattoir. The algorithms will also be further developed with such a scanner for commercially-installed projects. CT presents a significant opportunity to the red meat industry and can be seen as a 'quantum leap' improvement over currently available sensing technologies. This project has demonstrated this and provided a key stepping stone towards commercial implementation.

Executive Summary

A purpose-built CT scanning room was designed and constructed at a beef and lamb processing facility. A helical CT scanner was then procured, installed and commissioned successfully. Following this, a set of initial trials were conducted investigating scans of lamb, beef and viscera. After evaluating the results of this work, a decision was made to focus efforts upon the applications of muscle isolation and composition analysis – both pivotal for enabling automation as well as objective carcase measurement.

Some initial trials were conducted on bone-in and boneless ribsets and striploins to investigate these applications further. Initial algorithms were written which were able to isolate the *longissimus dorsi* muscle automatically. The factors influencing composition analysis were investigated, including effects such as partial voluming, the variability in HU ranges for different tissue types, and the effect of CT scanner hardware parameters. Based on these findings, a focussed set of trials investigating the determination of intramuscular fat content in beef striploins was proposed. A researcher from Murdoch University (Fiona Anderson) was then contracted to assist in the experimental design and data analysis for these trials as she had previously conducted similar work in lamb. On top of modelling intramuscular fat content from CT data, a range of commercial factors were also to be investigated, including different scan settings and different points of the muscle.

Fifty-two striploins were sourced for the trials. Their lengths and MSA grading data were recorded before cutting a 6cm portion off each end. These portions were then denuded of any fat and adjacent muscle groups, leaving the isolated *longissimus lumborum* muscle. The striploins were then CT scanned with two different scan settings – a 'high-quality' and a 'high-speed'. The 6cm portions were then frozen and sent to Murdoch for chemical testing. Models were then built predicting intramuscular fat content based on the average and standard deviation of the intensity values. The effect on the accuracies of the models between the two scan settings was compared as well as the effect of using three different slice widths – 0.6mm, 3mm and 6mm. Only moderate precision was achieved (R^2 = 0.31, RMSE = 2.40). Despite the best efforts to cover a wide range of marbling scores, there was a distinct lack of high-marbled samples in the trialling set. Another twelve high-marbled striploins were then sourced and scanned with the same methodology to include in the dataset. Furthermore, another modelling algorithm was trialled whereby pixel intensities were adjusted based on neighbourhood information. These two factors resulted in a significant increase in precision (R^2 = 0.86, RMSE = 2.01). It was also found that there was little difference between the 'high-quality' and 'high-speed' scan settings. There was little drop in precision between 0.6mm and 3mm slice widths, but a larger drop when using 6mm slices. This information has direct positive implications for the requirements of a CT scanner for on-line beef IMF determination. The caudal portion of the eye muscle was also shown to have significantly more (1.97%, $p<0.05$) intramuscular fat than the caudal portion. Fiona's paper on this work is attached to this report in its entirety as an appendix.

Further to these trials, algorithms were written for various automation tasks which aren't currently possible using DEXA. Such tasks present a unique opportunity for CT technology and include chine removal, fat trim, rib 1 junction identification and spine cut location. These were also assessed with both high-quality and high-speed scan data to again understand the requirements of an automation-focussed CT scanner.

The knowledge and algorithms developed throughout the course of this project will now be applied to direct commercial projects. This involves evaluating and/or developing CT imaging technology which is able to meet the specifications defined in this project while operating reliably within an abattoir processing environment. The algorithms and trialling methodologies developed in this project will feed into these directly.

A key opportunity area for CT technology is with respect to eating quality grading. Objective measurement of eating quality measures is vitally important to the industry, particularly with the advent of objective lean meat yield measurement systems. Moving forward, this will involve re-examining the modelling of intramuscular fat content in lambs using the learnings from this project. This is something of high-value to the lamb industry in particular given the current lack of eating quality metrics.

CT presents a significant opportunity to the red meat industry and can be seen as a ‘quantum leap’ improvement over currently available sensing technologies. This project has demonstrated this and provided a key stepping stone towards commercial implementation. Work is now commencing towards translating these outcomes into real-life, production applications in beef and lamb.

Table of Contents

1 Background

Scott Technology has successfully developed single energy x-ray (SEXA) and dual energy x-ray (DEXA) full carcase systems for the meat processing sector. In addition to driving cost effective automation solutions, the x-ray technology also is at the cusp of providing eating quality, food safety inspection and supply chain information for the Australian red meat sector. Parallel developments around DEXA to provide an entry point into objective carcase measurement uses CT images as the Gold Standard for developing and calibrating DEXA algorithms. Furthermore, the 3D information available from CT imaging enables automation and processing not currently achievable using x-ray absorptiometry.

In this project Scott will continue to develop CT knowhow by moving the CT developments from a research/laboratory type setting to an in-situ, at line, processor location.

2 Project objectives

2.1 Objective 1:

Develop and demonstrate Australian CT algorithms for various supply chain objective measurement uses, including eating quality (MSA) food safety inspection, and advanced automation.

2.2 Objective 2:

For each of the Outcome 1 algorithms developed and proven, identify the required CT hardware specifications as well as a ‘measure everything’ CT scanner.

2.3 Objective 3:

Produce indicative 3D drawings of a proposed beef and lamb CT system(s) within a host site.

3 CT Room Build and Installation

The first task in the project was to source an appropriate second-hand CT scanner within budget, available for purchase and with a reasonable warranty. A Siemen’s Sensation 64 CT scanner was found which met these conditions and was purchased (Figure 1).

A host site was selected where the CT scanner would be installed. This site possessed a number of favourable characteristics which underpinned its selection. First and foremost, it is a large dual-species (beef and lamb) processing plant meaning convenient access to meat samples at various stages of processing as required. It was also located conveniently with respect to access by SCOTT personnel.

A custom room was then designed to house the CT scanner. This room had to be appropriately shielded and built from scratch (Figure 2 - Figure 5). Appropriate radiation licenses and compliance also had to be arranged.

Figure 1 - The Siemens Sensation 64 CT Scanner - marketing image, previous installed location and stored in the Sydney warehouse (anticlockwise from top).

Figure 2 - CT room location (left) and construction of panelling with lead shielding (right)

Figure 3 - Inside CT room once panelling complete (left), entrance to control room (middle) and entrance to CT room (right)

Figure 4 - Installation of CT scanner (left, middle) and electrical rack in control room (right)

Figure 5 - Completed CT room inside (left) and outside (right)

4 Initial Trials

With the CT scanner installed, a broad range of scans were completed to assess the technology at a high-level and help define particular areas of focus for the project moving forward. These scans included scanning a whole lamb carcase, three beef sides (as intact as possible) and some viscera samples.

4.1 Lamb

4.1.1 Overview

- *Lamb carcase grading currently occurs using dentition, hot standard carcase weight and subcutaneous fat depth at a grading site on the 12th rib - which was clearly visible in the scans observed.*

- *While determination of marbling in lambs isn't currently assessed, industry is investing in assessing its potential to add value and what technologies may enable this. From scans performed thus far, CT looks to be a viable technology in this space.*

- *While the helical CT scanner used for the trials is unable to reach target scanning speeds required for single unit, 100% inspection, in-line lamb applications, the data may be artificially down-sampled. This allows us to simulate faster scanning to identify the fastest speed allowable for any given application and provides data to design the required CT solution.*

- *The sample was scanned at a number of different speeds and energies to identify the requirements for a given application.*

- *Initial visual analysis suggests potential for CT to be used for cut placement, identification of muscle seams, identification of internal muscle contaminants and current grading measures. There is also the potential to assess measures not currently performed by human operators but may benefit the industry in areas such as eating quality.*

- *Image quality achieved with whole carcases enables the potential to perform multiple operations with one CT scan (e.g. cut placement, grading and identification of internal muscle contamination).*

4.1.2 Lamb Study

Scanning of lamb carcasses was relatively simple as a complete carcass fits comfortably inside the field of view of the CT machine (Figure 6). Scan quality achieved was excellent - most notably the smaller skeletal frame did not give any beam hardening artifacts as in some beef scans (this issue is explained in section 4.2.2 - Beef Study). There was generally good definition between fat, muscle seams and skeletal features, with excellent results for the subcutaneous fat to bone area used for grading at the 12th rib.

Figure 6 - Lamb carcass prepared on Helical CT Scanner

Eye-muscle size is currently identified indirectly through estimation using a number of grading indicators. CT technology is able to measure this directly for any given carcase (see Figure 7).

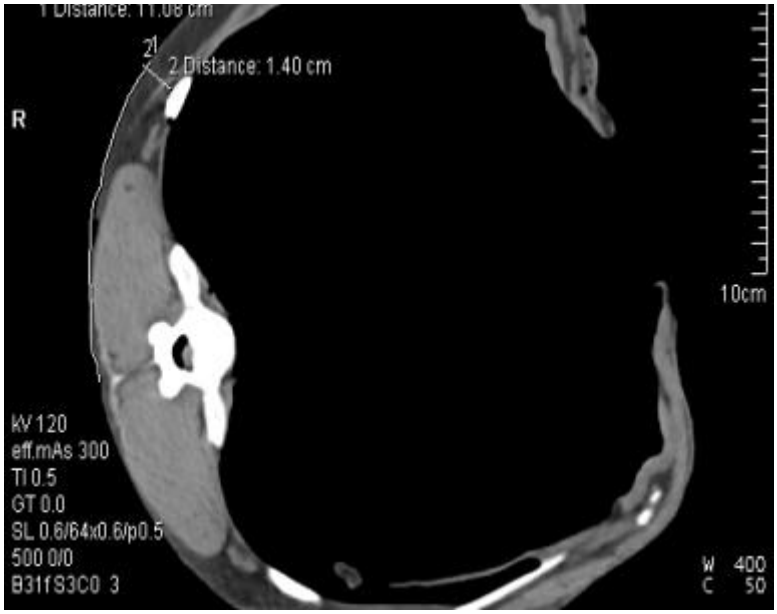

Figure 7 - Helical CT image of a Lamb Middle; clearly shows rib bones, the spine, the eye muscle as well as subcutaneous fat depth at rib 12.

Marbling is not currently part of the manual grading process for lamb, although industry is investing quite heavily in investigating what technologies may be suitable for this (e.g. hyperspectral imaging) and the value-adding opportunities which exist. The potential for characterising marbling using CT is quite promising and this project may present a valuable opportunity to investigate this further. Given that lack of beam-hardening effects experienced, there's a potential to couple grading measures, marbling and cut placement with one CT scan for an in-tact carcase.

Furthermore, the 3D structural information present can serve as an enabler for further primal processing of lamb. The definition between fat and muscle (Figure 8Figure 11) may serve to drive boneless automation that is not currently possible using available sensing methods (e.g. DEXA).

The system's scan rates were also trialled, with the fastest scan achieved for a complete carcass at approximately 55mm/s. If a typical 'line speed' for a lamb processing abattoir is 8 carcasses per minute, and a complete carcass scan length is 1500mm, the scan rate needs to be approximately 200mm/s; almost four times the tested peak scan rate for this system. It is possible to down-sample the data to emulate faster scanning speeds however to still assess how fast we'd be able to scan and while retaining the required level of accuracy for a given application.

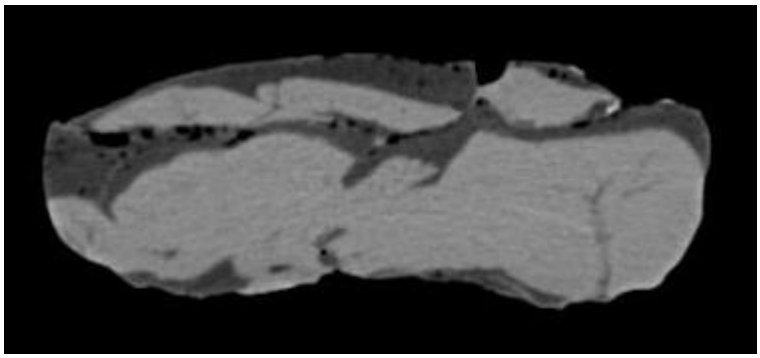

Figure 8 - Helical CT images of a Lamb Boneless Chump. The difference between the fat and lean is clearly visible.

4.2 Beef

4.2.1 Overview

- *As with lamb, initial trials aimed at keeping the carcase as 'in-tact' as possible to allow analysis of as many attributes and cut placements as possible. Initially quarters were attempted, then with the forequarter split in half down the middle with a caudocranial cut to allow each piece to be completely within the CT scanner's field of view. An Ox, an old cow, and a bull were scanned in this manner.*

- *Beam hardening – an effect which produces radial 'streaks' through an image – was encountered in samples containing ribs. Samples containing only the spine however, appear to be free of this artefact.*

- *Even with beam hardening effects, isolation of bone structure was still possible, notably at the rib 1 junction site which is a key point for scribing operations.*

- *Beam hardening effects however did affect the visual presentation of the eye muscle with these scans. The magnitude of the effect of these artefacts in assessing carcase attributes though shall be investigated in the next milestone phase as it may be found that, while quite visible to the eye, it doesn't impede calculations to a significant degree. If this is the case, multiple operations may be possible from one CT scan for beef (e.g. cut placement, grading and internal muscle contamination).*

- *A set of scans were taken on short loin and rib set primals. The carcase numbers for these samples was logged and their corresponding grading scores isolated. They were scanned bone-in and boneless.*

- *A number of different parameter configurations, including a 'line speed' one, were decided upon based on early trials and all samples were scanned with each configuration. This allows us to identify how 'fast' we can/need to scan for a given application for designing a purpose-built system.*

- *A number of third party software packages were trialled to enable manual analysis of the results. Preliminary analysis with the selected piece of software suggests that bone:lean:fat composition and marbling is able to be calculated from the trial data.*

4.2.2 Beef Study

As with the lamb scans, the initial plan was to keep the beef samples as intact as possible to maximise the number of attributes and cuts which could be evaluated. Thus, quarters were first investigated (Figure 9).

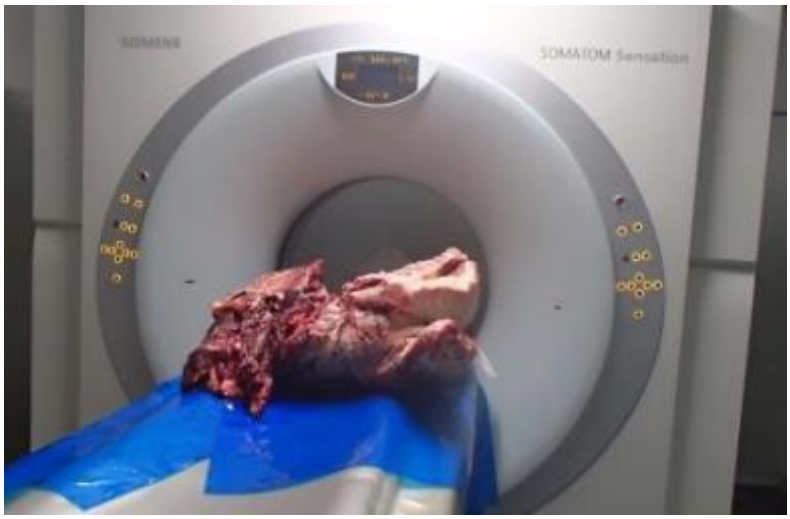

Figure 9 - Beef quarter prepared for Helical CT scanning.

The scan range of the system, in both distance and time, is restricted by heat dissipation of the x-ray tube. Thus a trade-off must be made between duration of scan and energy levels (equating to image quality), a balance which is bounded by the machine firmware and software to prevent damage to the system. Detailed understanding of these technology limitations will thus be applied in later milestones when specifying what an on-line CT scanning solution will look like for a given application.

For the cow and bull sides, the forequarter was split in half to allow scanning as per Figure 10. This was done for efficiency purposes along with maintaining a craniocaudal scan direction, which would be the most likely orientation for an on-line system.

Figure 10 - Forequarter split into Dorsal (left) and Ventral samples for scanning. Hindquarter scanned intact (right).

One phenomenon of note was the occurrence of beam hardening in some of the scans (see Figure 11). When an x-ray beam encounters dense materials, in this case thick sections of rib bone, lower energy photons are absorbed by the material, resulting in a higher average energy for the transmitted beam at that point. When the beam is measured by a detector, the effect is as if the beam had not encountered as much attenuation due to the higher average energy. The beam hardening was prevalent in scans of any large or small sized beef product containing thick rib bones, regardless of scan times or energy levels used.

This effect was found even with the slowest and highest energy scans possible with the machine. The degree to which this impairs the ability to perform certain applications (e.g. bone, meat and fat composition, marbling etc) is to be investigated in the next milestone. The factors which characterise this effect (e.g. bone thickness, carcase age, ox vs bull vs cow etc) will also be investigated. This will allow us to identify the practical significance of the effect and what post-processing may be applied to counter it. As later described, a number of physical aspects were also able to counter the effect.

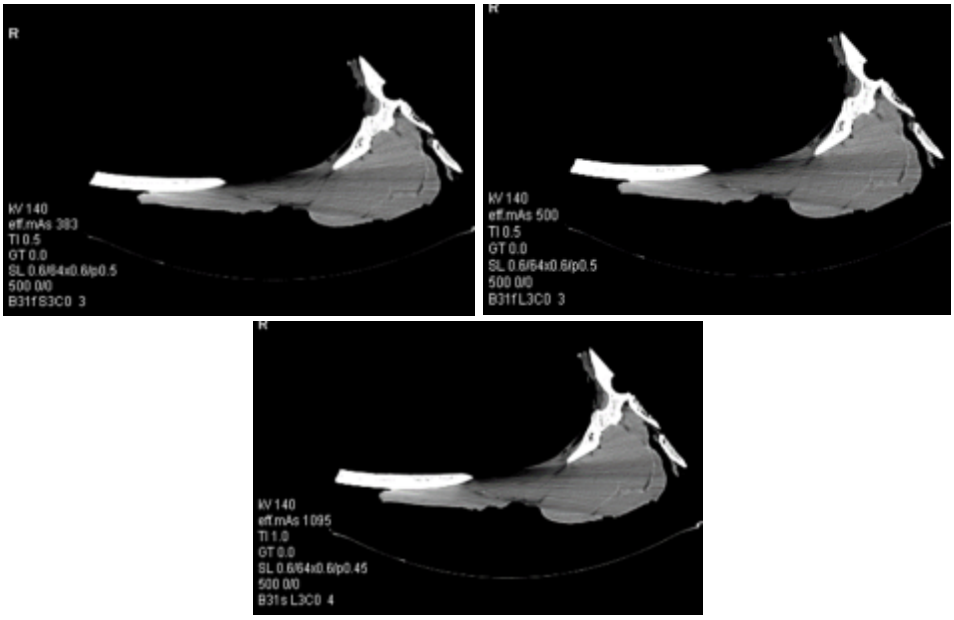

Figure 11 - Images above show difference with increasing mAs (eff. mAs) and rotation time (TI). Note the hardened beams showing as radial lines from the edge of the rib and extending through the eye muscle.

Figure 12 shows a number of different slices as the CT scanner moves from between ribs to the middle of a rib. It can be seen that when no ribs are in the scan, there appears to be little presence of beam hardening. As soon as the rib comes into the slice though, the effect is propagated through much of the adjacent muscle.

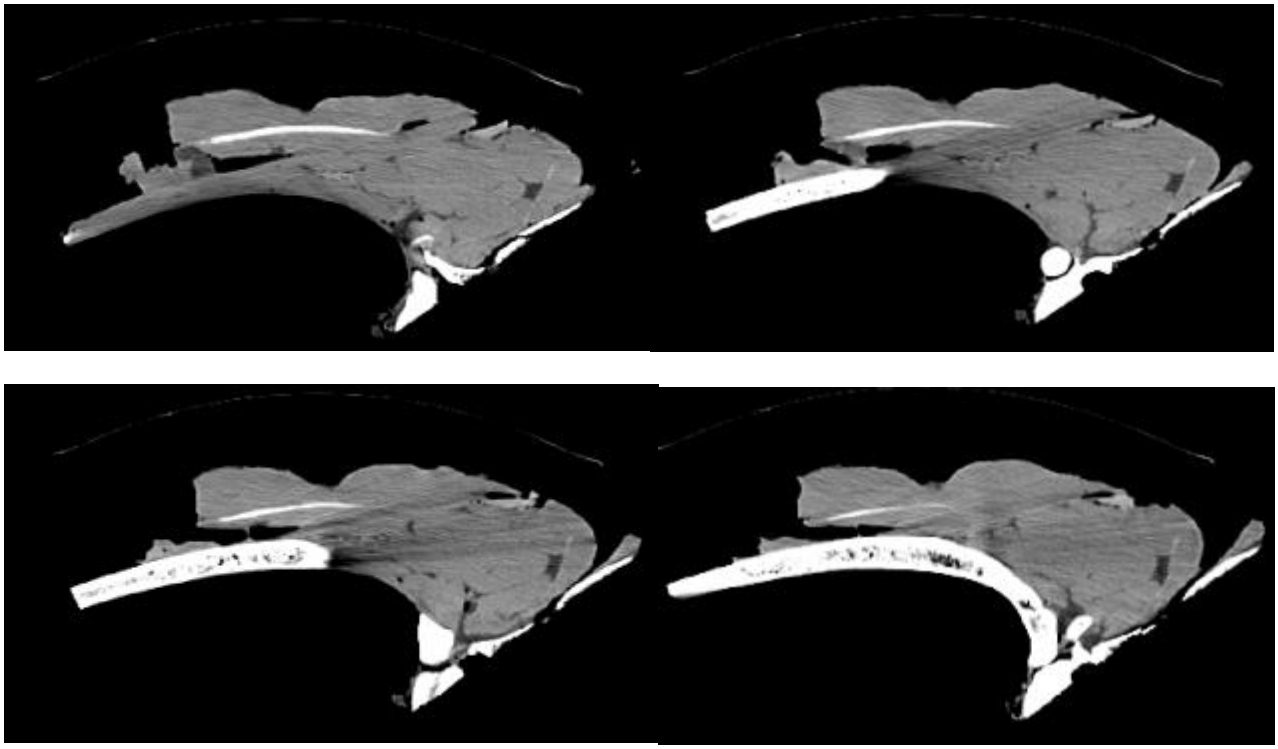

Figure 12 - Presentation of beam hardening through different slices around a rib

Scans of the hindquarters however seemed free of this effect (see Figure 13). This confirmed that this issue seems to present only when the ribs are present and not with just the spine.

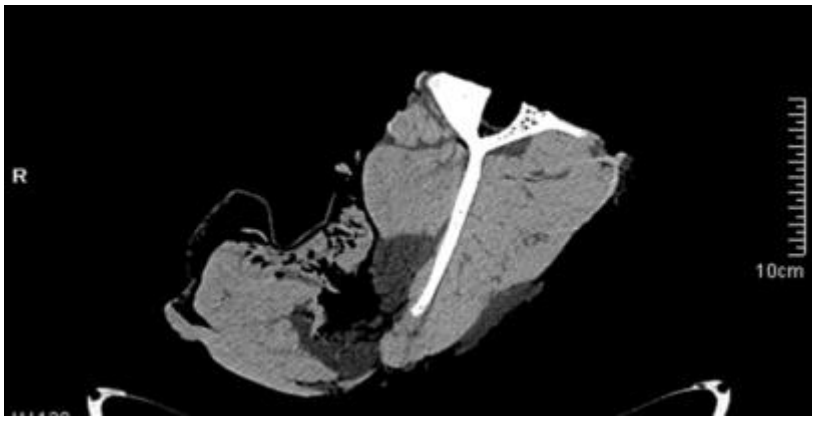

Figure 13 - In hindquarter sections, the beam hardening was not present, even at 'line speed' trial scan rates (160 sides per hour at 1000mm scan length)

Even with the beam-hardening effects experienced, separation of bone from fat and lean was still possible, even with the 'line-speed' scan parameters. The costochondral joint at rib 1 is a key point for scribing operations and can be challenging to isolate in DEXA images. This was found to be visible even with the 'line-speed' scan parameters (see Figure 14 and Figure 15).

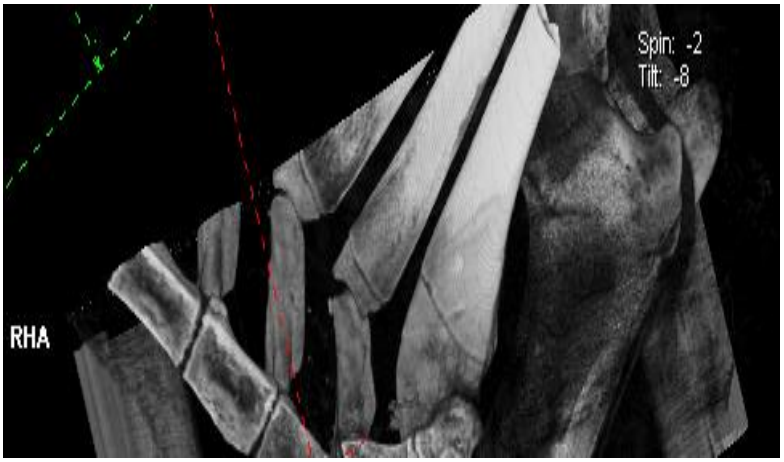

Figure 14 - Isolation of bone around rib 1 costochondral joint for a 195kg bull with 'line-speed' scan parameters

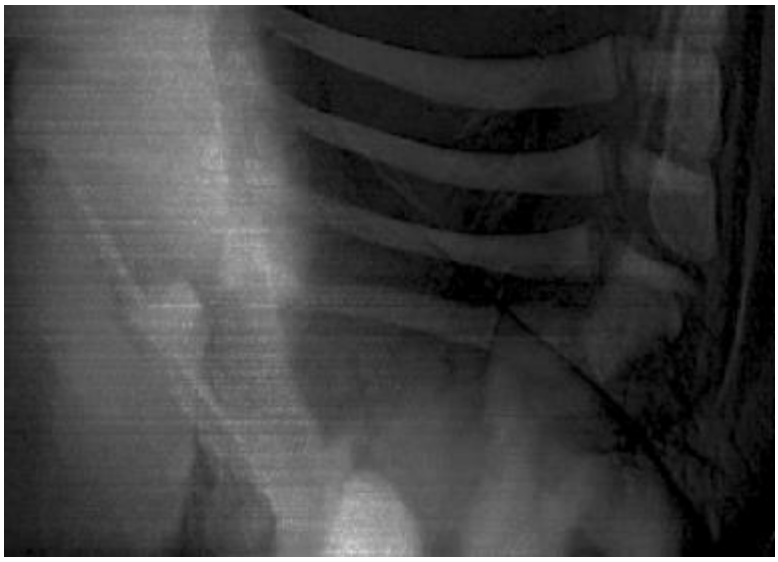

Figure 15 - By comparison, DEXA image around the rib 1 junction for a 187kg obtained at Swift Dinmore

This suggests that even with beam-hardening effects, CT is still a viable option for determining cut placement in beef, as well as other primal processing tasks (e.g. automated deboning, fat trimming etc).

Trials were then focussed on the eye muscle (*longissimus dorsi*), particularly around the grading site used for marbling determination. To do this, the short loin and rib set for given carcase sides were chosen. The carcase side identification numbers were logged and the complete grading data

for these sides were provided. The samples were scanned both with bone-in and then boneless. This data potentially enables:

- Quantifying of grading measures using the CT data and verification against the human grading results.
- Quantifying the effect of beam hardening on data analysis.
- Identifying the effects of different scanning parameters.
- Identifying the effects of different post-processing kernels used to build the CT data.
- Visualising the presentation of the entire length of the *longissimus dorsi* and how composition varies away from the current grading site.

The scans on the bone-in rib set samples demonstrated significantly less beam-hardening effect due to the shorter rib length (see Figure 16).

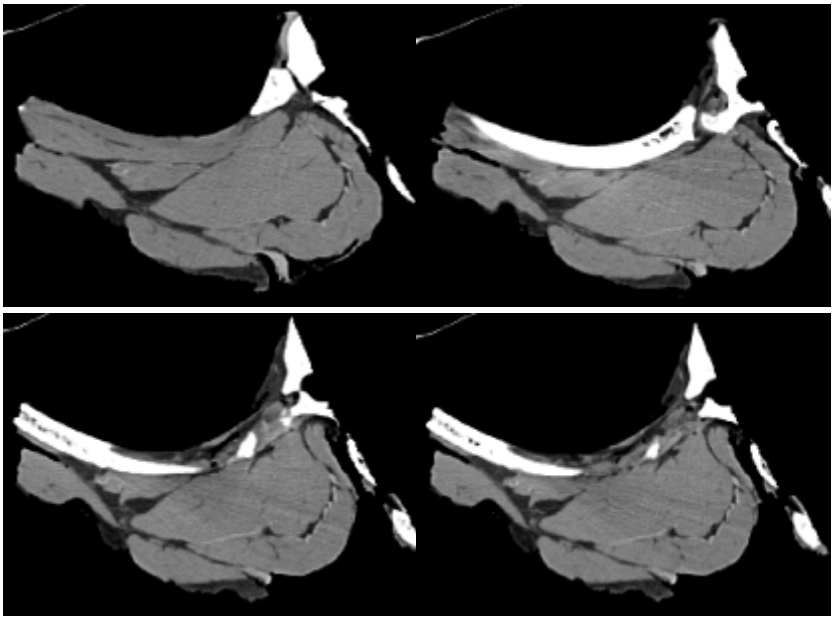

Figure 16 - a number of slices taken from a CT image of a bone-in rib set

A series of scans were taken with the ribs at a 45^{o} angle to the scanning axis to observe how beam hardening presented when the scan direction was out of alignment both with the ribs and with the spine. The beam hardening in this case was reduced further (see Figure 17).

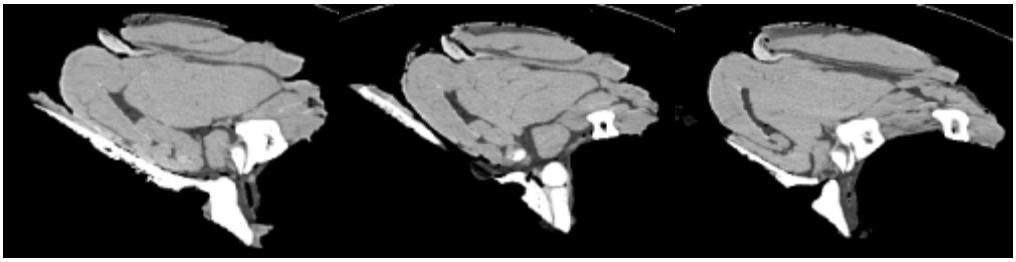

Figure 17 - a number of slices taken from a CT image of a bone-in rib set oriented at 45^{o}. This is the same sample presented in Figure 16.

As aforementioned, each sample was first scanned bone-in before being boned out by a trained boning room operator and scanned again boneless. This procedure will enable the quantification of the effect beam-hardening on actual calculated results.

4.2.3 Intramuscular Fat Analysis

Preliminary work was performed on characterising marbling in beef samples. By performing this high-level analysis, an understanding was developed on how these characteristics are to be explored in the next stage of the project if stakeholders agree that this application warrants further, in-depth investigation.

First, MSA grading cards for marbling were transformed into a numerical model to which the outputs of CT image analysis could be compared. These MSA grading cards come in increments of 100, from 100 through to 1100. When a grader assesses a carcase, the grade assigned is in increments of 10 (from 100 through to 1190). Thus they interpolate the grades between cards for a given carcase. For this stage of the project, the grading cards were analysed in vision processing software, converting each marbling score to a percentage of visible fat coverage. The values between cards were then interpolated linearly (see Figure 18).

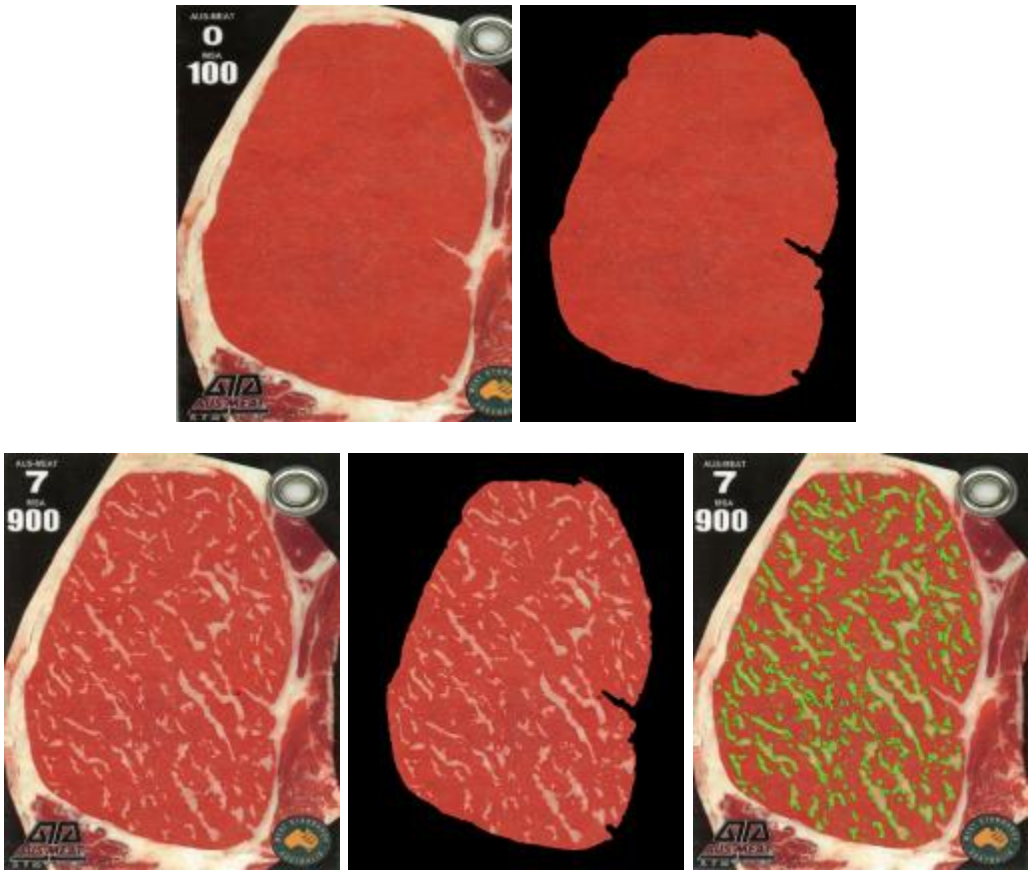

Figure 18 - An example of two MSA grading cards and their masked images which were used for histogram data analysis, extracting the ratio of tissue to fat in the image and providing a percentage total fat in the isolated muscle cross-section. The bottom-right image shows the boundaries for the intramuscular fat specks identified for the MSA 900 card.

The results are shown in Table 1. These values are the inferior limits – a result for a sample would be binned into the next lowest category (e.g. a sample calculated as possessing 11.10% intramuscular fat would be categorised as MSA720).

Table 1 - The table shown below indicates a percentage fat total for each marbling score, as extracted from the MSA Grading Cards. This was a quick calculation and will have some errors introduced, however it does provide some objective figures to a typically subjective grading process.

MSA Grade	Calculated % IMF	Interpolated Values								
		x10	x20	x30	x40	x50	x60	x70	x80	x90
MSA100	0.33%	0.34%	0.35%	0.36%	0.38%	0.39%	0.40%	0.41%	0.42%	0.43%
MSA200	0.44%	0.48%	0.52%	0.56%	0.60%	0.63%	0.67%	0.71%	0.75%	0.79%
MSA300	0.82%	1.01%	1.20%	1.39%	1.58%	1.77%	1.96%	2.15%	2.34%	2.53%
MSA400	2.71%	3.00%	3.29%	3.58%	3.87%	4.16%	4.45%	4.74%	5.03%	5.32%
MSA500	5.61%	5.90%	6.18%	6.47%	6.76%	7.04%	7.33%	7.62%	7.90%	8.19%
MSA600	8.48%	8.67%	8.87%	9.07%	9.27%	9.46%	9.66%	9.86%	10.06%	10.26%
MSA700	10.45%	10.71%	10.97%	11.23%	11.49%	11.75%	12.01%	12.27%	12.53%	12.79%
MSA800	13.05%	13.47%	13.89%	14.32%	14.74%	15.16%	15.58%	16.01%	16.43%	16.85%
MSA900	17.27%	17.51%	17.74%	17.97%	18.21%	18.44%	18.67%	18.90%	19.14%	19.37%
MSA1000	19.60%	19.72%	19.84%	19.95%	20.07%	20.18%	20.30%	20.42%	20.53%	20.65%
MSA1100	20.76%									

Several approaches to the analysis of collected CT data were then explored. There are two critical processes in this analysis; segmentation and histograms.

Segmentation will place boundaries around parts of the image, ensure that the correct part of the product is being measured. Several segmentation software solutions were evaluated which provide a number of tools to facilitate sample segmentation for further analysis.

After an extensive search and trialling, the program selected to be most appropriate for analysing the Beef CT data from Brooklyn and determining the Beef Grade from the imaged 3D data is *Seg3D*. http://www.sci.utah.edu/cibc-software/seg3d.html. Figure 19 shows a typical example for analysing a CT data set.

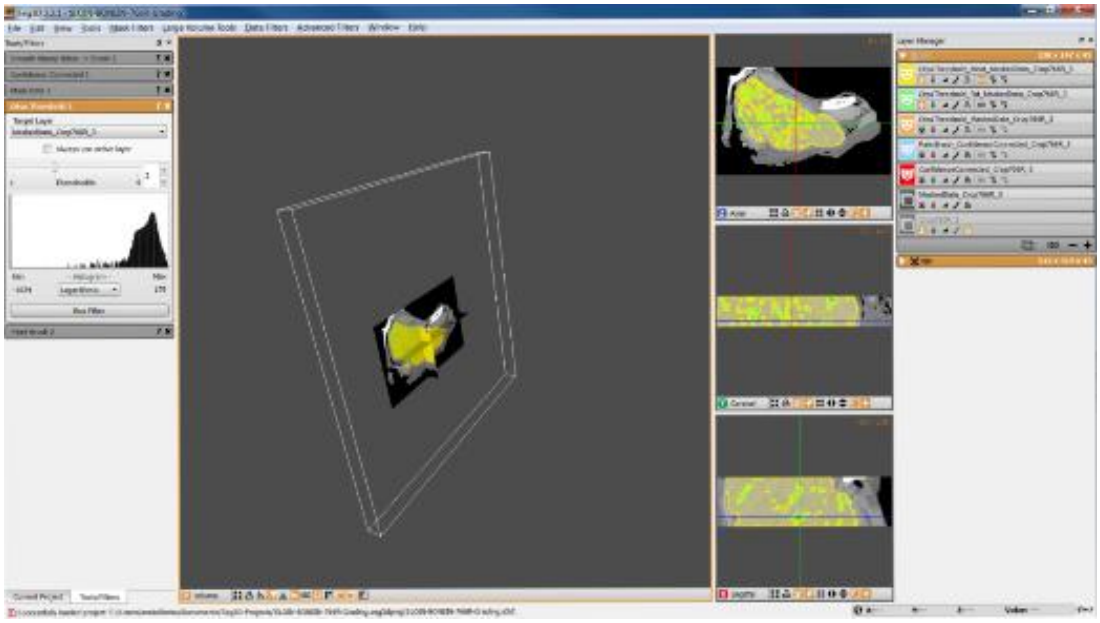

Figure 19 - Example screenshot from Seg3D software during evaluation

Seg3D has many automatic and manual tools for segmenting various regions from the 3D data sets. Following is a description (Table 2) of the methods used to determine the beef grade from two carcases, designated 850R and 766R, which were graded as 380 and 590, respectively, for marbling. The determination is done on 3D images from the short loin of these carcases.

Table 2 - Intramuscular fat content vision processing

850R	766R
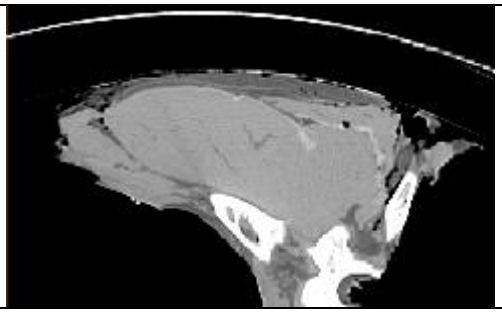	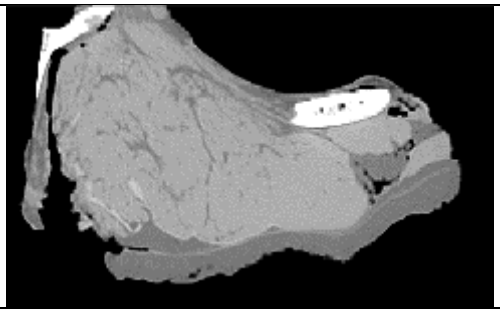
Step 1: Crop the 3D data into a smaller and more manageable 3D volume. In this case, both data sets were cropped to 238 x 147 x 43 voxels.	
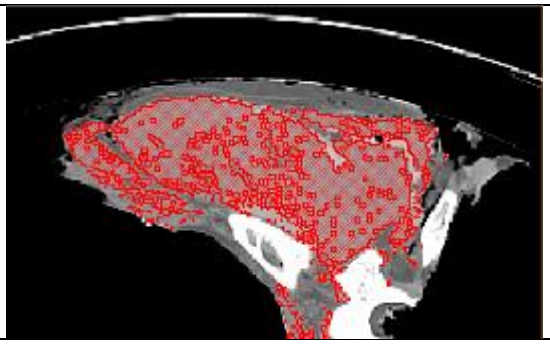	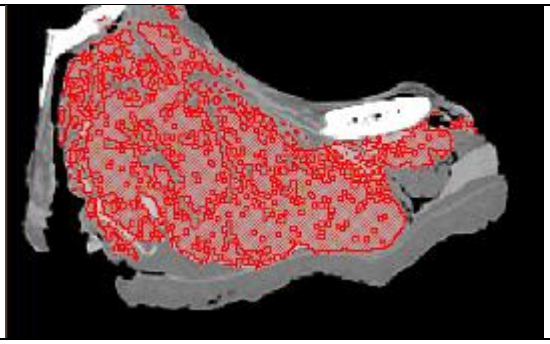

Step 2: Initialise the mask that represents the *longissimus dorsi*. The *Confidence Connected* feature is used to create a mask that at least overlaps the muscle in 3D. As can be seen, the muscle is not completely tagged and that other muscles have also been tagged by the mask.

At this point it must be emphasised that there is the need for a registration approach in which a well-known muscle model is used as a seed for a *Registration* technique to help automate this step and step 3. *Seg3D* does have a feature called *Point Set Registration* that would be worth investigating once a model is made available.

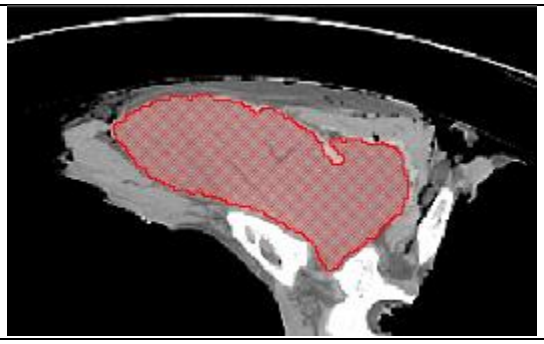

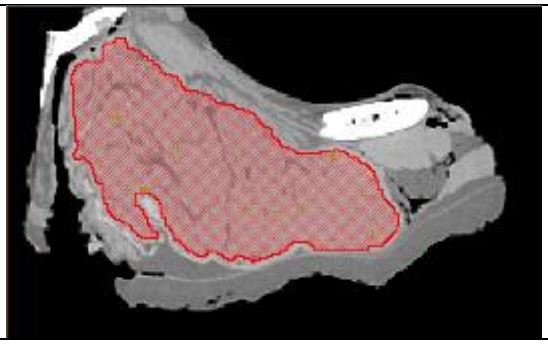

Step 3: Manually perform a sequence of *Painting, Dilation and Erosion* steps until the *longissimus dorsi* is uniquely tagged by the mask. The number and order of steps required is subjective and depends on the operators understanding of cattle anatomy. *Seg3D* efficiently and comfortable facilitates these steps, using the *Paint Brush* and *Smooth Binary Dilate -> Erode* features.

By using the *Mask Data* feature, the *longissimus dorsi* is extracted into its own 3D data set. Note that the mask does not extend to the very edge of the muscle. The main purpose is to minimise any edge effects in the following calculations.

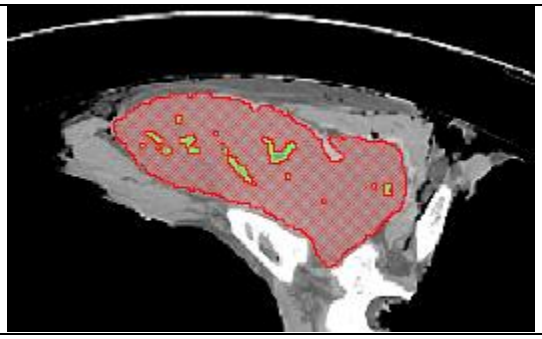

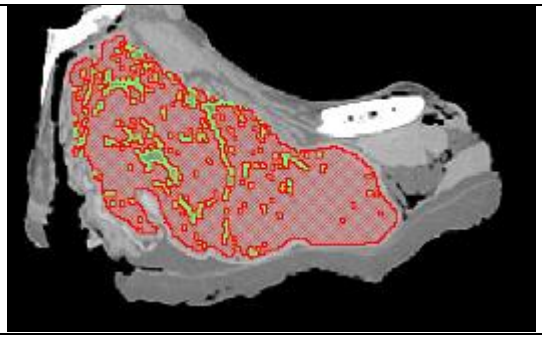

Step 4: If there are no significant artefacts in the images, namely no Beam Hardening, then an automatic process can be used to segment the fat and muscle in the masked regions. The *Otsu Threshold* feature is used, typically with 2 thresholds. In this case three masks are generated but the first one is discarded since it only represents empty space.

In the examples above, only carcase 766R was amenable to this process. The *red* represents meat and the *green* represents fat. The total voxel count for these two 3D regions is 304,117 meat and 42,233 fat voxels. For the representative slice the voxel count is 14,473 meat and 1,840 fat voxels.

To segment carcase 850R, a sequence of manual steps is required. The best approach is to create a mask that tags only the fat voxels. The mask that tags the meat voxels is then created from the difference between the muscle mask and the fat mask. To create the fat mask, the *Neighbourhood Connected*, *Paint Brush* and *Boolean OR* features are used. Once again, the number and order of steps required is subjective and depends on the operators understanding of

how fat networks are distributed through meat.

Again, *red* represents meat and the *green* represents fat. The total voxel count for these two 3D regions is 232,786 meat and 5,362 fat voxels. For the representative slice the voxel count is 10,775 meat and 329 fat voxels.

As above, this is a tedious task to complete manually. An alternative approach using histograms is proposed in Step 5.

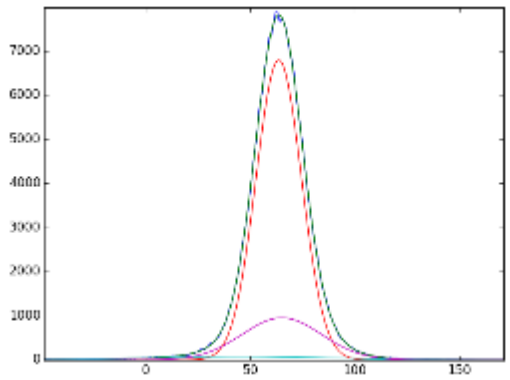

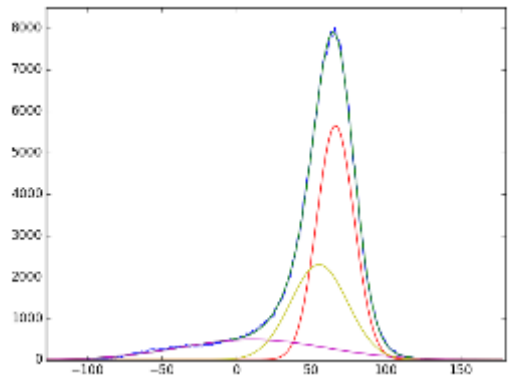

Step 5 (Alternative): *Seg3D* allows data sets to be exported in the *nrrd* format. The masked 3D image data set (end of Step 3) is saved to disk. *Python* is a very flexible programming language and has many packages. By using the *numpy* and *scipy* packages, histograms can be generated from the image data. Gaussian curves are then fitted to the histogram and the area under each curve represents the number of meat and fat voxels. Above are the histogram and the fitted Gaussians for the two carcases.

However, as can be seen from the results, the histogram is not composed of ideal Gaussian curves – a more appropriate curve may be needed, such as a Poisson distribution. Nevertheless, data can be extracted if the correct curves are combined.

For carcase 850R, the *red* and *purple* curves are combined to give 230,096 meat voxels and the *aqua* curve gives 8,118 fat voxels. For carcase 766R, the *red* and *yellow* curves are combined to give 287,311 meat voxels and the *purple* curve gives 59,927 fat voxels.

This approach has the advantage that further segmentation between fat and meat voxels is not required. However, more work is required to more accurately decompose the histogram. If the values are sufficiently accurate to discriminate between the different Beef Grades, then this approach will be faster.

The preliminary results obtained for each of the aforementioned segmentation methods are shown below (Table 3) for two bone-in rib set samples scanned.

Table 3 – Fat-Muscle segmentation results for each of the segmentation methods discussed

Method	850R			766R		
	Muscle (voxel count)	Fat (voxel count)	% Fat	Muscle (voxel count)	Fat (voxel count)	% Fat
3D Segmentation	232,786	5,362	**2.3**	304,117	42,233	**12.2**
Representative 2D	10,775	329	**3.0**	14,473	1,840	**11.3**
Histogram	230,096	8,118	**3.4**	287,311	59,927	**17.3**

Another important consideration is how to segment bone, lean and fat in a given CT image. Each voxel is assigned a value in Hounsfield units (HU). There are currently no agreed upon, definitive thresholds for composition analysis in beef, although current literature suggests a range of approximately -100HU to 0HU for fat, 30HU to 130HU for muscle, 200HU to 800HU for calcification and 700HU to 3000HU for bone. There are a number of factors which make the determination of these thresholds, and thus the calculation of composition, non-trivial. This is to be investigated further in the next milestone of the project.

Figure 20 shows a histogram of HU values versus ln(Frequency) for the *logissimus dorsi* muscle in three different samples for a single CT slice. It can be seen that in one sample there are three distinct peaks corresponding to fat, muscle and bone. The other samples aren't as clear but suggest similar HU thresholds. This is promising as it suggests hard, universal thresholds may be applicable but further analysis would be required to ascertain this.

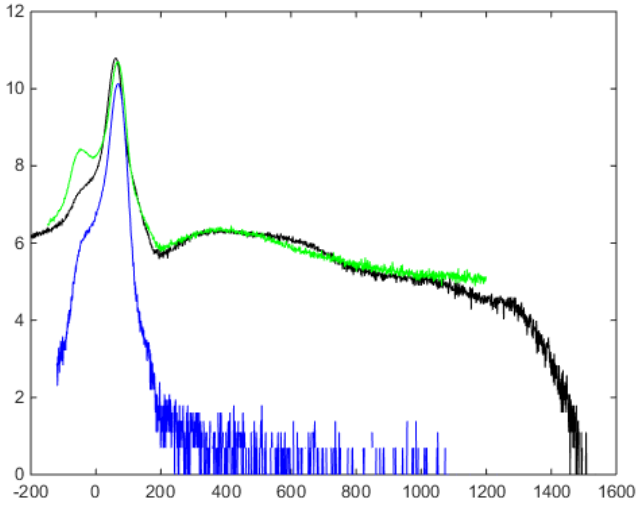

Figure 20 - HU values for three different samples, single CT slice across the *longissimus dorsi*

The calculated fat percentage results for the three segmentation methods (see Table 3) were then assigned an MSA grade using the transformed MSA grading scale (see Table 1). The results of this are shown below in Table 4, along with the grade originally assigned to the sample by a grader. The results obtained suggest viability in investigating this with more detail in the next milestone of the project.

Table 4 - the comparison between the Host Site grading score, and the calculated grading score from three approaches of analysis taken with the Helical CT scan data.

	850R		**766R**	
	% Fat Total	Analysis	% Fat Total	Analysis
3D Segmentation	*2.3*	**370**	*12.2*	**760**
Representative 2D	*3.0*	**410**	*11.3*	**730**
Histogram	*3.4*	**420**	*17.3*	**900**
MSA Marbling Score assigned to sample		**380**		**590**

A number of opportunity areas were recognised for moving forward in this area:

- Higher accuracy mapping of MSA grading cards into numerical thresholds and investigating structure characterisation
- A focus first on ideal segmentation to characterise the effect of different factors including:
    - HU threshold values for lean vs fat;
    - compensation for partial volume effects (a phenomenon which occurs when voxels correspond to material in the sample which isn't purely fat, lean or bone but a combination);
    - intramuscular fat structure characterisation
    - variation of marbling throughout the *longissimus dorsi* muscle
- Numerically determining the effect of beam-hardening in samples
- Comparing results obtained for different scanning parameters
- Obtaining datasets for more samples, along with their grading data
- Investigating requirements for fully automated segmentation and registration

Keeping these considerations in mind, the preliminary results look promising. Further analysis on captured data will allow further insight into the current discrepancy and provide direction for further data acquisition.

4.3 Viscera Study

In order to fully explore the capabilities of the Helical CT system, scanning of beef viscera was explored. The exercise is primarily interested in the detection of contaminants, infection or disease which would lead to the viscera being condemned and therefore not adding value to the cattle beast as a whole.

Availability of a range of condemned product was limited due to the stock processed the day before (grass-fed cattle have different susceptibilities to certain infections and parasites than grain-fed cattle). The viscera are also highly perishable and should be scanned as freshly as possible, which also increases the likelihood of seeing disease and parasites active in the fresh tissue.

For the preliminary study, scanning was undertaken on hearts, livers and kidneys. These were identified by the host site as the most common organs condemned. The supplied product consisted of:

- 'Clean' set of viscera from 2 animals; heart, kidneys, livers
- 'Condemned' viscera; 1 x heart, 2 x kidneys, 2 x livers

4.3.1 Liver

Upon initial analysis, the scans of livers infested with liver fluke (Figure 21) did not clearly show the parasites on visual inspection of the CT images (Figure 22Figure 25). It is believed this is due to the liver fluke being of a very similar structure to the liver tissue thus there is not adequate contrast to clearly identify them directly. However, they may be able to be detected when augmented with another technology (e.g. MRI, ultrasound). It may also be possible to identify indirectly by looking for abnormalities (e.g. in bile duct structure).

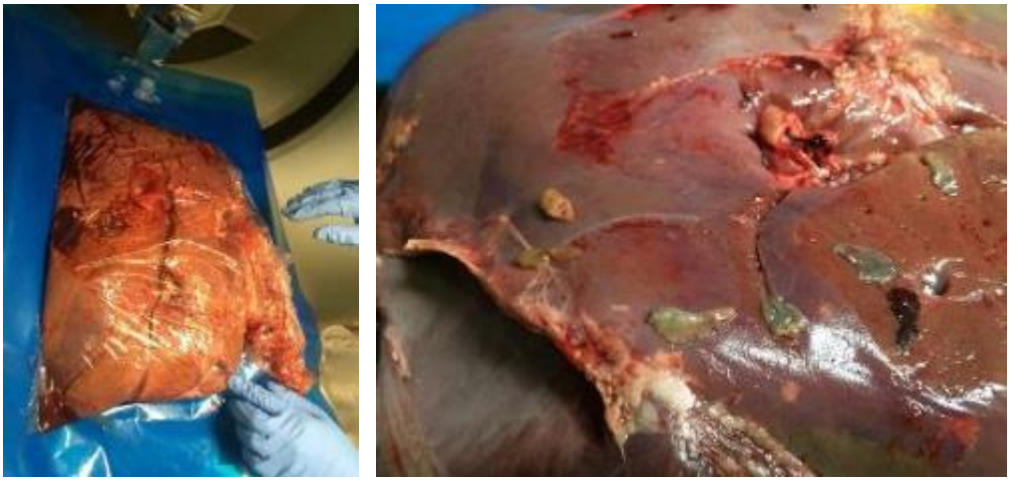

Figure 21 - Clean' sample prepared for scanning (left), 'Condemned' sample (right) showing liver flukes removed from the bile duct area.

Other contaminants to be investigated in the future include abscesses and cysts, which are both likely to be readily detected by x-rays due to their different density compared to surrounding tissue.

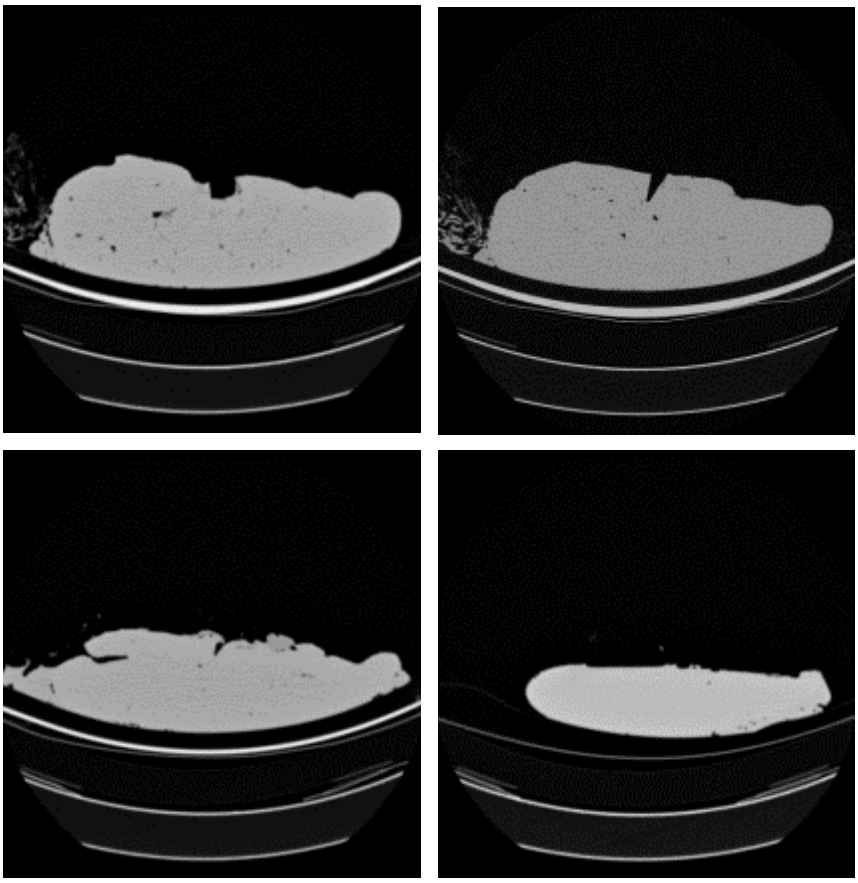

Figure 22 - Helical CT slice images of Bovine Liver. Note presence of bile ducts, and gall bladder on left of image (top left, bottom left), and inspection cuts from AQIS inspector as well as the gall bladder being visible also (top right).

4.3.2 Kidneys

The white spots visible on the kidneys, indicative of subacute interstitial nephritis (Figure 23), do not represent a significant change in density and therefore contrast (Figure 24). Again though, it may be possible to detect this condition indirectly by identifying abnormalities in the kidney tissue. Augmenting the CT technology with another (e.g. MRI, colour camera, ultrasound) may enable robust detection of such defects.

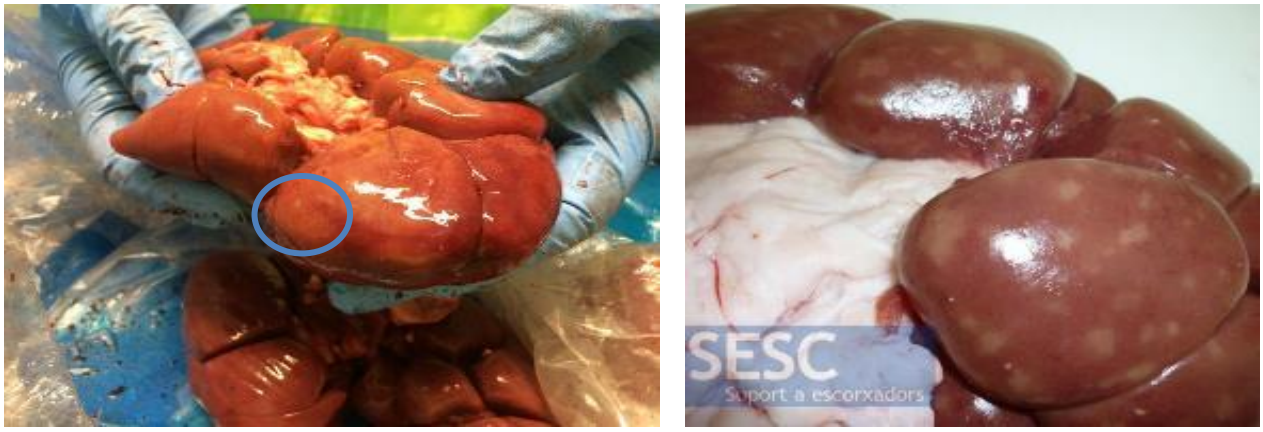

Figure 23 - 'Condemned' kidney sample (left) with white spot highlighted. In this sample the spots were very small; a more severe example is shown (right), image source: (http://www.cresa.cat/blogs/sesc/ronyo-de-taques-blanques-en-un-bovi/?lang=en).

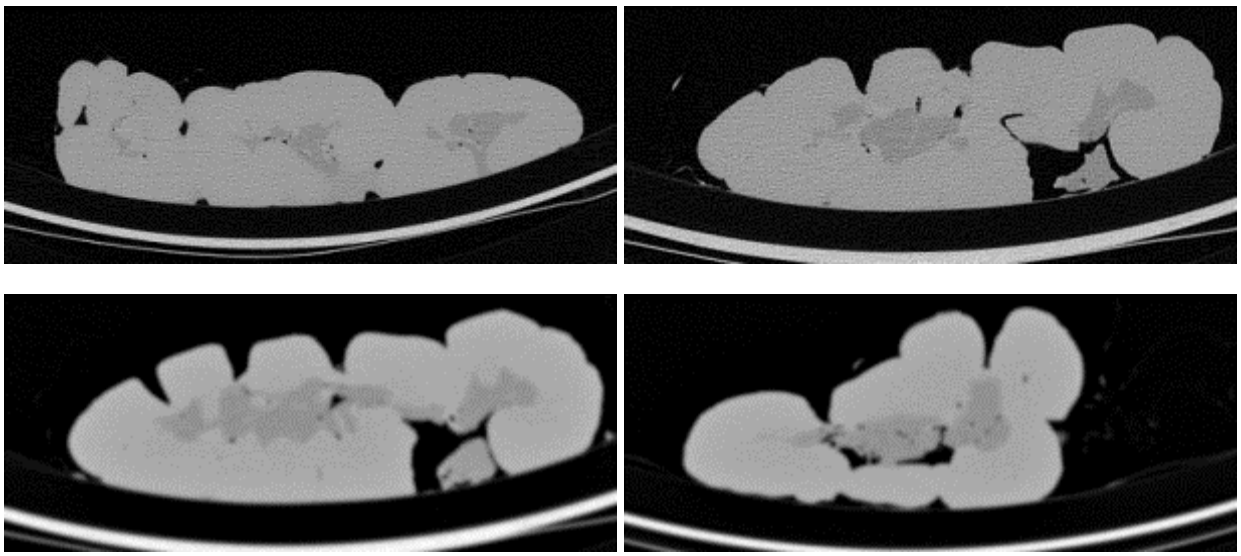

Figure 24 - Helical CT slice images of Bovine Kidney. Note differing image sharpness between top two slices, and bottom two slices. The blurred lower two images show the visual side effect of increasing scan time.

4.3.3 Heart

The heart showed no obvious signs of disease or parasite, even to the host site staff member assisting in the assessment (Figure 25). This further illustrates the need for objective grading of offal contamination within industry. A common cause for condemnation of hearts is presence of tapeworm (*Taenia saginata)* eggs both on the surface of the muscle and within the structure (Figure 26). This was not the case in the sample provided, but this occurrence will be investigated under future studies.

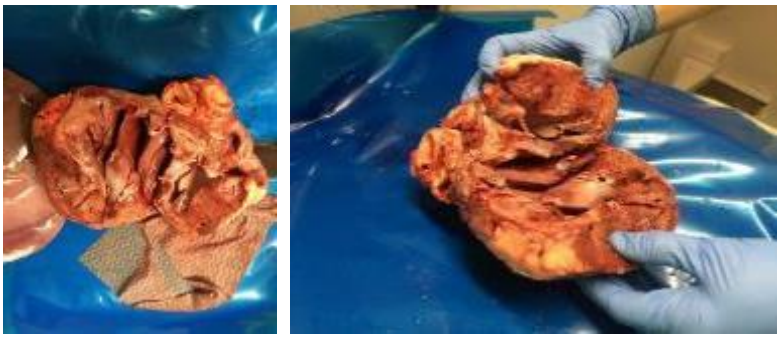

Figure 25 - Condemned' heart sample (top), with knife cuts shown for inspection of the organ; no obvious evidence of contamination or disease in this sample.

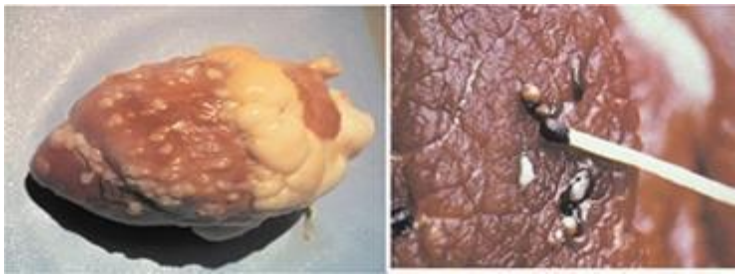

Figure 26 - Image above shows an example of a tapeworm infested heart, with egg sacs shown populating the organ surface and within the muscle, image source: (http://www.afrivip.org/sites/default/files/Helminths-ruminants/musculature.html).

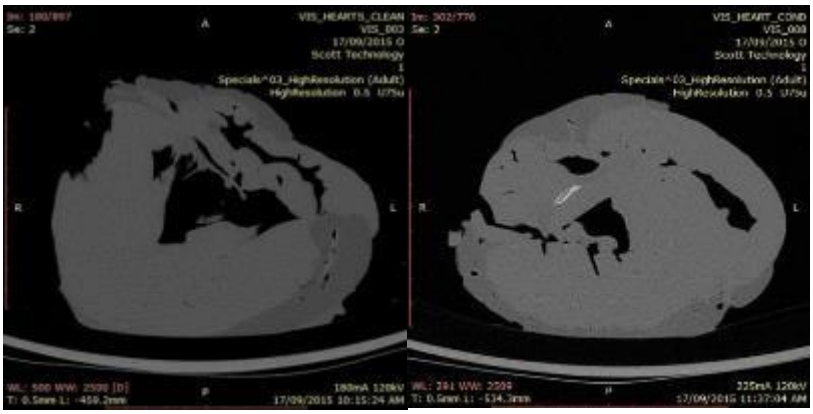

Figure 27 - Helical CT slice image of Bovine Heart. Note cartilage piece in white at centre (bottom image), and also note additional cavities and openings from knife inspection by AQIS agent as shown in photos on previous page.

While the provided sample set was quite limited, the scans taken do indicate what is observable in x-ray images, which does provide a likelihood of detecting some further contaminants.

Table 5 contains a list of likely contaminants to be found in beef viscera. Some of these are based on minor textural and colour changes in the organs, and it has been established from preliminary scans that these changes may not detectable with x-ray technology alone. In these cases, augmenting the CT scan with another sensing technology (e.g. MRI, ultrasound, colour imaging) would be beneficial in attempting to isolate such forms of contamination.

Items such as cysts (especially those displaying some level of calcification), abscesses and parasite eggs typically have a higher water or fibre content than surrounding tissue and it is expected that these would be detectable.

Table 5 - Summary of investigation of viscera features and contaminants. Red = No, Orange = Maybe, Green = Yes.

Contaminant	CT Scan Completed	Likelihood of Detection	Further Testing Required	Likelihood of Detection (MRI)
Cysts				
Onchocerca				
Abscess				
Tape Worm (Taenia Saginata)				
Liver Cirrhosis				
Liver Carotenosis				
Liver Flukes (Distoma)				
Liver Melanoma				
Liver Sawdust (Nutritional Hepatic Necrosis)				
Liver Telangiectasia				
Kidney Subacute Interstitial Nephritis				
Kidney Petechiae				
Specified Risk Materials (SRMs)				
Parasites (cysticerosis, Sarcocystosis)				
Lymph Nodes				
TVC, E.Coli				

5 Composition Analysis and Muscle Segmentation – Initial Analysis

Upon completion of the initial trials, an internal review was conducted within Scott, discussing the high-level results and observations encountered. It was decided that two attributes in particular should be examined with greater detail: calculation of composition and isolation of muscles.

These attributes were chosen due to their potential relevance to a fairly broad range of applications (e.g. cut placement, saleable yield calculation, grading etc). They were thought to have particular opportunity in the area of grading, especially given the MSA's framework of grading based on cuts. As a result, it was decided these applications would be investigated in the context of grading. Detailed analysis would be done on the opportunities and challenges with respect to isolating the *longissimus dorsi* muscle and characterising the composition of intramuscular fat within it.

5.1 Composition Analysis

5.1.1 Overview

- *A number of practical considerations mean that simply calculating composition based on constant HU ranges may not be accurate enough for a commercial application. This includes the partial volume effect; reference HU ranges for fat, lean and bone; and CT scanning configurations.*

- *Histogram data of the striploin and ribset scans show variation in fat peaks presentation while the lean muscle peaks are fairly consistent both between scans and within scans (from slice to slice) although this variation might not have a practical effect.*

- *There was little difference between moderate speed/power and low speed/high power scans. There was a significant difference with the line-speed scans although the trend of the data was similar.*

- *Reconstruction kernel used affected absolute results but showed little relative difference.*

- *Intramuscular fat looks to vary along the longissimus dorsi.*

- *Based on these, the following considerations should be factored into further trialling and analysis:*
    - *scans of just the longissimus dorsi along with chemical lean calculation as an objective comparison point*
    - *scans performed with 0.6mm slice widths*
    - *samples spanning entire range of marbling scores and of different breeds, genders etc should be obtained*
    - *scan with line-speed and moderate speed parameters only*
    - *obtain data for varying levels of intramuscular fat with chemical lean obtained as an objective comparison point*
    - *obtain scans of segments of the longissimus dorsi for each sample and obtain chemical lean as an objective comparison point*

5.1.2 Introduction

A CT scan produces of a collection of 2D 'slice' images along the length of the sample. These slice images consist of an array of voxels (the equivalent of a pixel in a traditional image), each of which is assigned an intensity value in 'Hounsfield Units' (HUs). Different materials tend to be associated with certain ranges of HU values which means, theoretically, the composition of a scan for a certain material can be identified by identifying the proportion of voxels in its associated HU range. For example, if fat is believed to be represented uniquely by HU values greater than -100 and less than 0, then the number of voxels within this range divided by the total number of voxels in the entire sample's CT image will give the proportion of fat in the sample (by volume).

In practical applications however there are a number of reasons why the aforementioned process doesn't reliably hold; the key factors being:

- the partial volume effect;
- variability of reference HU ranges (both inter- and intra-species); and
- variability between CT scanner hardware, scanning parameters and scanning protocols. (Bardera, Boada, Font-i-Furnols, & Gispert, 2014)

The work in this milestone thus sought to provide more definition in these areas to identify the key areas that further trialling should address in developing algorithms for automated composition analysis of a given sample.

5.1.3 Partial volume effect

The partial volume effect is observed when a given voxel does not represent a volume of a 'pure' tissue, but rather a mix. Consider the example shown in Figure 28.

- In each of the panels (A, B and C), the outer square represents the field of view for the image and each square on the grid represents a 'voxel'.
- Panel A shows the physical setup of the example. The field of view of the image contains two substances: a circular area of substance I which has a HU value of 10, and the remaining area of substance II which has a HU value of 0.
- When an image is captured, the image is discretised into an array of square voxels based on the resolution of the system. Each voxel is shown as a square on the overlayed grid. It can be seen that the voxels at the centre of substance I appear as 10HU as expected. However, the voxels at the edges have a mixed proportion of substance I and substance II, which result in voxels of intensity 3HU and 8HU.
- Panel C shows the CT image of the field of view. Rather than containing only voxels of 10HU (substance I) and 0HU (substance II), there are also voxels of 3HU and 8HU. There is also no clear boundary between the two substances.

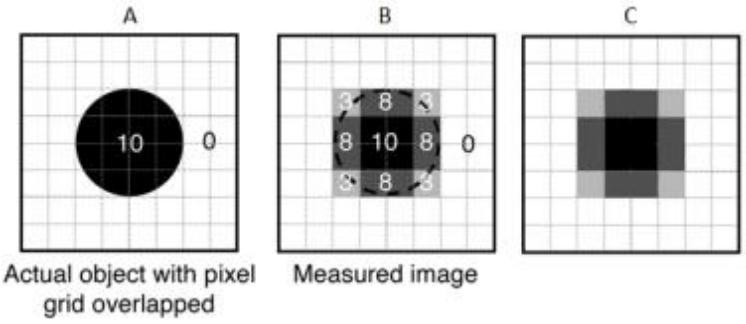

Figure 28 - Partial volume effect

For the purposes of composition analysis, this effect has two main interactions. Firstly, at boundaries between tissues, there will be voxels which can't strictly be classed as fat or lean in the same way that, in the example above, the voxels with values of 3HU or 8HU can't strictly be classed as substance I or substance II.

Secondly, a layer of complexity is added when the tissues are characterised by HU ranges rather than exact values. With the example above, consider that a pure sample of substance I, rather than presenting as 10HU presented over the range 8HU-10HU. In this case, should voxels of 8HU be considered as pure substance I or a combination of substances I and II? It is in this way that the partial volume effect can overlap the issue of variability of reference HU ranges for fat, lean muscle and bone.

Considering these points from a practical perspective, this issue only needs to be catered for in an automated algorithm if its effect is significant relative to the application. **Thus, the following considerations should be applied to the next set of trials:**

- **scans need to have corresponding objective data to quantify the effect** (ie chemical lean determination for intramuscular fat composition vs lean muscle in the *longissimus dorsi* muscle)
- **scans should be taken with the smallest slice width possible (0.6mm)** to minimise the effects.

If the effect is shown to be significant, there are a number of methods presented in literature which may potentially be adapted for the specific application.

5.1.4 Reference HU variability

Research suggests that there isn't one set of golden HU ranges for the different tissue types (fat, lean muscle and bone) (Bardera, Boada, Font-i-Furnols, & Gispert, 2014). In the case of bone in particular, there is a large amount of variability due to differences between animals in terms of bone densities (similar to the differences experienced between humans) (Navajas, et al., 2010). There is a possibility for variation between different species, between breeds within the same species, as well as within different animals of the same breeds (Bardera, Boada, Font-i-Furnols, & Gispert, 2014).

In investigating this effect and how significant it may be for the development of automated algorithms, it was decided to first analyse the scans taken of the ribset and short loin primals for four different bodies. It was hypothesised that, by looking at the HU distribution of the samples, there should be clear and consistent peaks to identify the 'pure fat' and 'pure lean' HU values.

Ribset and short loin primals were scanned for four different beef carcases. These primals were scanned bone-in and boneless. Furthermore, one of the samples was scanned at a 45^{o} angle to the scanning axis. Thus, there were 17 scans in total which were analysed, as shown in Table 6.

Table 6 - Scan summary

		Bone-in	BoneLess	MSA Marbling Score
764L	RIBSET			MSA430
	SLOIN			
766R	RIBSET			MSA590
	SLOIN			
849R	RIBSET			MSA240
	SLOIN			
850R	RIBSET			MSA380
	RIBSET 45^{o}	Same sample as 'Ribset' but oriented 45^{o} to the scanning direction	DATA NOT TAKEN	
	SLOIN			

For each of the 17 scans, the HU-value histogram was taken for each slice and cumulatively added to give an overall HU-histogram for the scan. The results for all scans are shown in the histograms in Figure 29 - Figure 32 below. Green lines represent bone-in scans while blue lines represent boneless scans. The x-axis indicates HU-value while the y-axis is the natural log of the frequency.

The observations of note for these histograms are:

- there are distinct peaks for fat (ca. -65HU) and lean (ca. 65HU) but not bone, which presents across the approximate range of >250HU;
- fat and lean peaks seem fairly consistent across all scans;
- the lean peaks however appear much more consistent, sharper and more distinct than the fat peaks

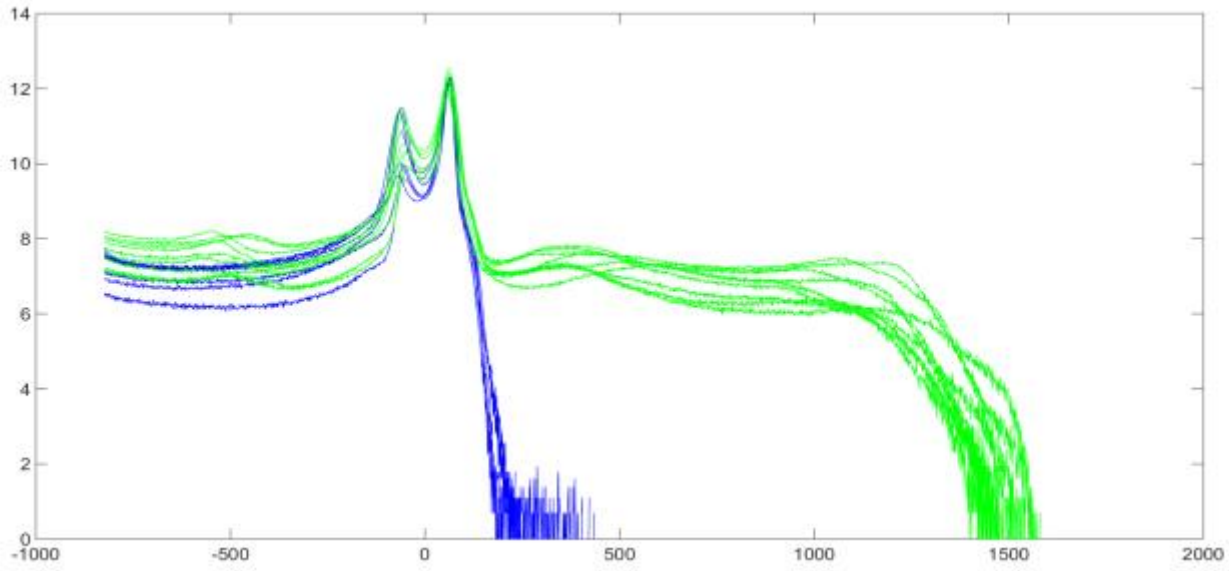

Figure 29 - Cumulative histograms for each scan

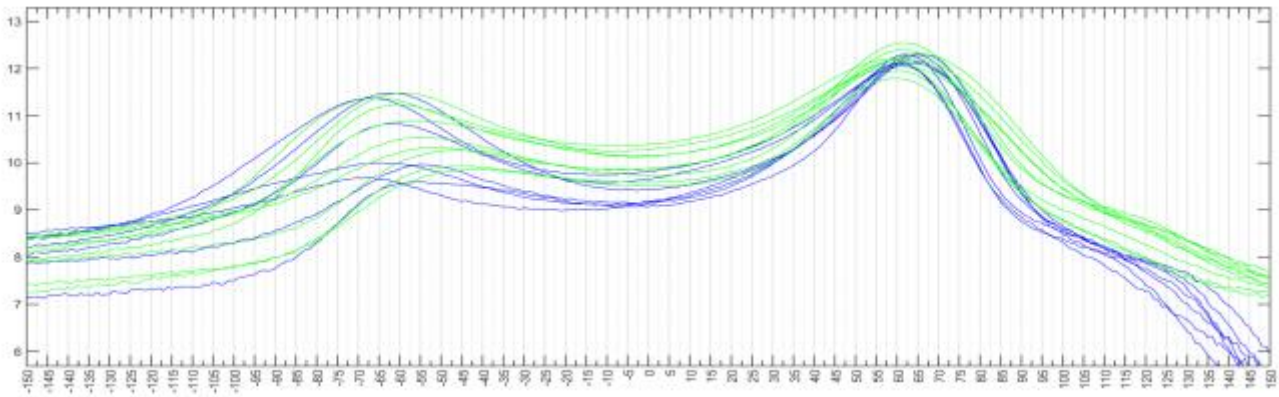

Figure 30 - Cumulative histograms for each scan - zoomed into fat and lean peaks

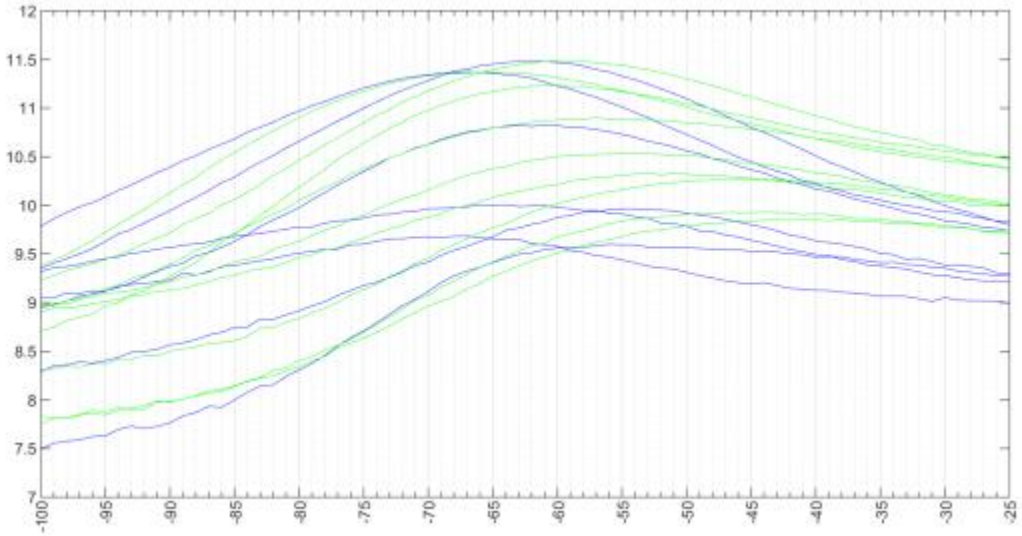

Figure 31 - Cumulative histograms for each scan - zoomed into fat peaks

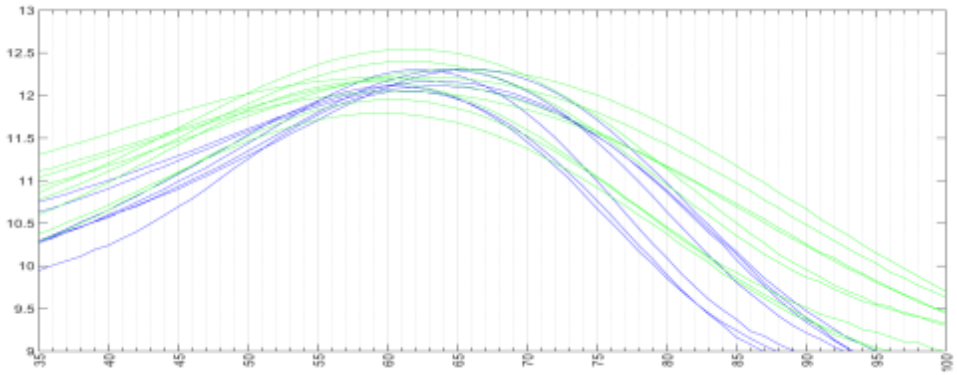

Figure 32 - Cumulative histograms for each scan - zoomed into lean peaks

Figure 33 to Figure 36 below show the histograms for each sample individually. The ribset and short loin scans, boneless and bone-in, are plotted on top of each other for a given sample. The x-axis indicates HU-value while the y-axis is the natural log of the frequency.

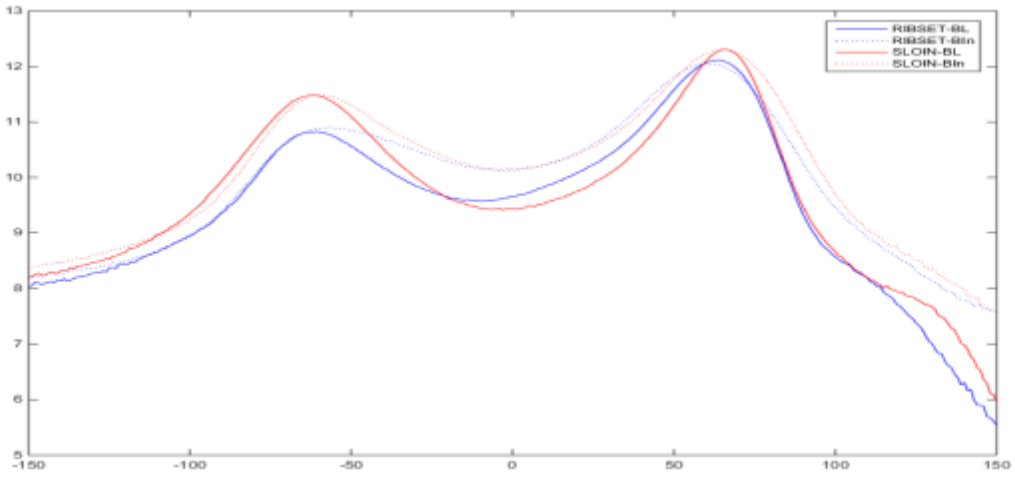

Figure 33 - Cumulative histograms for sample 764

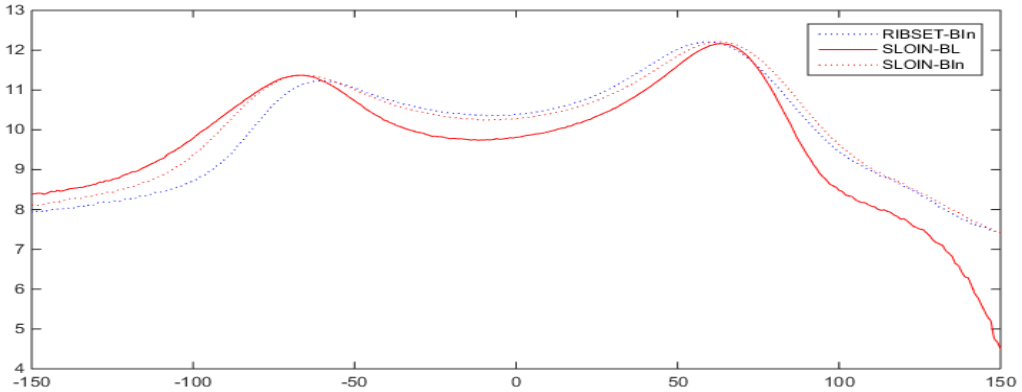

Figure 34 - Cumulative histograms for sample 766

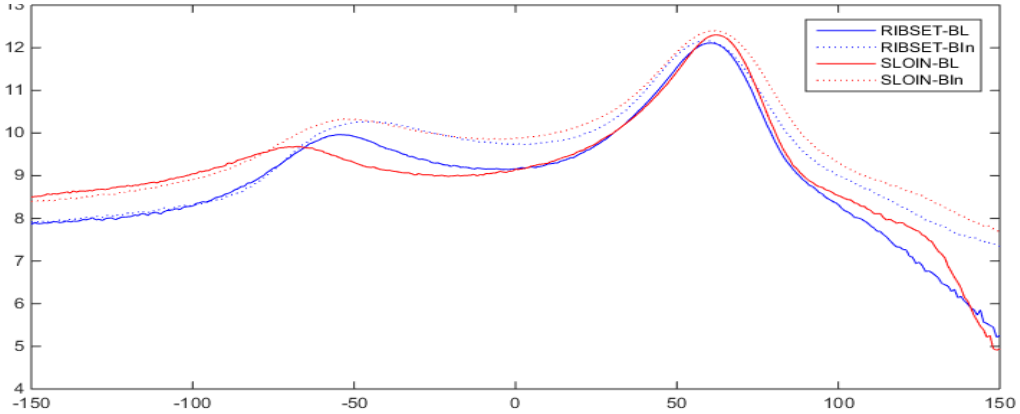

Figure 35 - Cumulative histograms for sample 849

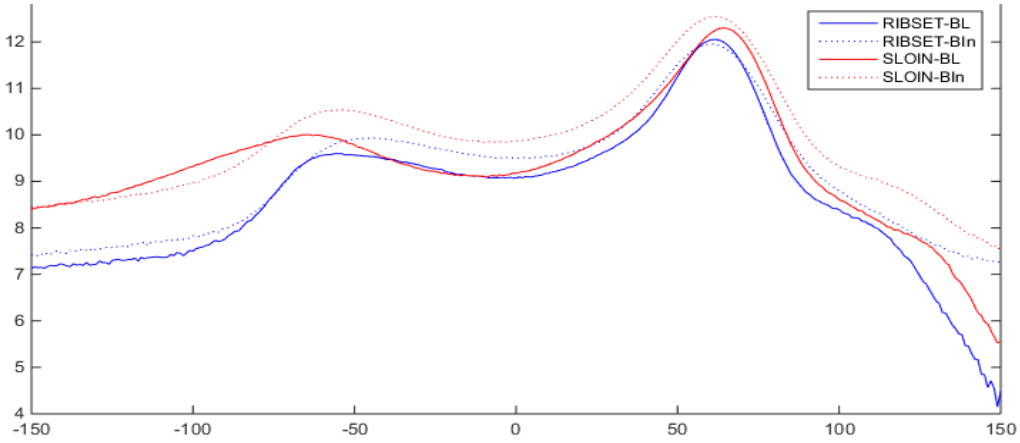

Figure 36 - Cumulative histograms for sample 850

The same observations can be seen although it should also be noted that the fat peaks are particularly shallow for samples 849 and 850. These samples are the lowest marbled, meaning they will also possess less fat in total compared to samples 764 and 766 (Font-i-Furnols, Čandek-Potokar, Maltin, & Prevolnik Povše, 2015).

The peaks for each scan were calculated numerically:

- Fat peak = local maxima over range [-150,0]HU
- Lean peak = local maxima over range [0,150]HU

The results are shown in Table 7. Also added are the MSA marbling score and rib fat measurement taken by the grader for each sample. Observing these results, a number of observations were made. With fat, the peaks aren't as sharp compared to that corresponding to lean muscle. It was expected that the peaks would be consistent across all scans but this wasn't observed. The difference between the bone-in and boneless scans may be attributed to the presence of bone marrow, which has a similar HU range to fat. It's also possible that beam hardening had some effect as well. The difference between the boneless ribset and short loin

primals for samples 849 and 850 may be attributed to these samples having less fat in general. There is also the possibility that pure fat lies over a wider distribution. Intra-species variations may also be having an effect regarding the differences between the samples.

As aforementioned, the lean peaks appeared much sharper and more consistent across all scans. The values for the bone-in scans seem to be slightly lower than their corresponding boneless scans possibly due to the beam-hardening effect.

Table 7 - Fat and Lean Peak Analysis Results

		FAT		LEAN		GRADING DATA	
		Bone-in	BoneLess	Bone-in	BoneLess	MSA Marb	Rib Fat
764L	RIBSET	-57	-61	59	64	430	11
	SLOIN	-58	-61	65	66		
766R	RIBSET	-60	-65	59	61	590	6
	SLOIN	-66	-67	62	64		
849R	RIBSET	-44	-55	58	60	240	7
	SLOIN	-53	-67	61	62		
850R	RIBSET	-44	-56	60	62	380	7
	RIBSET 45°	-41		59			
	SLOIN	-54	-64	62	64		

For each scan, the individual slices were then analysed and the fat and lean peaks identified. Figure 37 - Figure 40 below show the variation for the fat peaks. The horizontal axis is the slice number and the vertical axis is the fat peak calculated for that slice Table 8 summarises the statistical data calculated.

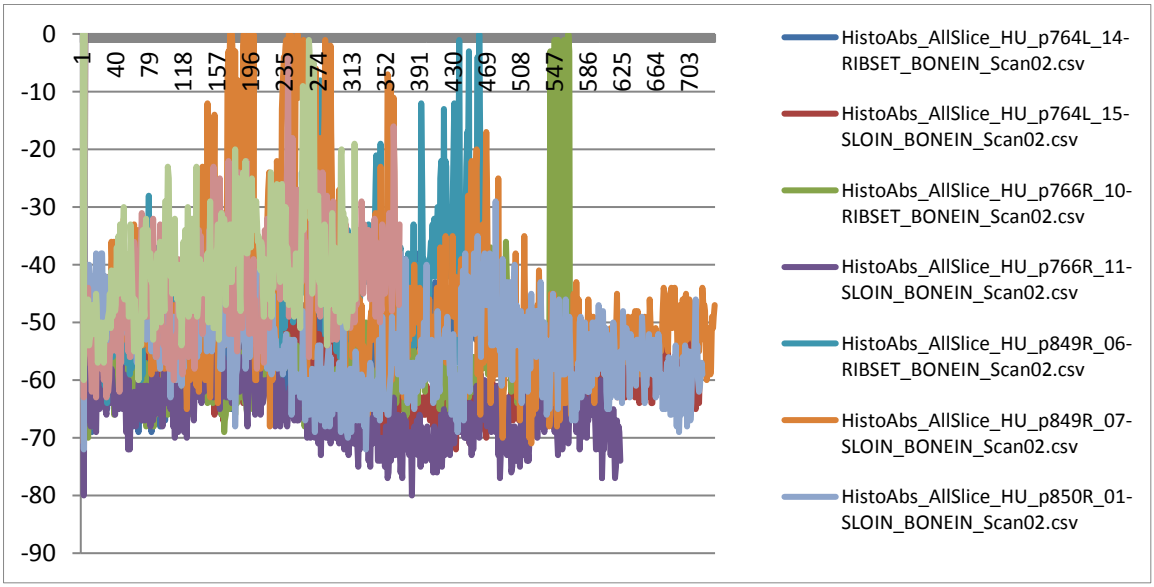

Figure 37 - Fat Peak for each CT slice image - Bone-In Scans

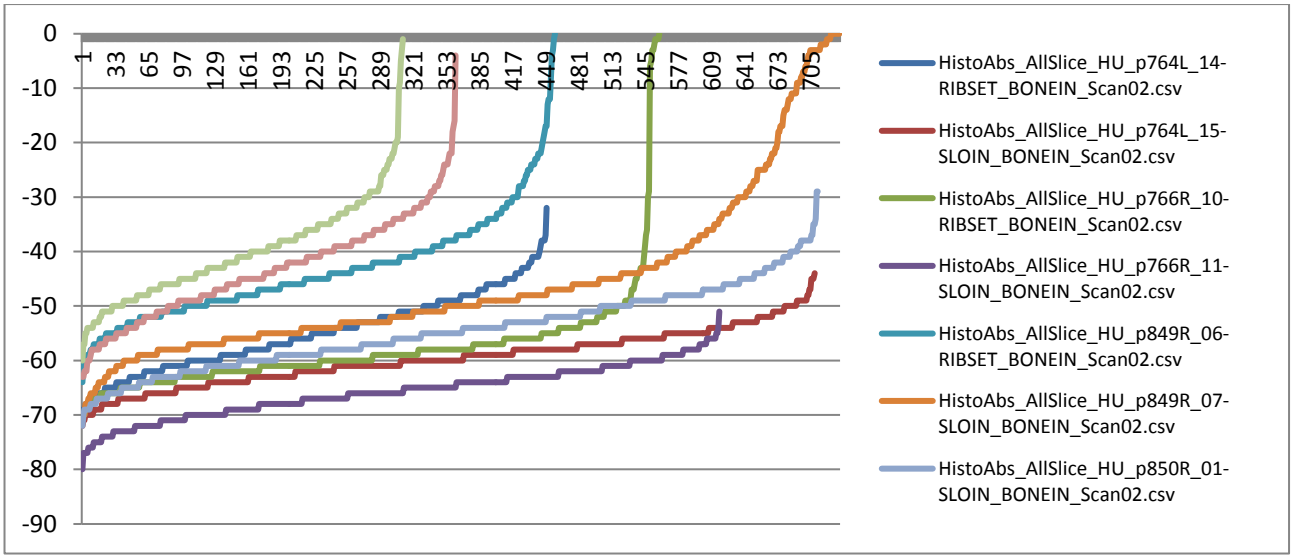

Figure 38 - Fat Peak for each CT slice image - Bone-In Scans (data sorted by increasing fat peak)

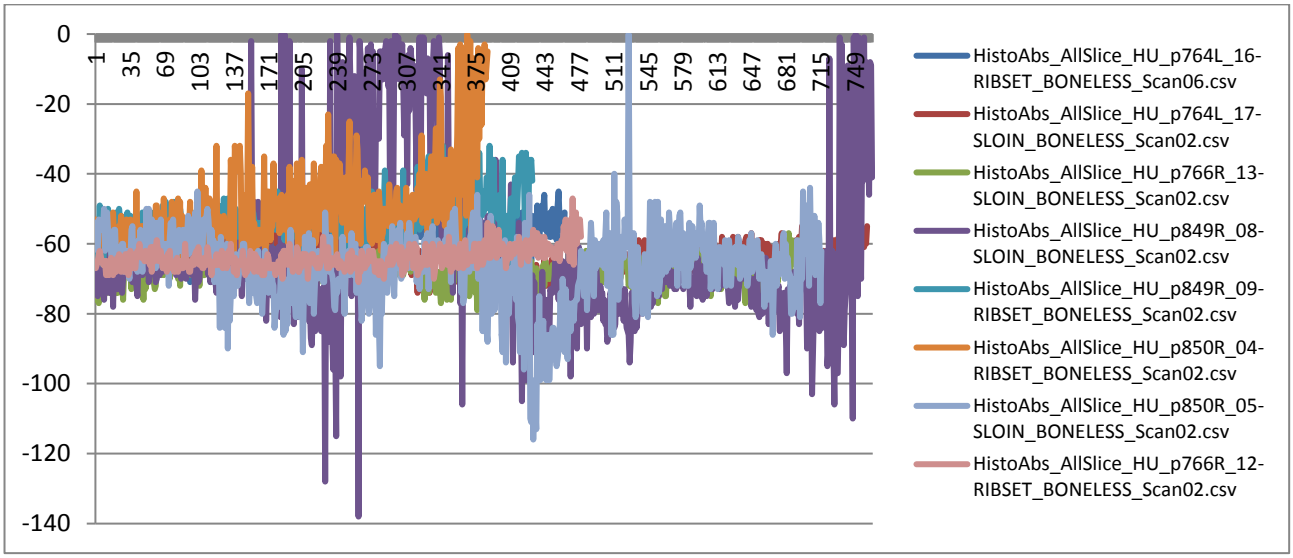

Figure 39 - Fat Peak for each CT slice image - Boneless Scans

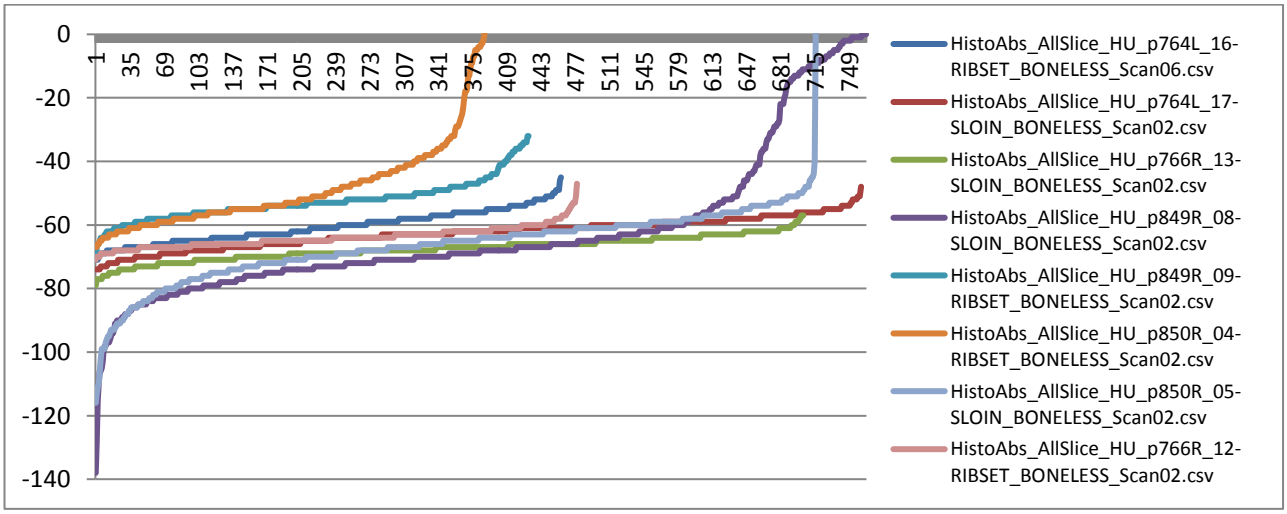

Figure 40 - Fat Peak for each CT slice image - Boneless Scans (data sorted by increasing fat peak)

Table 8 - Summary Statistics of Fat Peak Variation

		BONE-IN					BONELESS				
		Mean	StdDev	Min	Max	Range	Mean	StdDev	Min	Max	Range
764L	RIBSET	**-54.9**	**6.87**	*-69*	*-32*	37	**-60.6**	**4.9**	*-71*	*-45*	26
	SLOIN	**-59.6**	**4.95**	*-72*	*-44*	28	**-62.5**	**4.6**	*-74*	*-48*	26
766R	RIBSET	**-57.9**	**9.16**	*-70*	*0*	70	**-64.0**	**3.1**	*-71*	*-47*	24
	SLOIN	**-65.7**	**4.68**	*-80*	*-51*	29	**-67.4**	**3.7**	*-79*	*-57*	22
849R	RIBSET	**-43.3**	**9.67**	*-64*	*0*	64	**-52.6**	**6.1**	*-70*	*-32*	38
	SLOIN	**-45.9**	**14.81**	*-71*	*0*	71	**-62.4**	**22.8**	*-138*	*0*	138
850R	RIBSET	**-43.4**	**9.20**	*-63*	*-4*	59	**-48.9**	**13.0**	*-67*	*0*	67
	RIBSET 45°	**-40.1**	**9.02**	*-60*	*-1*	59					
	SLOIN	**-54.5**	**7.21**	*-72*	*-29*	43	**-66.7**	**10.8**	*-116*	*0*	116

Figure 41 to Figure 44 below show the variation for the lean peaks. Table 9 summarises the statistical data calculated.

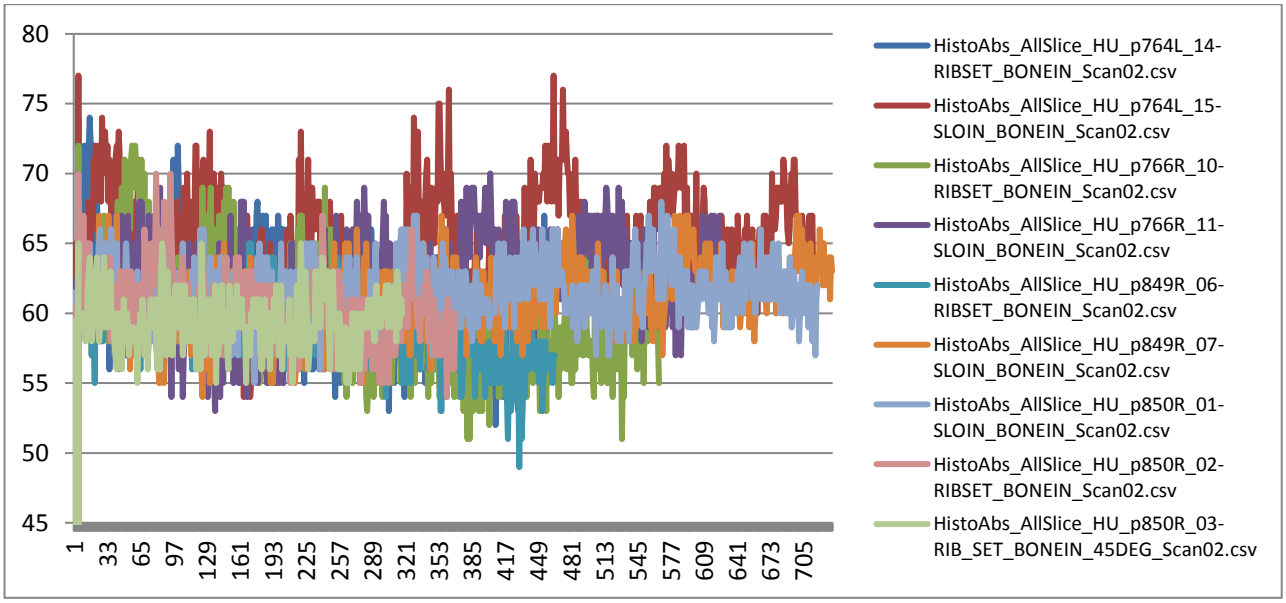

Figure 41 - Lean Peak for each CT slice image - Bone-In Scans

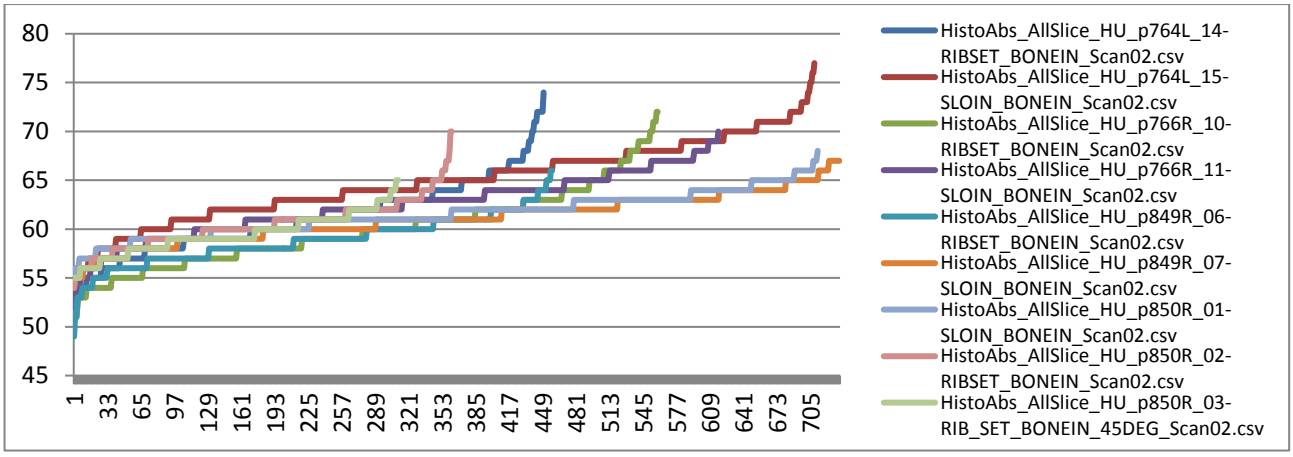

Figure 42 - Lean Peak for each CT slice image - Bone-In Scans (data sorted by increasing lean peak)

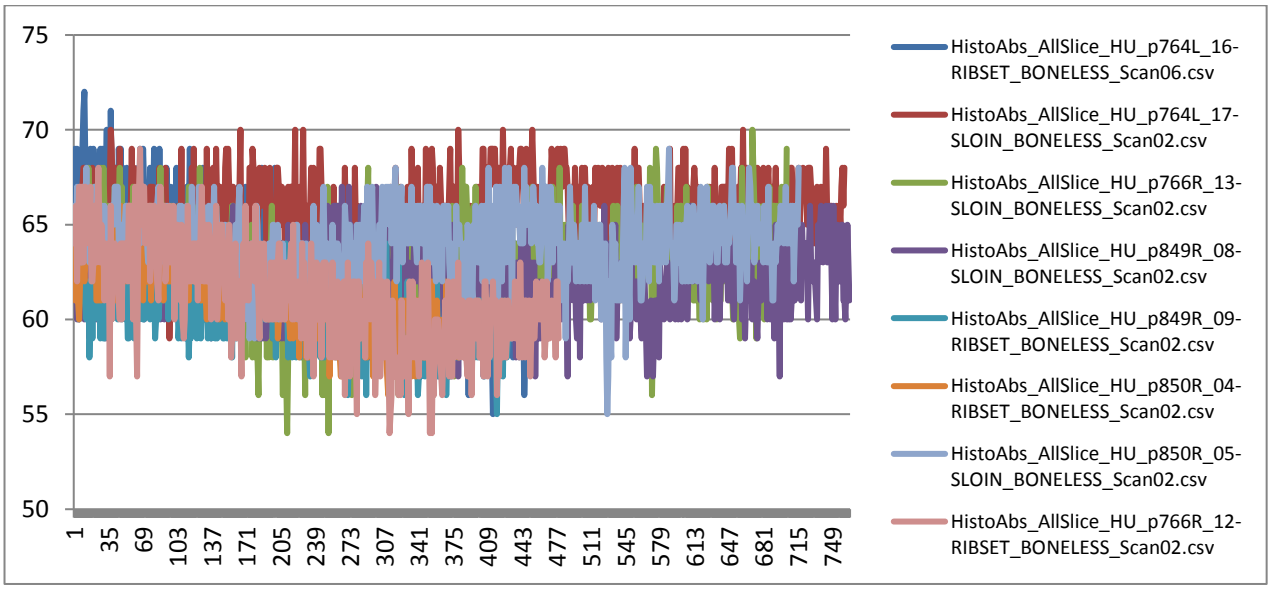

Figure 43 - Lean Peak for each CT slice image - Boneless Scans

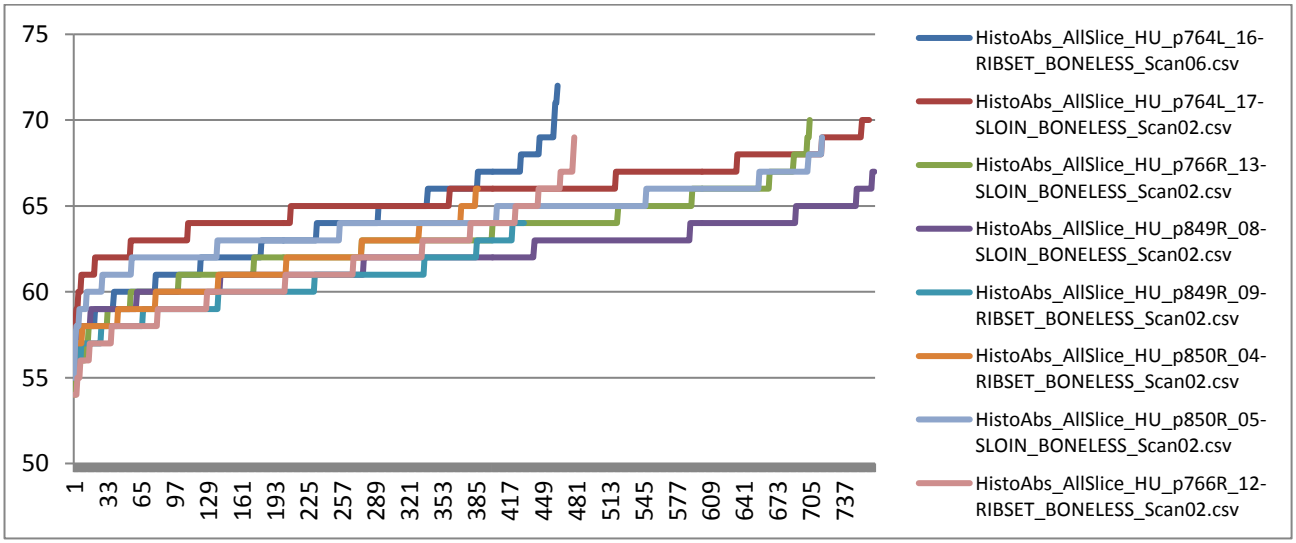

Figure 44 - Lean Peak for each CT slice image - Boneless Scans (data sorted by increasing lean peak)

Table 9 - Summary Statistics of Lean Peak Variation

		BONE-IN					BONELESS				
		Mean	StdDev	Min	Max	Range	Mean	StdDev	Min	Max	Range
764L	RIBSET	**61.1**	**3.74**	*52*	*74*	22	**63.5**	**2.91**	*55*	*72*	17
	SLOIN	**64.9**	**3.91**	*54*	*77*	23	**65.6**	**1.99**	*58*	*70*	12
766R	RIBSET	**59.9**	**3.88**	*51*	*72*	21	**61.2**	**2.71**	*54*	*69*	15
	SLOIN	**62.3**	**3.15**	*53*	*70*	17	**63.0**	**2.44**	*54*	*70*	16
849R	RIBSET	**58.8**	**2.45**	*49*	*66*	17	**60.3**	**1.73**	*55*	*64*	9
	SLOIN	**61.1**	**2.39**	*54*	*67*	13	**62.1**	**1.82**	*57*	*67*	10
850R	RIBSET	**60.4**	**2.39**	*54*	*70*	16	**61.3**	**2.01**	*56*	*66*	10
	RIBSET 45°	**59.5**	**2.02**	*55*	*65*	10					
	SLOIN	**61.5**	**2.15**	*55*	*68*	13	**64.1**	**1.90**	*55*	*69*	14

These findings suggest that the observations made between scans also hold within the same scan. The fat peaks vary significantly more slice-by-slice within the same sample and over a much wider range. The low fat samples also had a higher variation that the high fat samples. One unexpected result is that, for the scans of 850R and the short loin scans of 849R, the variation in fat peak **increased** between the bone-in and boneless samples. The lean peaks on the other hand were much more consistent, slightly more-so in the boneless samples.

Summarising all the findings in this section, the primary questions looking to be answered with respect to the development of automated algorithms are:

- should fat, lean and bone content be quantified using fixed or calculated HU thresholds and what is the practical effect?
- do any other factors have a significant practical effect? For example: partial volume effect, presence of bone, breed etc

5.1.5 CT variations

All trials for this project will be performed with the same unit which is calibrated each morning of trialling. For each scan sample, three different scans were performed:

- moderate speed/power (383mAs, 17.5mm/s);
- high power/very slow speed (1100mAs, 7mm/s); and
- line speed (157mAs, 54mm/s).

These scans were performed one after another without moving the sample in between.

For a particular scan sample (766 boneless ribset), the *longissimus dorsi* region was manually drawn for the first 24 slices for each of the three sets of scan data. The approximate IMF% was then calculated via thresholding. The IMF% calculated for each slice is shown in Figure 45 for the three different scan settings.

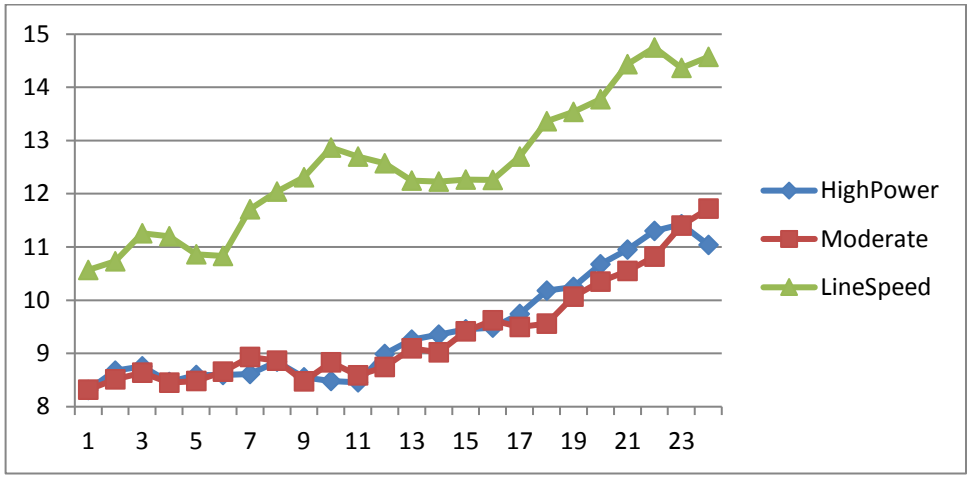

Figure 45 - IMF% for different CT scan settings

It can be seen that the difference between the moderate and high power scans yielded very similar results. The line-speed scans however were significantly different although did yield a similar trend. This suggests that the high power data is likely not required for the next set of trials which is beneficial when considering tube life. If scanning at closer to line-speed, extra data processing steps will need to be performed given the particular application, but the similar trend in data suggests faster scanning may still enable a commercially feasible solution.

It was also found that, when comparing the scans together, there were slight differences in the images suggesting that some movement had occurred. This means any manually drawn regions of interest must be redrawn for each set of scan data which introduces an inconsistency as well as inefficiency. It also suggests there's a possibility that there may have been some movement of the sample during the line-speed scans (although the movement most likely occurred when positioning the bed for a given scan).

Another CT scanning parameter which was investigated was the reconstruction kernel used. Four different kernels were tested: B20f – smooth; B31f – medium smooth +; B45f – medium; B75f – very sharp. The different kernels were compared for the *longissimus dorsi* region for the same sample. It can be seen in Figure 46 that there is a difference in absolute calculated value depending on the kernel used, although the trends are roughly the same. This suggests that, when comparing calculated results to objective results (ie chemical lean), the kernel used may skew the results and this must be considered in analysis. It will also affect the HU values selected for classification.

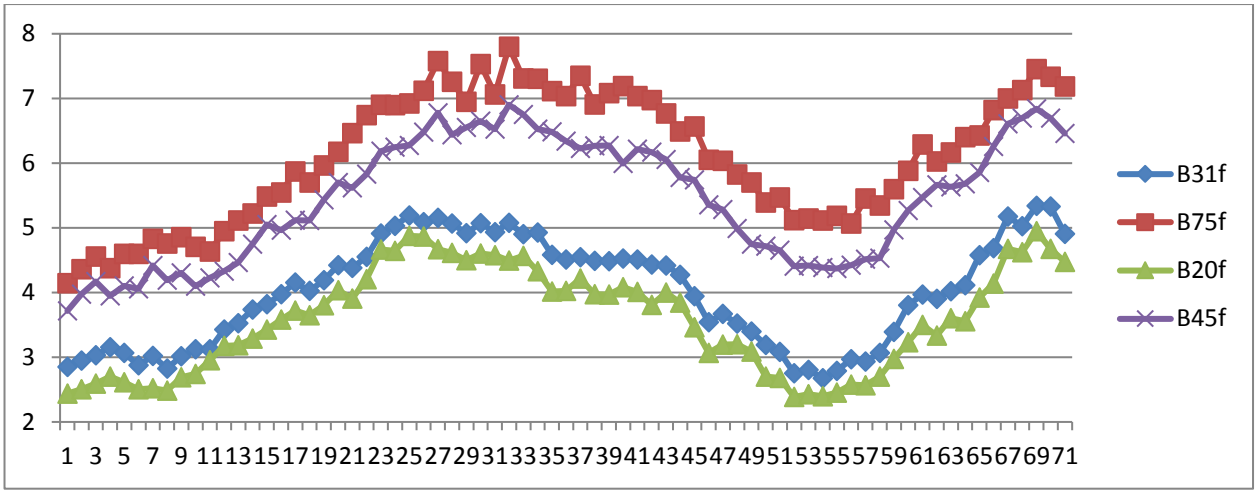

Figure 46 - IMF% for different reconstruction kernels

Summarising all the findings in this section, the primary questions looking to be answered with respect to the development of automated algorithms are:

- what is the fastest we can scan and still obtain results considered accurate enough for commercial feasibility?
- what is the effect of reconstruction kernel used?

Thus the following points should be taken into account for the next set of trials:

- **only scan samples with the line speed and moderate scan parameters**
- **multiple samples containing varying levels of intramuscular fat should be scanned and analysed for chemical lean**

In conjunction with this extra data, additional analysis may need to be performed to characterise the effect of the reconstruction kernel on reference HU determination and composition calculation, especially in terms of linearity.

5.1.6 Intramuscular Fat Variations

While analysing the intramuscular fat throughout the samples, a variation was seen to occur. Figure 47 below demonstrates the calculated intramuscular fat percentage, along with associated MSA marbling grade moving away from the grading site in the ribset and short loin primals.

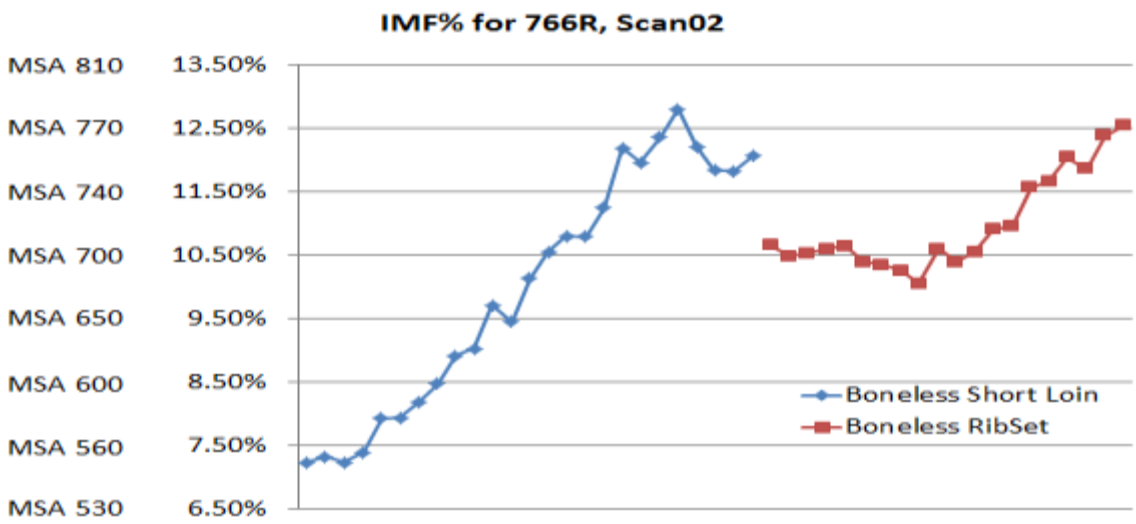

Figure 47 - Variation of Intramuscular Fat either side of grading site

Thus the following points should be taken into account for the next set of trials:

- **objective measurement (ie chemical lean) of intramuscular fat should be obtained at a number of different positions along the *longissimus dorsi* to verify this trend**
- **points of separation of the *longissimus dorsi* for chemical lean testing should be visible on CT scans to match data**

5.2 Muscle segmentation

5.2.1 Overview

- *A number of third party software solutions were trialled with little success in automatically isolating the longissimus dorsi from adjacent muscles.*

- *Bodies with low levels of fat have low/no intermuscular fat between muscles.*

- *A high-level, custom coded algorithm was able to be developed with promising results for longissimus dorsi isolation. It was coded to two samples – 850-Ribset and 766-Ribset and verified across all boneless scans.*

- *Based on these, the following considerations should be factored into further trialling and analysis:*
    - *samples spanning entire range of marbling scores and of different breeds, genders etc should be obtained*

5.2.2 Introduction

The isolation of soft tissue from bone is a relatively simple task due to the large difference in absorption characteristics. Isolating fat from lean muscle however can be a more difficult task, but pure fat and pure lean muscle still have a fair difference between them. Separating two muscles from each other when there isn't a significant amount of other tissue (e.g. fat or bone) between them is quite challenging.

The ability to isolate muscle groups is a task which potentially bears relevance to a number of applications, including cut placement, primal identification, grading etc. In this section, muscle segmentation was investigated under the application of grading. Thus, the *longissimus dorsi* was targeted to be isolated from the scans.

The goal of this work was to investigate this task at a high level and understand the challenges and opportunities related to the development of automated algorithms for this task. From this, any considerations for the next stage of trialling were to be identified to allow work to enable further development.

Scans were taken on two primals (short loin and ribset) for four bodies, both boneless and bone-in. It was decided that in the high-level investigation for this milestone, work would be focussed on a subset of this data. The bodies chosen were 766 and 850 – the highest and lowest marbled samples, respectively. It was decided to focus efforts on the section of the primals closest to the grading site. As can be seen in Appendix A – Beef Cross Sections, the *longissimus dorsi* is the largest muscle. At the furthest points, the shape of the *longissimus dorsi* changes (especially with the short loin) and it becomes smaller and more crowded with other muscles). For these initial investigations, the ribset primal was focussed upon, up to about 150mm from the grading site.

Figure 48 and Figure 49 below show these primals under the bone-in and boneless conditions. It can be seen that the presence of bone did not have much of an effect in terms of maintaining separation of the different muscles.

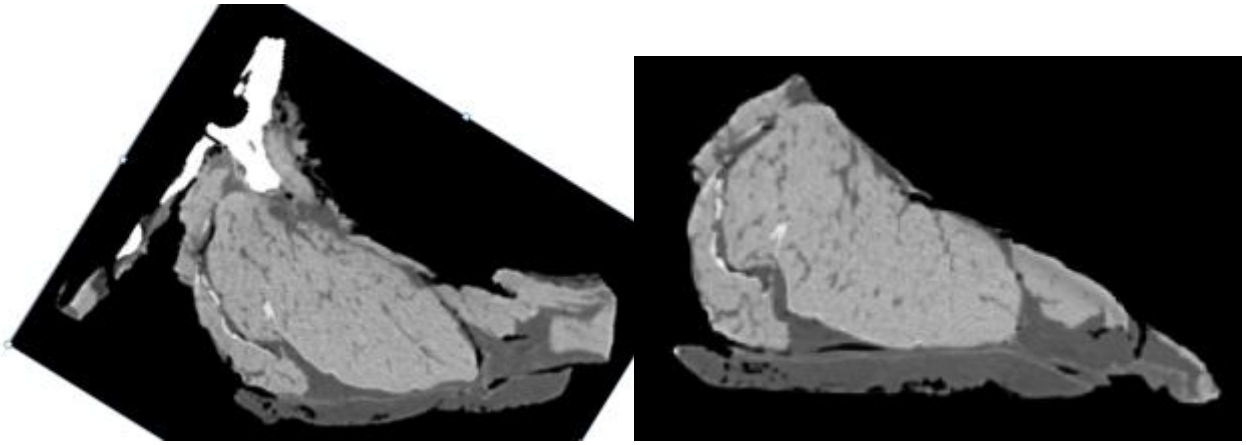

Figure 48 - Ribset primal for 766: bone-in vs boneless

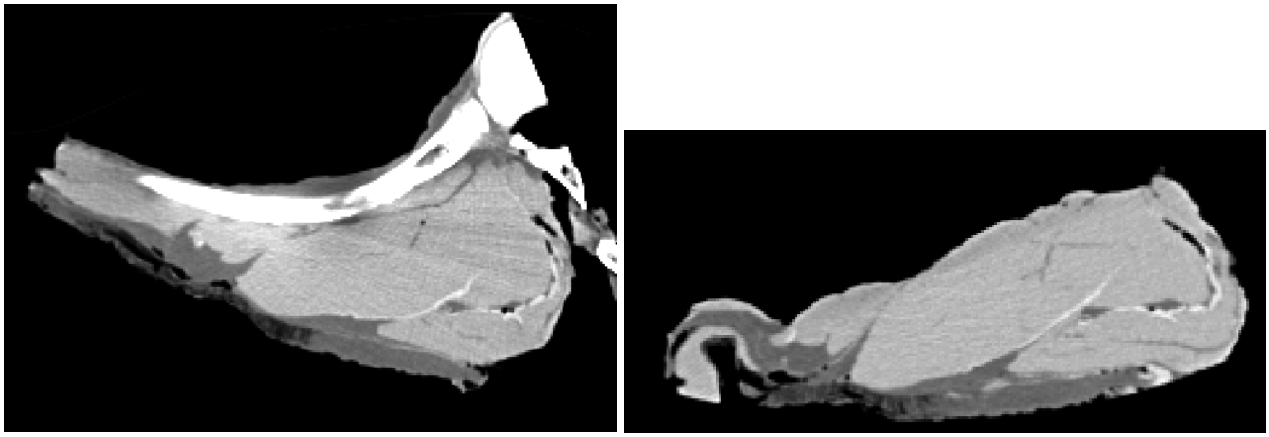

Figure 49 - Ribset primal for 850: bone-in vs boneless

5.2.3 Third party software

A number of third party software packages were first evaluated for this application. These included software packages which feature amongst the literature:

- Seg3D
- Slicer
- TurtleSeg
- ITK-SNAP
- Microview

All of these software options struggled with isolating the *longissimus dorsi* automatically from adjacent muscle groups during initial evaluation. It was then decided to focus some efforts on coding our own segmentation algorithms.

5.2.4 Custom developed algorithms

A number of approaches were trialled in attempting to isolate the *longissimus dorsi* from the adjacent muscles. Initially we had little success, as eventually the isolation would completely degrade, either filtering out most of the *longissimus dorsi* or not removing any of the adjacent muscles. Particular difficulty was met with the low marbled sample (850) which also had little intermuscular fat between the different muscles. Figure 50 demonstrates the difficulty encountered. The sample was thresholded manually with two regions – one just below the lean peak (shown in red, the first histogram) and just above (shown in green, the second histogram). Even manually setting these thresholds, the *longissimus dorsi* wasn't able to be separated as its own distinct region. There was simply nothing separating it from the adjacent muscles.

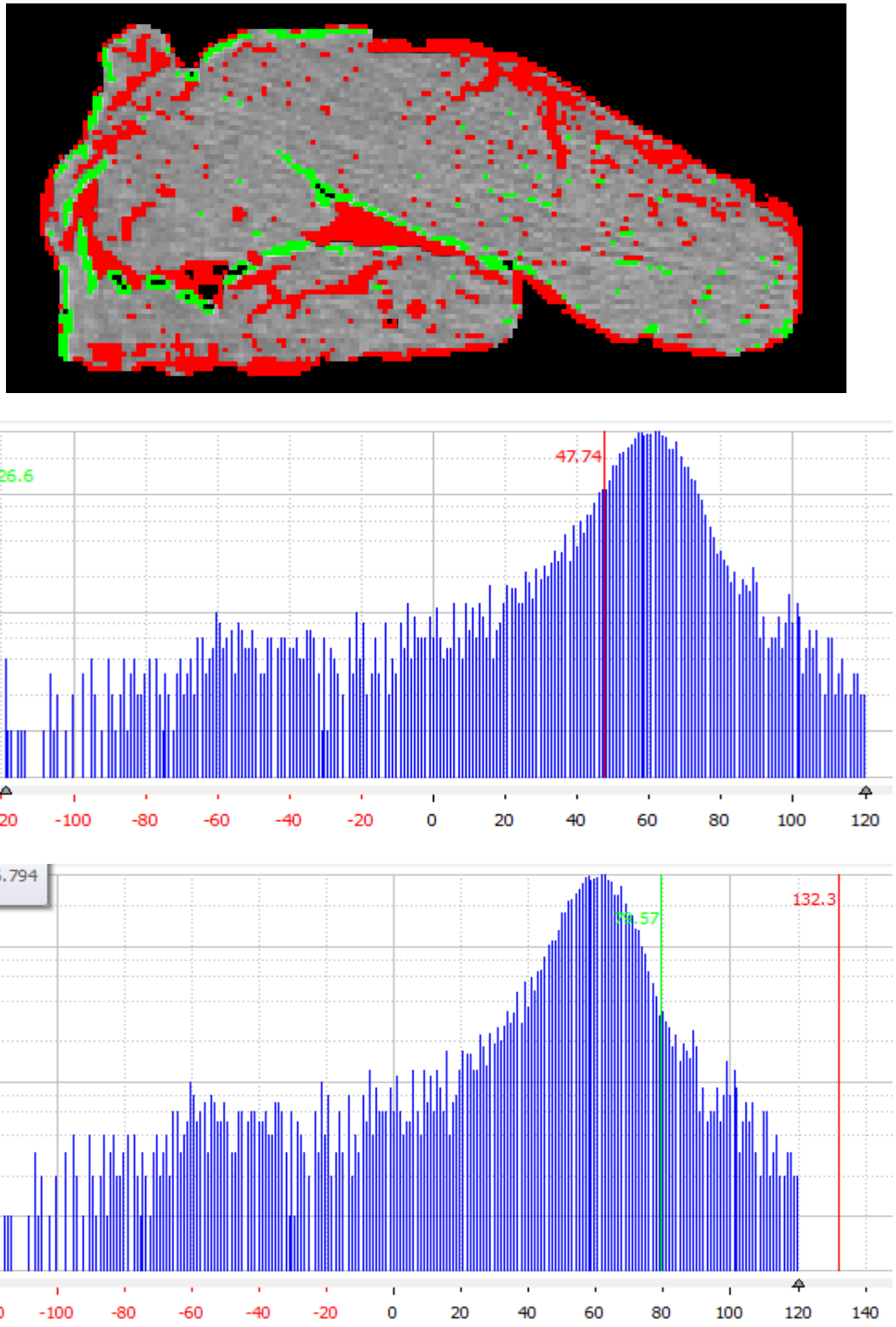

Figure 50 - 850 *Longissimus Dorsi* Isolation using thresholding. 'Fat' highlighted in red and upper boundary border pixels highlighted in green (top). Histograms showing the HU distribution in the image as well as threshold values for red (middle) and green (bottom) highlighting.

After a number of attempts, a promising approach was able to be developed. The algorithm requires further development, but the high-level approach appears sound to build upon. This algorithm was run on all boneless scans obtained (including bodies 849 and 764, and all the short loin scans) to verify the code wasn't just suitable to the 850-ribset and 766-ribset scans which were used for development. The results are shown in Table 10.

Table 10 - *Longissimus Dorsi* Segmentation Results

Slice 1	Slice 150
850-Ribset	
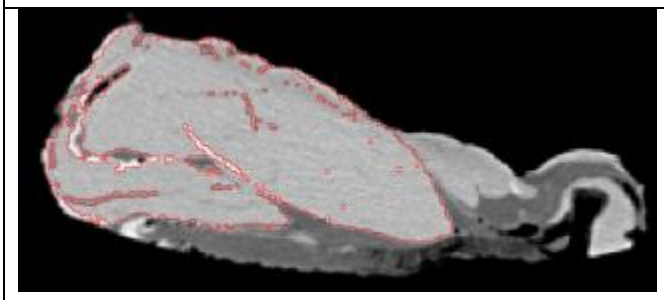	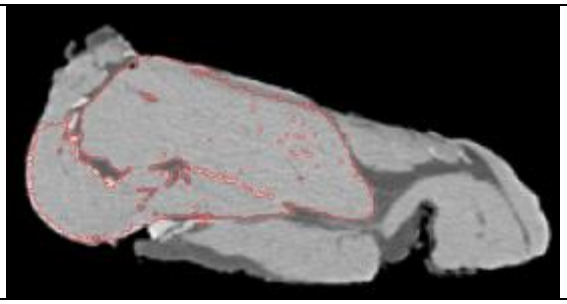
766-Ribset	
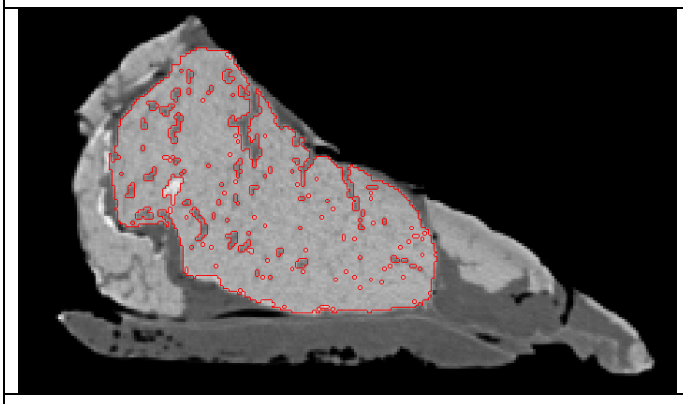	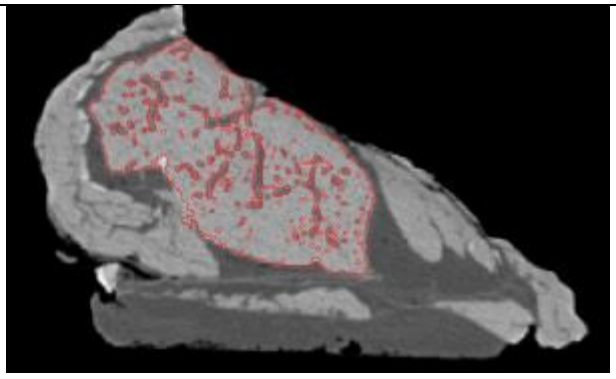
849-Ribset	
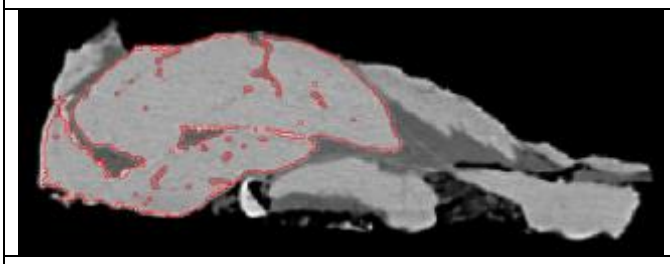	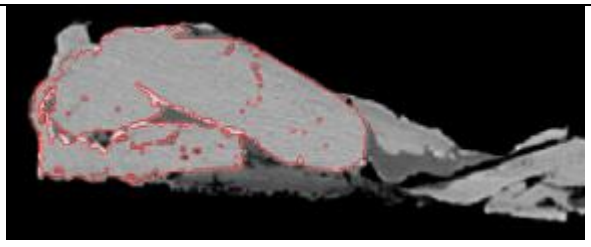
764-Ribset	
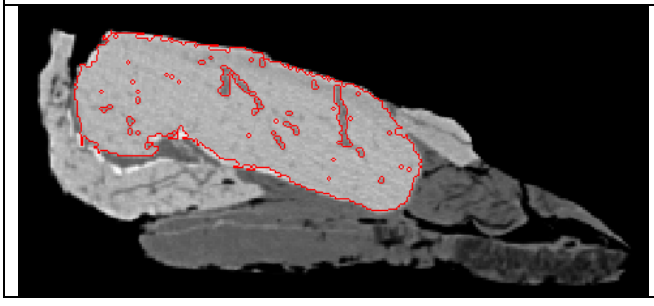	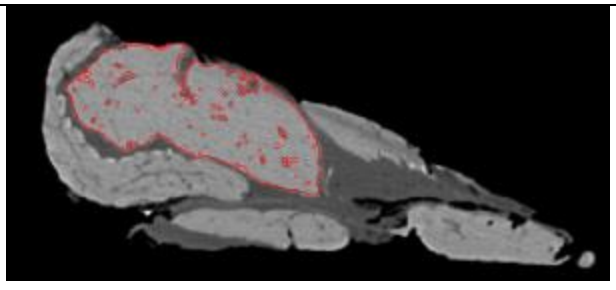

850-Short Loin

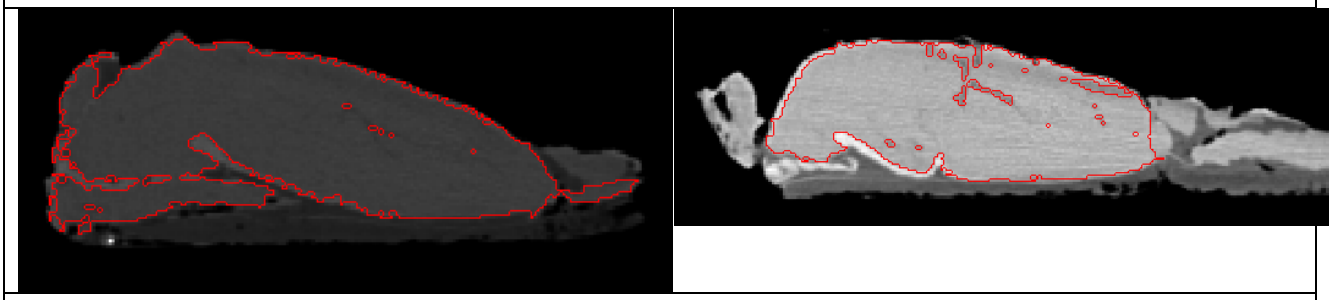

766-Short Loin

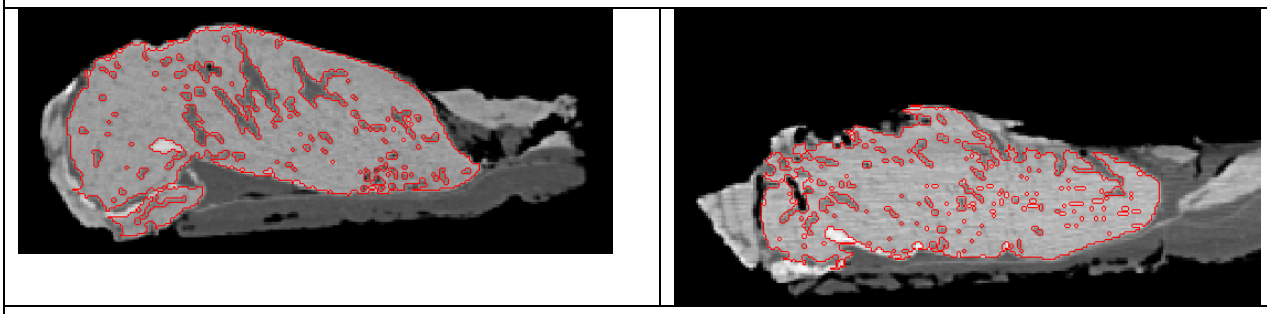

849-Short Loin

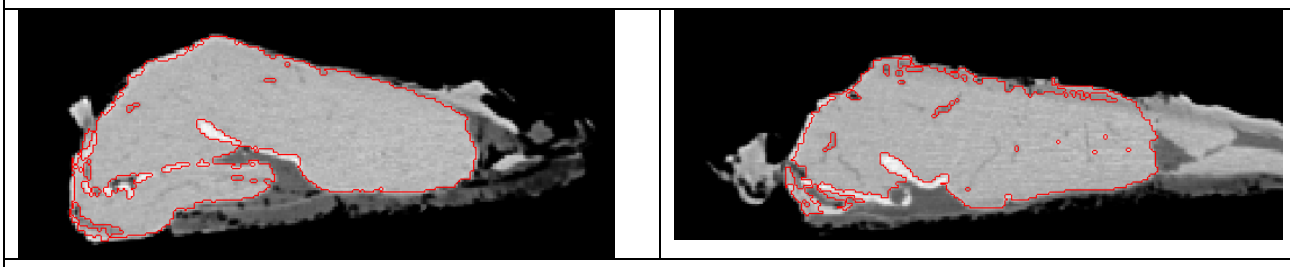

764-Short Loin

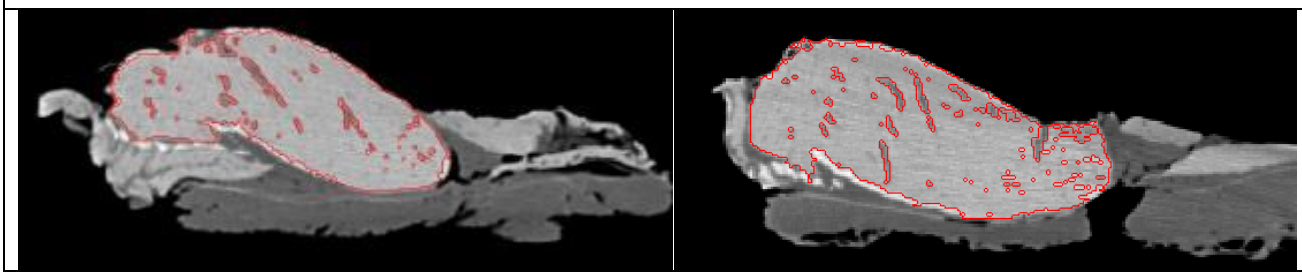

6 Striploin Intramuscular Fat Determination

6.1 Introduction

The use of MSA grading system is important in beef to determine estimates of eating quality. Marbling score is determined manually in the plant and reflects intramuscular fat (IMF) %. The amount of IMF% is linked to eating quality assessment for tenderness, juiciness and flavour. Marbling score is currently assessed in a number of cuts to attain an MSA marbling score. Rapid and accurate in-plant assessment of IMF% would enable better input into the MSA grading system. A helical computed tomography (CT) scanner has been installed at JBS Brooklyn (Siemen's Sensation 64). A model for determining chemical fat (IMF%) in beef using the Brooklyn CT scanner would allow rapid and accurate prediction of IMF% and therefore MSA marbling score.

CT has been used to determine the IMF% content of muscle in beef, lamb and pork with varying degrees of precision. The use of CT scanning alone has been shown to have low to moderate precision for IMF% prediction. Techniques with higher precision generally rely on additional information such as carcase weight and measures of fatness, making independent and rapid analysis of muscle for IMF% generally poor. This experiment has used the CT scanner in the Brooklyn plant to scan 52 beef *longissimus lumborum* samples using a number of different settings. A key aim was to determine if CT scanning can accurately determine IMF%, and what aspects of image quality can be eroded yet still achieve an adequate prediction.

There is evidence to suggest that the IMF% changes along the length of the striploin (m. *longissimus lumborum*). This study determines the magnitude of this change in IMF%, with future analysis able to improve the description of these changes in IMF% along the m. *longissimus lumborum*. This would allow for adjustments to be made to the weighting of the MSA marbling scores taken along the length of this muscle to improve the accuracy of the eating quality assessment of this muscle.

Work has been completed on the analysis of bone, fat and lean composition in beef. This involved building information on the technological factors involved when using helical CT for the application of beef OCM. The application of automated muscle isolation was also investigated using the *longissimus lumborum*, with promising results achieved.

It was thus decided to take this analysis further by conducting a large-scale controlled experiment. This trial would involve analysing a significant number of striploin samples for IMF content in order to develop models and further understand the potential challenges associated with the application. A decision was made to engage Fiona Anderson from Murdoch University as a consulting party due to her expertise in this area – she has performed a similar study on lamb (Anderson, Pethick, & Gardner, 2015). She assisted in the experimental design and performed the analysis on the data.

One of the key novel characteristics of these trials however was the clear goal of defining commercial outcomes. The aim of this milestone was to identify what commercial specifications would be required from a commercial helical scanning system to enable to perform IMF grading. Furthermore, the relationship between different hardware parameters and their effect upon accuracy was to be evaluated. Other potential value propositions which the technology may be able to offer industry were to also be considered. One side benefit from conducting this work however is that it does calibrate this machine to chemical lean for the purposes of evaluating other technologies for this application as well in the future.

The objectives of the work performed were thus defined as:

- Determine a model for the Scott CT scanner to predict chemical lean.
- Investigate the change in IMF between the anterior and posterior ends of a striploin as a potential unique value-proposition for CT technology in grading.
- Characterise how slice width and scanning power affect IMF determination accuracy. That is, what specifications would a production CT scanner require to achieve acceptable results for beef IMF calculation?
- Compare CT results with MSA grading results to evaluate value-proposition of the technology.

6.2 Trial Design

- 52 striploins were provided for analysis, along with their MSA grading data.
- For each striploin sample, approximately 6cm from the anterior and posterior ends of the striploin were removed and trimmed such that the *longissimus lumborum* muscle was isolated. The middle portion of the striploin remained intact.
- Samples were arranged with the anterior portion closest to the CT gantry, followed by the middle portion, and finally the posterior portion (Figure 51).
- Samples were arranged on a bed and scanned two at a time (Figure 51).
- A phantom was scanned with each set for future reference.

Figure 51 - Sample setup in CT scanner

Each set of samples were scanned at two settings – a ‘High Quality’ setting to serve as a reference for this project and in the future; and a ‘Line Speed’ setting – a fast scan with lower exposure.

- The effect of increasing slice width to increase cycle time will be evaluated by combining the data between for adjacent slices.
- Immediately following scanning, the cranial and caudal samples were vacuum packed and frozen, before being sent to Murdoch University for IMF% determination. Samples were freeze dried using a ScanVac CoolSafeTM freeze drier and IMF % of each muscle sample determined using a near infrared procedure (NIR). NIR measurements were taken using a Spectro Star 2400 and all samples were subsequently calibrated against chloroform solvent extraction.
- A detailed register of the MSA grading data for the samples which were provided by the processor. Figure 52 is a graph showing the distribution of marbling scores that were obtained. The vertical axis is the MSA marbling score and the horizontal axis is the sample number. Of interest is the amount of coverage vertically in the graph.
-

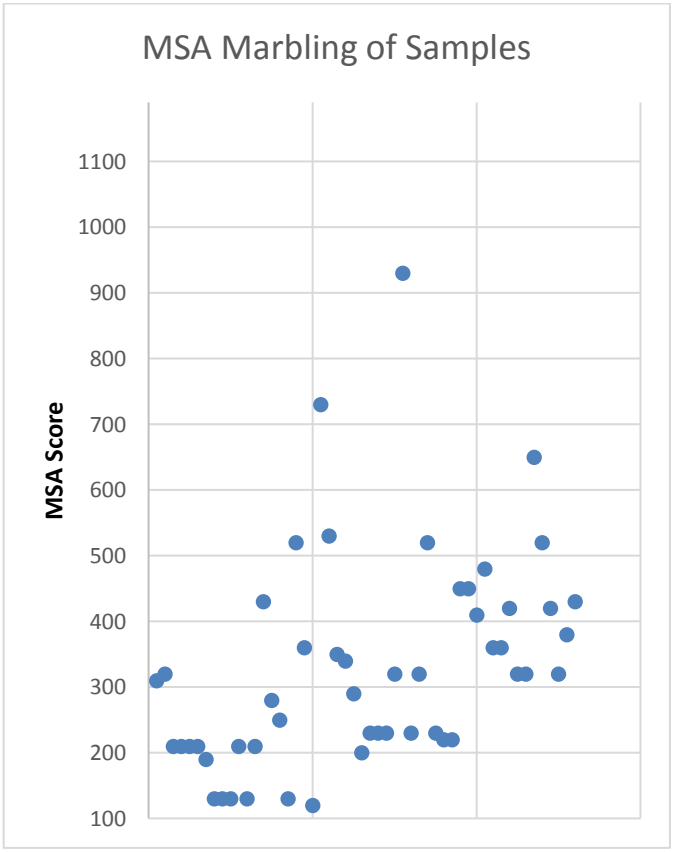

Figure 52 - MSA Marbling Score of Samples

It can be seen that there was a lack of high-marbled samples in the dataset. A specific effort was made to source high-marbled striploins and two more trials were conducted with the same methodology. Figure 53 shows the final spread of the striploins with the new samples included. It can be seen that the marbling range is covered much more effectively.

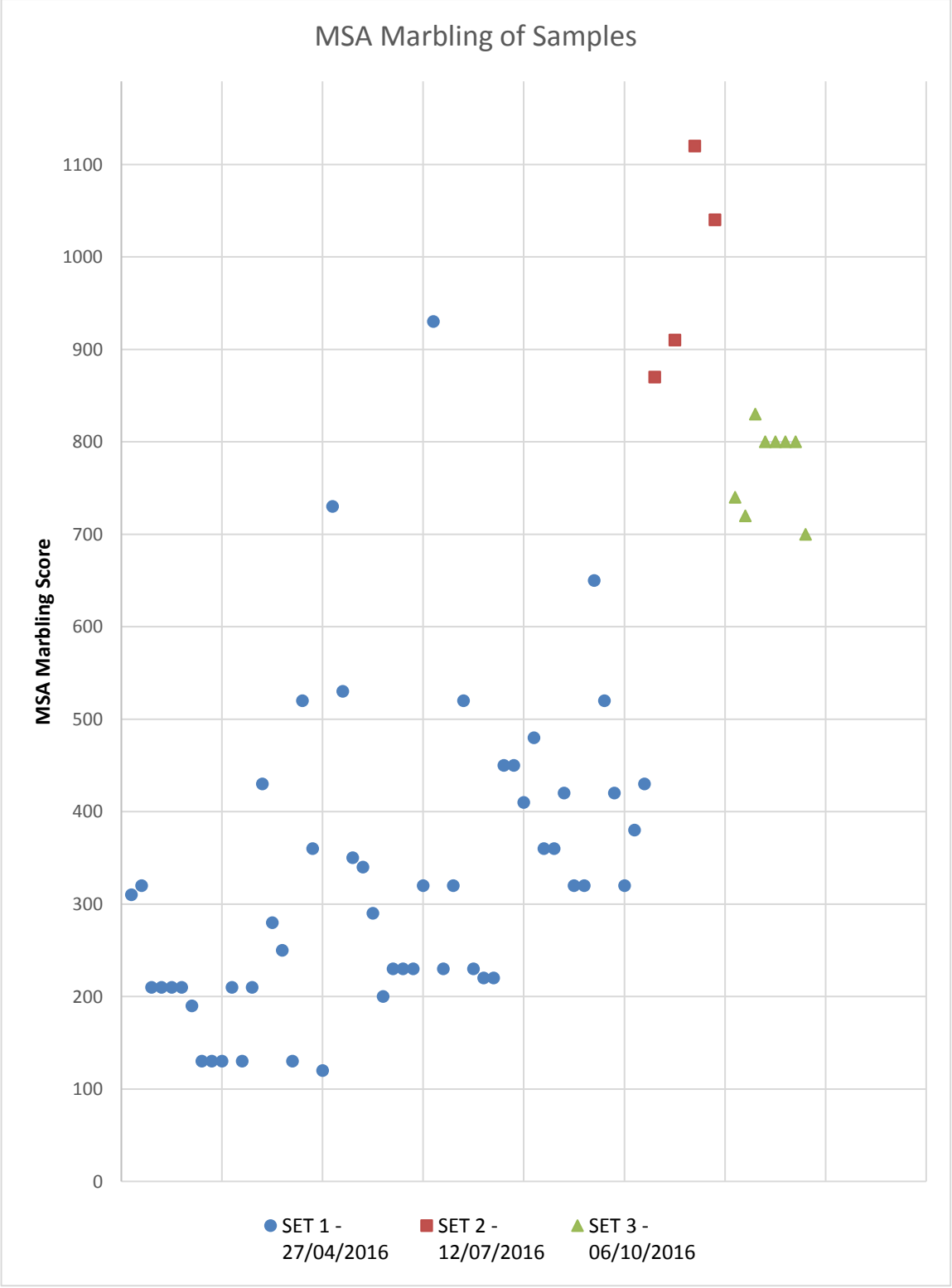

Figure 53 - MSA marbling scores for striploin samples trialled - final

The data was then analysed using a number of different processing methods to build a number of models for the prediction of intramuscular fat content. The analysis also examined:

- Whether a difference existed between the anterior and posterior portions of the *longissimus lumborum*
- How the 'line-speed' scan setting affected prediction compared to the 'high-quality' setting

- The impact of different acquisition slice widths to prediction
- The effect of including additional information to the models

Fiona's paper on the trials and analysis is attached in its entirety in Appendix C – Striploin Intramuscular Fat Modelling Report (F. Anderson, Murdoch University).

7 Assessing Beef Automation

7.1 Introduction

X-ray absorptiometry has been a significant enabler of automated cutting in the red meat industry through its single energy (SEXA) and dual energy (DEXA) modalities. Due to natural variation which occurs across animals, to cut bones one must identify bones. Modelling is often not able to give the accurate results required. A multispectral version of the technology (MEXA) offers further opportunities in the area of automation although the opportunities and limitations it presents is yet to be examined fully.

One drawback of these technologies however is that they distort the image data. Firstly, the image formed is 'flattened'. A feature can be identified in an x-ray image but its location in 3D space can be at any point along a vector originating at the x-ray tube and terminating at the corresponding pixel on a detector. This is shown in Figure 54 whereby the feature (point *a* on the carcase) identified in the x-ray image (represented by pixel *a* on the detector) could exist along the ray path (in pink) from the source to the detector.

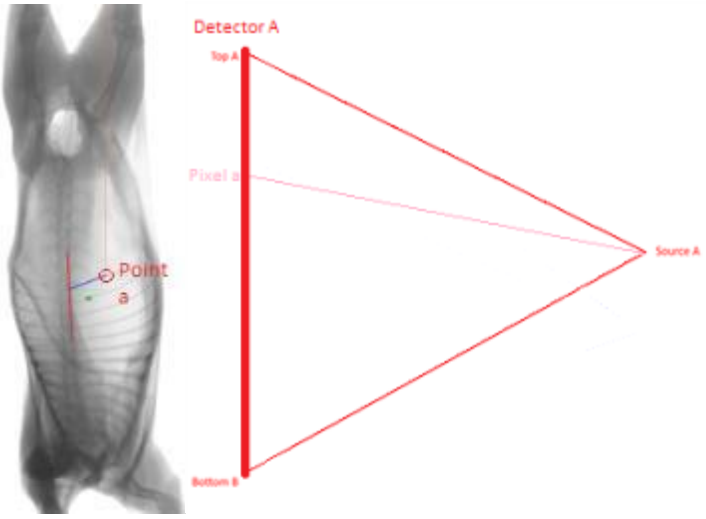

Figure 54 - Projection of a point onto an x-ray image pixel

A number of strategies can be used to ascertain the 3D location of features from the 2D x-ray images, but they have varying levels of success and aren't applicable for all applications.

This flattening of the x-ray data also reduces the clarity of certain points of interest due to the geometry of the fan beam. One example of this is the vertebrae. Figure 55 shows a DEXA image

of a beef carcase. It can be seen in the centre of the image some separation of the vertebrae is visible however this ability falls away as the beam starts to cut ‘across’ the vertebrae at an angle. In addition to this, the other features around the spine drastically compromise the presentation of the vertebrae. Optimising DEXA hardware (including using more power) in this situation will only yield a certain level of benefit.

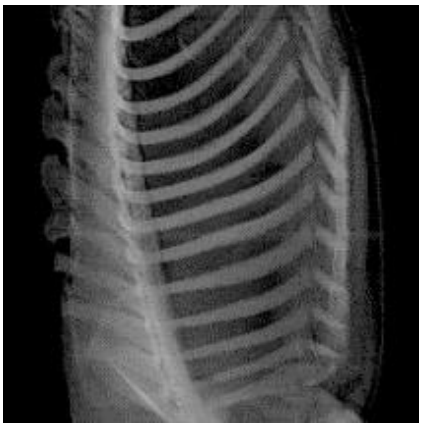

Figure 55 - DEXA image of a beef carcase

There are also features that aren’t able to be identified in DEXA images such as lymph nodes.

A CT image provides the gold standard for such applications. The inherent 3D nature of the data means that no extrapolation is required to obtain 3D information for features of interest. The nature of CT also results in an undistorted view of the bone structure. The limitation in identifying a feature is thus the resolution of the system without any influence of geometry.

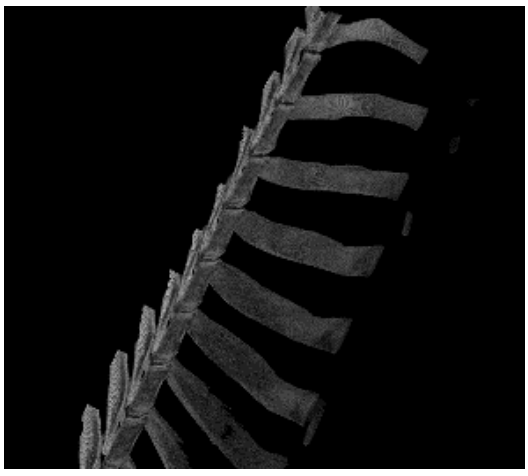

Figure 56 - CT image of a beef carcase with the spine isolated

We investigated the ability of CT to identify cut paths currently deemed challenging to projective x-ray absorptiometry images. The cuts evaluated include:

- A spine cut

- The rib 1 junction
- A cut using a non-bone feature
- Fat trim
- Chine Removal

7.2 Spine Cut

In order to assess a spine cut, a CT scan of a beef forequarter was analysed (Figure 57).

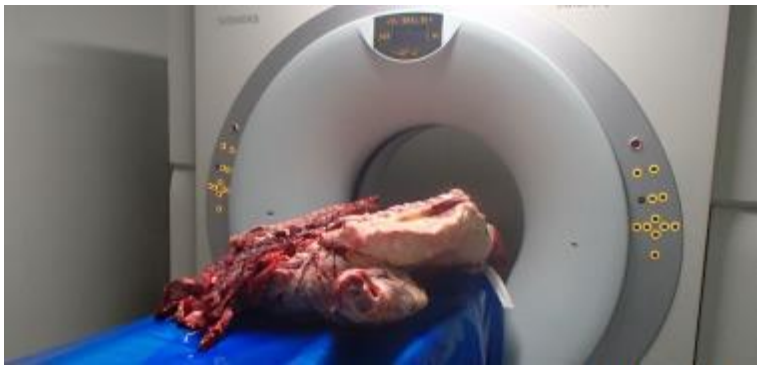

Figure 57 - Whole Beef (ox) Forequarter scanned in CT scanner

The cut investigated will be at the vertebrae between ribs 3 and 4. This was selected due to its challenging nature. It's a very thick part of the carcase and the scapular is in the way. Both these factors would make this cut very difficult to detect using DEXA as seen in Figure 58. If a cut can be placed here, it should be possible to place at any vertebrae using a similar methodology.

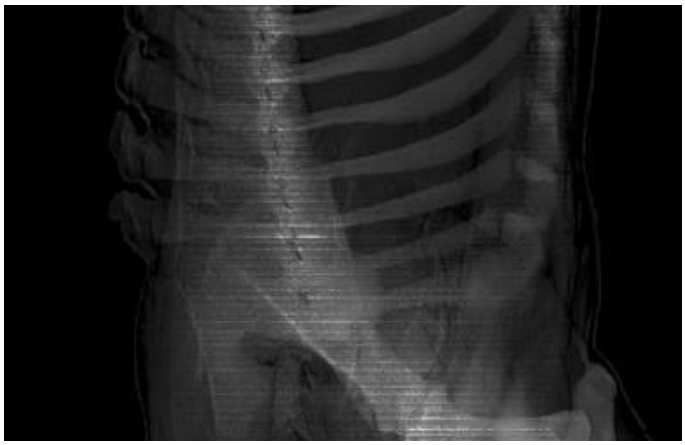

Figure 58 - DEXA image of rib 1 junction

First the bone structure was isolated for the forequarter and the rib and vertebrae structure isolated from the scapula, humerus and brisket as shown in Figure 59.

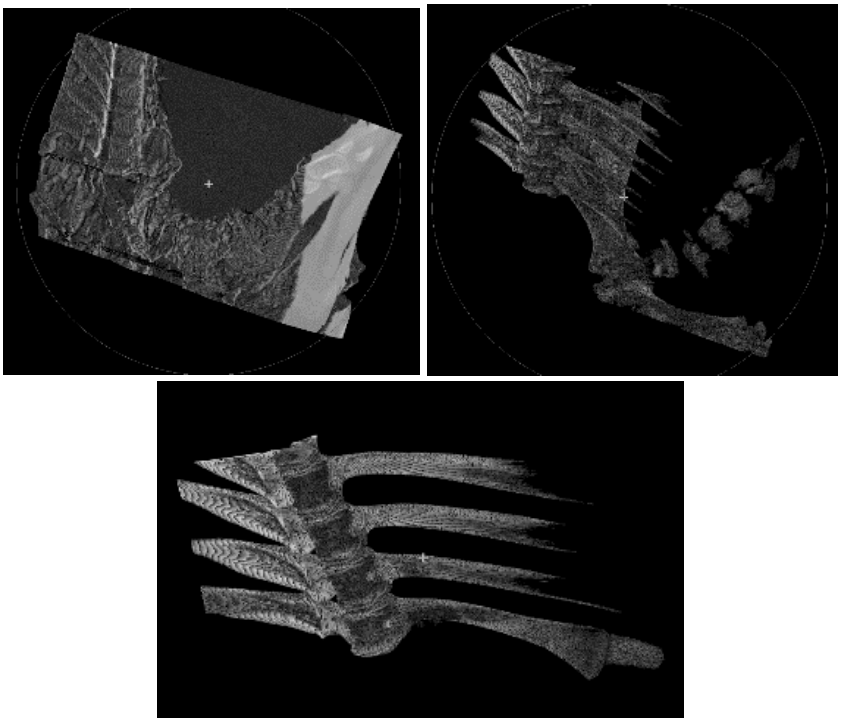

Figure 59 - Isolation of ribs and chine

It can be noted that the lower ribs are washed out on this scan as a result of how the sample was scanned. Realistically the sample was too large to scan with this CT scanner with ideal positioning. Different scan parameters should have also been used but these would have limited the scan length. The primary goal of this scan was to capture as much information as possible of the spine and rib 1 junction and this was still achieved. A scan was also taken of a bull forequarter which was split down the middle caudocranially. This scan did not exhibit the same issues with the rib ends despite the carcase being larger and thicker in this area (see Figure 60).

Figure 60 - CT scan of the ventral half of a bull forequarter

To process the data, the viewpoint was first adjusted to the chine bone and rendered by distance. It can be seen the separation between the vertebrae become quite visible. A rib counting algorithm is then used to identify the ribs and thus, a region of interest for the spine cut. This process is shown in Figure 61. It can be seen in the last image however that cutting at this

junction would actually cut into the rib behind it. The algorithm could thus be modified to adjust the placement of this cut relative to the joint of the rib to the spine as desired.

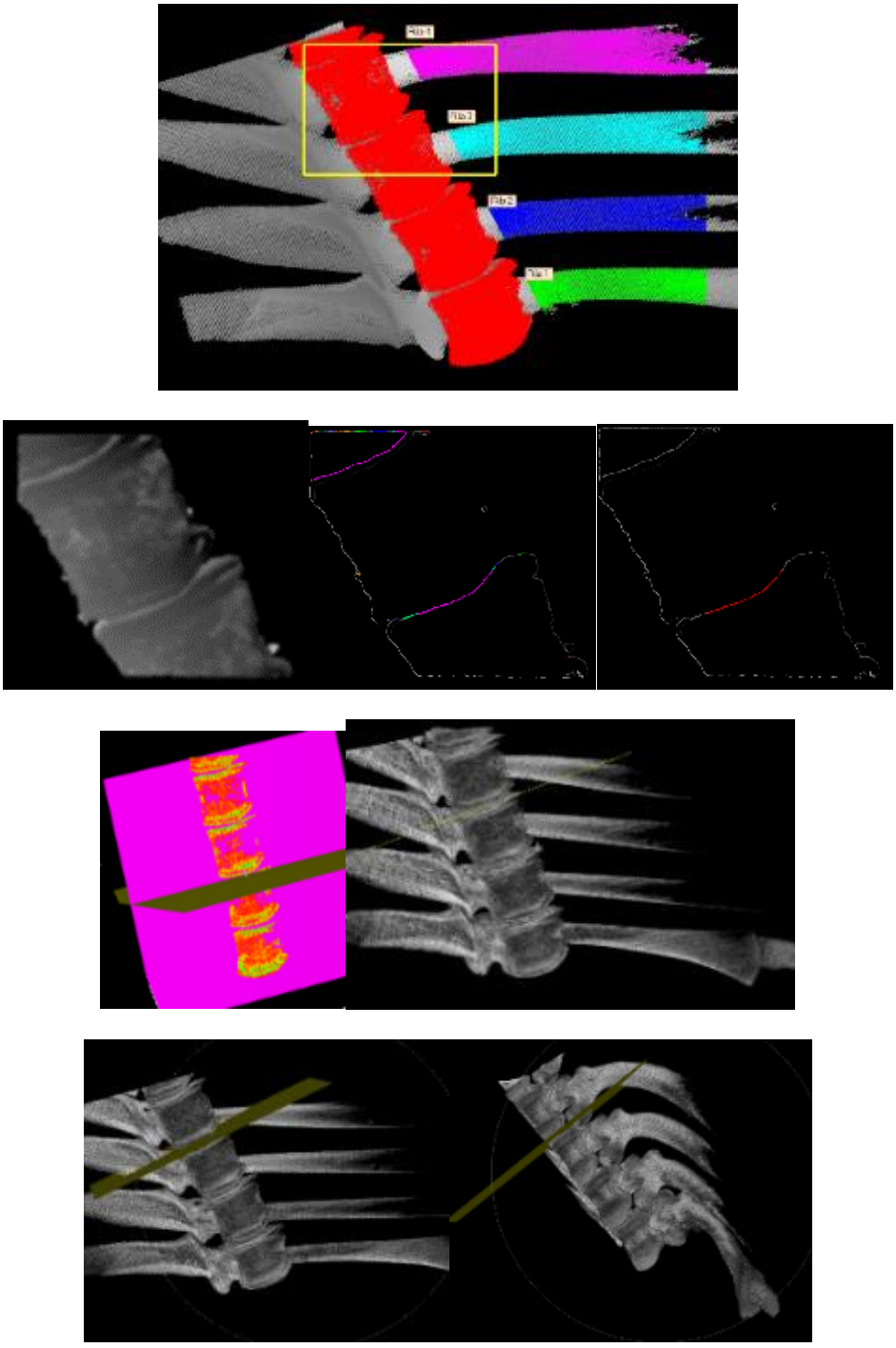

Figure 61 - Isolation of cut path across spine between ribs 3 and 4

It can be seen that the 3D data from the CT image drastically improves the accuracy and robustness of the application. Having the internal structure means that regions of interest can be more tightly defined and artefacts removed. A key example of this benefit is being able to remove the scapula to allow better presentation of the spine. This is not something that can be done on a projective x-ray image. Similarly, the ribs are able to be isolated more clearly. Utilising CT for

spine cuts would thus enable a much more robust solution for the placement of spine cuts. This can be seen at even the fastest scan speed available for this CT scanner.

This result was then cross checked against the scan performed at the ‘fastest’ available settings for the scanner which equated to a scan speed of approximately 55mm/s with no issues (Figure 62). It is thus envisioned that a scanner designed to operate at line speeds (ca. 500 sides per hour+) would be capable of performing all spine cuts accurately and reliably.

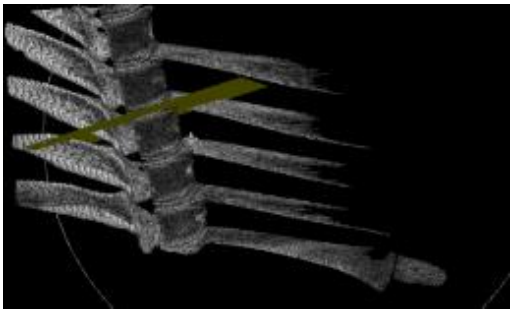

Figure 62 - Cut path with data obtained with 'fastest' scan speed

7.3 Rib 1 Junction

The rib 1 junction is one of the two points of interest which defines the brisket cut. This point is in a particularly challenging part of the carcase to image due to the thickness of this tissue in this area. This makes it challenging to obtain a clear image of the junction which is low in noise using projective x-ray technology. This is made more challenging when some movement is present as this creates artefacts in the image.

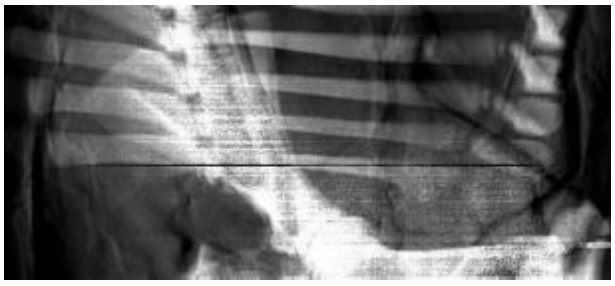

Figure 63 - Presentation of rib 1 junction in a DEXA image

The presentation of the rib 1 junction also varies significantly between carcases, as shown in Figure 64. For older carcases, the cartilage in the junction has essentially calcified meaning there is no ‘junction’ to detect strictly speaking.

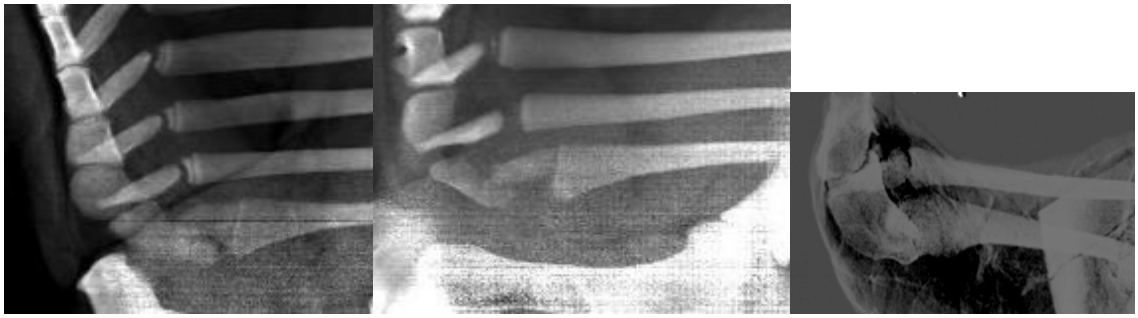

Figure 64 - Differing presentations of the rib 1 junction

One other issue which may present in certain plants is stringing up of the leg. When this is done, the humerus can completely occlude the rib 1 junction, making direct identification impossible with a projective x-ray image. Figure 65 shows an x-ray image of a carcase where the foreleg has been 'strung up'. It can be seen that this causes humerus to cover the rib 1 junction entirely. As demonstrated in section 7.2, this wouldn't be an issue with the 3D CT data as the humerus can be isolated from the rib structure.

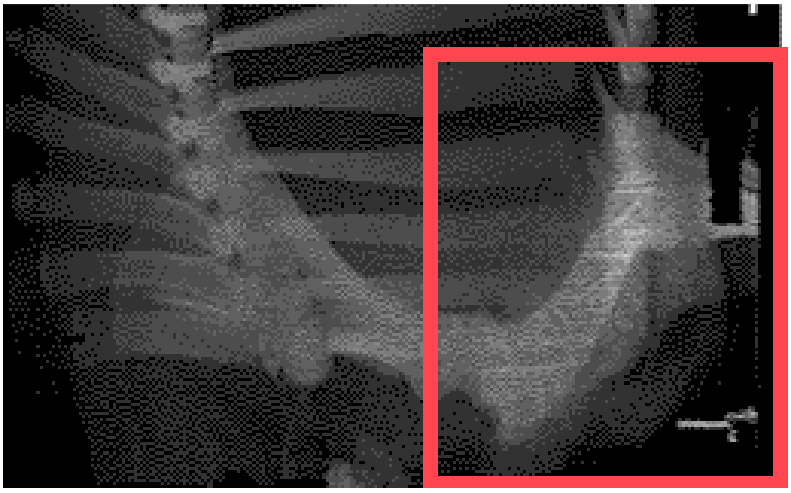

Figure 65 - Occlusion of the rib 1 junction caused by a 'strung leg'

The scan of the forequarter for an ox (as per section 7.2) was first evaluated as it possessed the entire rib 1. As above, the ribs were isolated from the humerus and any other surrounding features (Figure 66). Rib 1 was then selected.

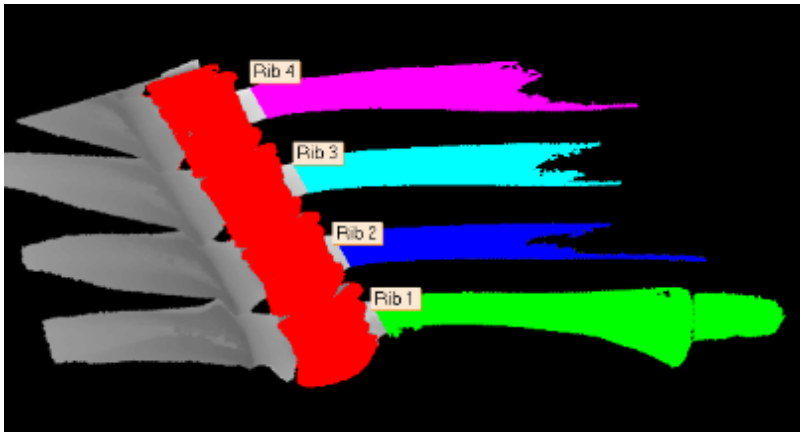

Figure 66 - isolation and identification of ribs and chine

In this example, the rib 1 junction was clearly visible with the bone isolated from soft tissue (Figure 67).

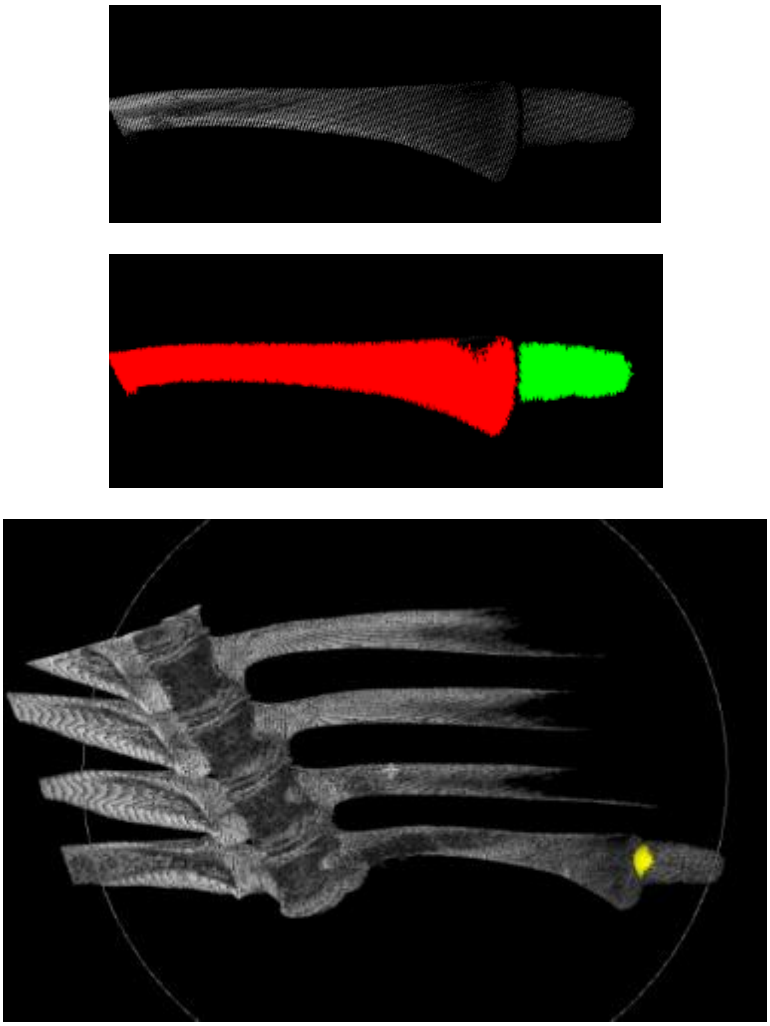

Figure 67 - Identification of the rib 1 junction from the CT data

A CT scan was also taken of a cow. Similar to the bull, the forequarter had to be divided in half to be able to fit inside the CT scanner. Unfortunately, this sample was damaged in that a cut was placed in rib 1. This hasn't affected the ability to assess the cut. The important thing is that this sample exhibited a much higher level of calcification of the rib 1 junction. It was also more present in the brisket too which meant that rib 1 and its sternal segment weren't easily separated from the brisket as with the ox sample above. Thus, a two-stage filter was applied to get rid of other artefacts first. Note how rib 1 has been split due to being cut in two. These two segments were isolated and joined (Figure 68). Unlike the ox sample however, the rib hasn't been isolated from its sternal segment. It is still visible however, just not as clearly separated.

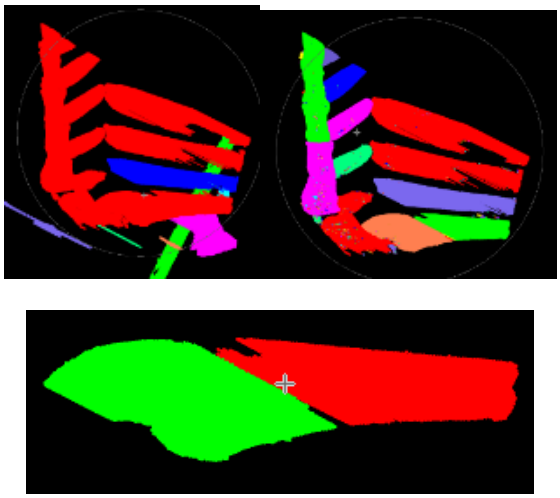

Figure 68 - Isolation of rib 1 and sternal segment for an old cow

Both examples were processed using the fastest CT scanning parameters available. It can be seen that, while more involved for the case of the cow which possessed a fairly high level of calcification in its joints, the rib 1 junction was still able to identified (Figure 69). There is thus a high degree of confidence that this task would be able to be accomplished even with further image quality degradation resulting from scanning at line speeds. Such a solution should be able to identify the rib 1 junction directly, even in the case of old cattle with calcified joints.

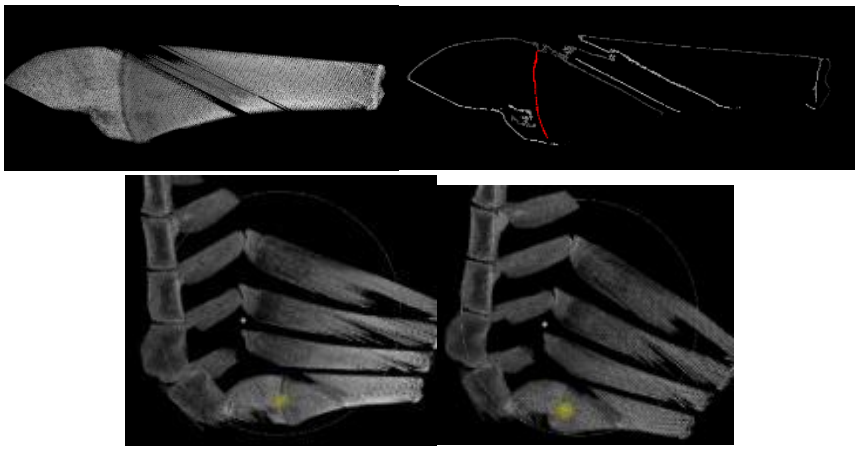

Figure 69 - Identification of the rib 1 junction for an old cow

7.4 Cut using a non-bone feature

There are a number of cuts which are performed on a carcase which are specified by non-bone features. In some instances, this is to facilitate the use of a manual operator – cut reference points often need to be identifiable to a human operator. The use of sensing technologies, particularly x-ray which is capable of imaging subsurface features, can present an opportunity to identify features which are actually more ideal but are unable to be identified by a human. The upshot of this is there are features which aren't identifiable using projective x-ray. Even features which are visible to the human eye can be extremely difficult to find automatically using cameras due to the immense amount of variation experienced – a human brain is the most efficient pattern matching machine in existence.

An example of one of these cuts is shown in Figure 70. This cut is used to separate the rump from the butt. According to the AusMeat specification, this cut commences at the subiliac lymph node to a point cranial to the acetabulum to the ischiatic lymph node and the ventral portion of the flank. Visually, the cut passes between the last coccygeal vertebrae and hip bone, removing approximately 10mm off the tip of the femur.

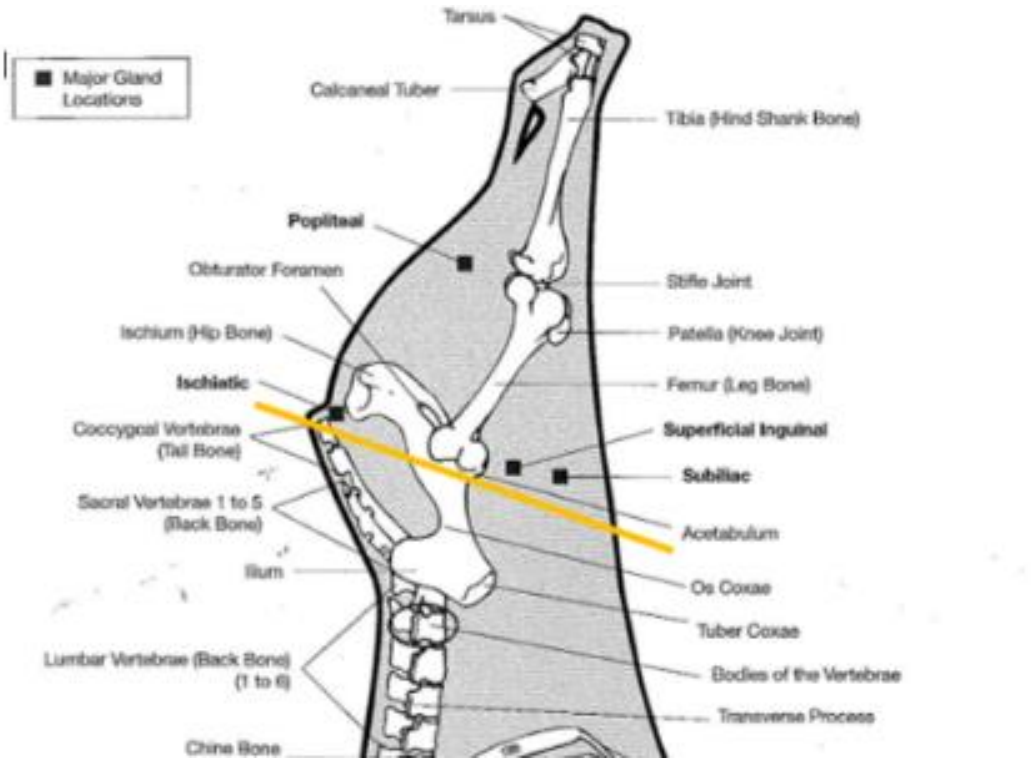

Figure 70 - Example cut in beef utilising a lymph node as a point of reference

A lymph node should be identifiable in a CT image, with an approximate HU range of 0 to 100, a range which also contains skeletal muscle. A CT scan of a hindquarter was analysed to see if the lymph node was visible. CT technology is thus able to identify lymph nodes. The application however would be challenging and sufficient image quality would be required to achieve automated isolation (at least in most slices) from adjacent tissue. Trials would have to be conducted with a larger sample size to confirm presentation for the lymph nodes of interest for

given applications. Particularly of note would be the amount of fat around the lymph nodes to facilitate isolation. For a scan of a beef hindquarter, this lymph node was able to be identified, but only manually (Figure 71, Figure 72, Figure 73).

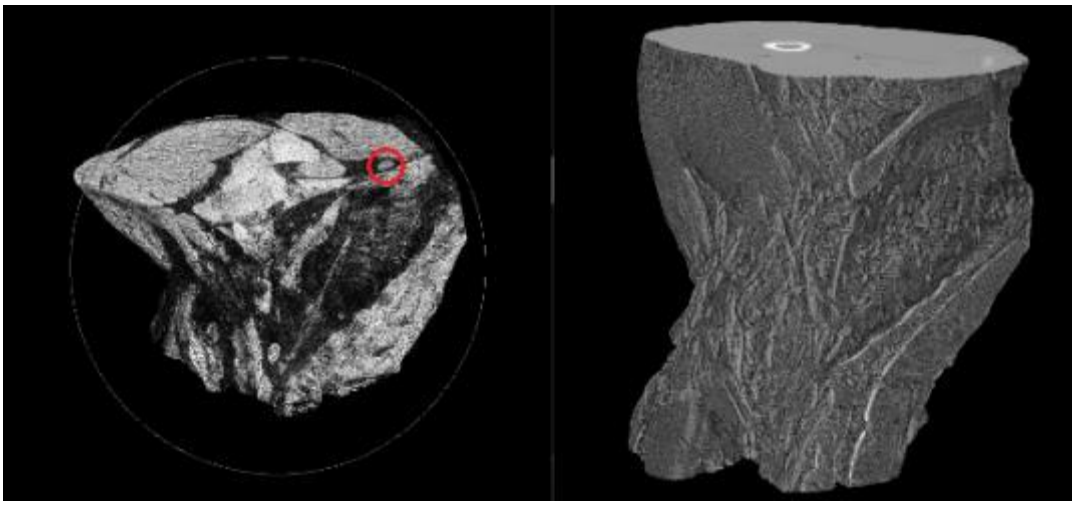

Figure 71 - Visual identification of lymph node in CT data

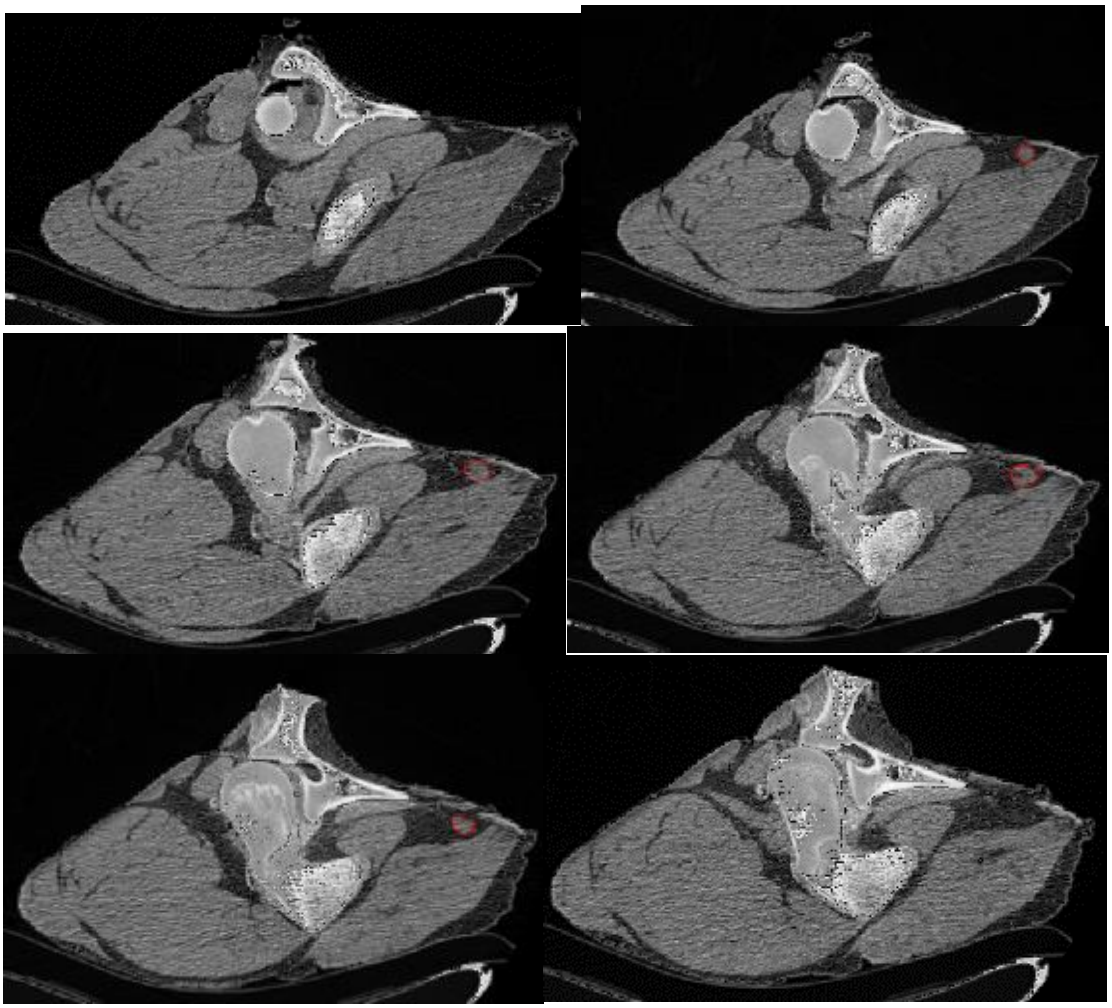

Figure 72 - Presentation of lymph node in a number of slices

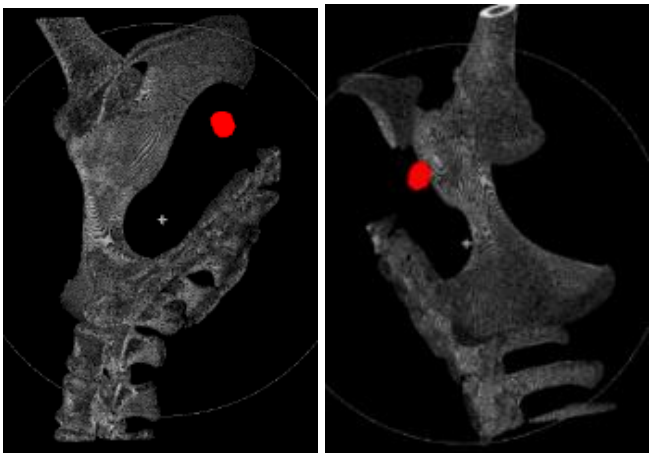

Figure 73 - Lymph node location in CT data

7.5 Fat Trim

When boneless primals are sold to a customer, a certain amount of subcutaneous fat may be specified. The trimming of fat is currently done by an operator manually based on the fat-level visible at the two exposed faces. It is impossible for them to know however how this is varying across the length of the primal. This can result in claims from customers for excessive fat depth when primals are sliced (Figure 74).

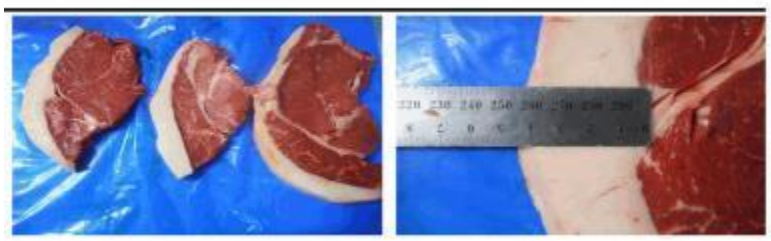

Figure 74 - Example issue of returned product due to excessive fat

Such an application is not possible using DEXA, which is 2D. As there are no distinct features to identify, using multiple points of view won't work to recreate the 3D geometry. It is also a surface which is of interest which requires a lot more 3D information to be calculated as opposed to a cut requiring two or so discrete points to be identified in 3D space. A CT-based solution would offer a high level of accuracy and robustness.

A scan of a beef short loin was analysed for this application (Figure 75). The fat voxels were isolated using HU values and the subcutaneous fat was separated from the intermuscular and intramuscular fat (Figure 76). With the subcutaneous fat layer isolated, excess fat was isolated to provide a final fat depth of 5mm (Figure 77). The resulting ideal surface could then be defined as a complex cut for a robot with a knife to perform the trimming. The compromise between accuracy and cycle time for the given application and processor would define the complexity of this cut path.

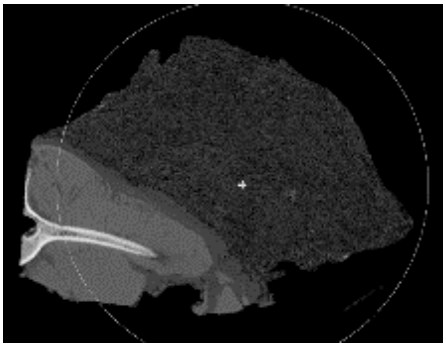

Figure 75 - CT scan of short loin

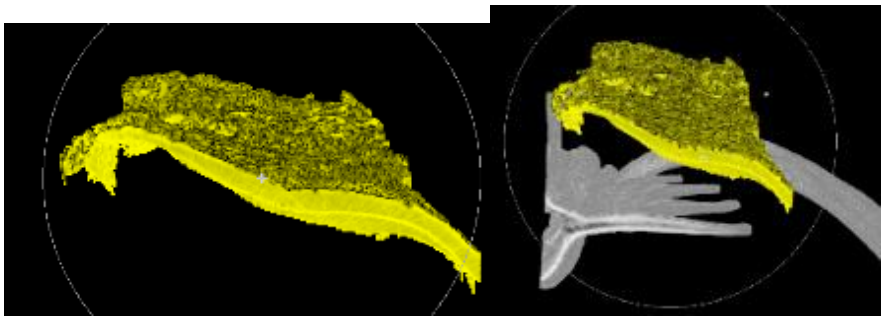

Figure 76 - Isolation of subcutaneous fat layer for a short loin

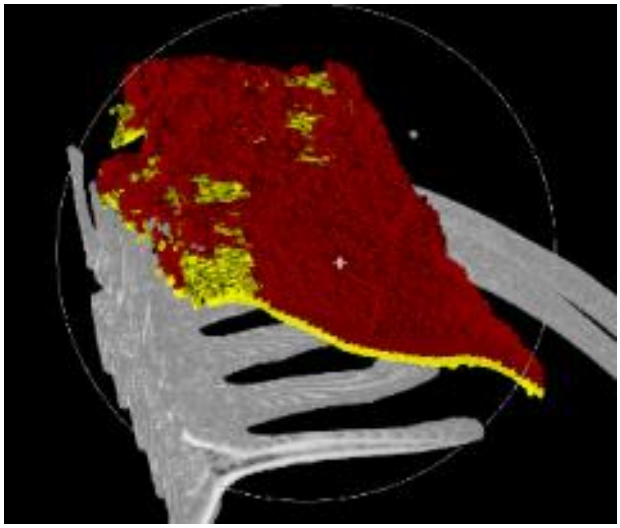

Figure 77 - Trimming result. Trimmed fat shown in red

It can be seen that this application lends itself readily to CT technology. This application was able to be achieved using the 'fastest' scan available but this would need to be examined in further detail. As the quality of the image degrades, the ability to differentiate between fat and lean also degrades. It appears that this effect isn't as severe for subcutaneous fat however, versus intramuscular fat, because of the larger volume. This would be the primary consideration in specifying a system however.

7.6 Beef Chine Removal

The chine removal process for beef currently occurs through the placement of a cut using a bandsaw across the chine bone to remove it from the rest of the primal (Figure 78). Along this path, there are intermittent bulbous protrusions into the *longissimus dorsi* muscle (referred to as 'buttons'). This is shown in the right hand slice of Figure 79. The ideal cut path to perform is thus variable based on a trade-off between maximising yield and further processing of the primal by removing the 'buttons' left within the primal. It is envisioned than an automated solution should allow for an adjustable parameter to define this.

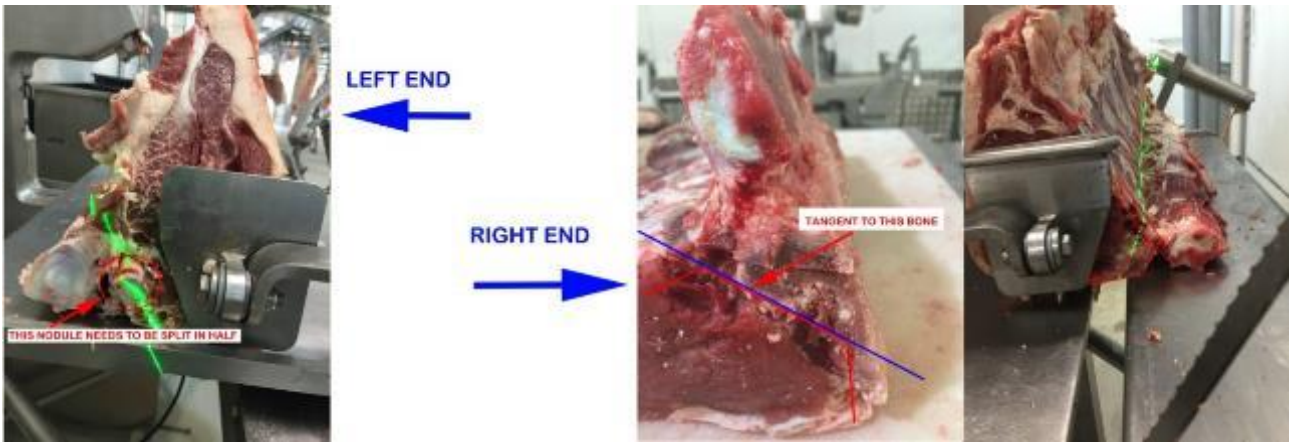

Figure 78 - Chine removal cut location

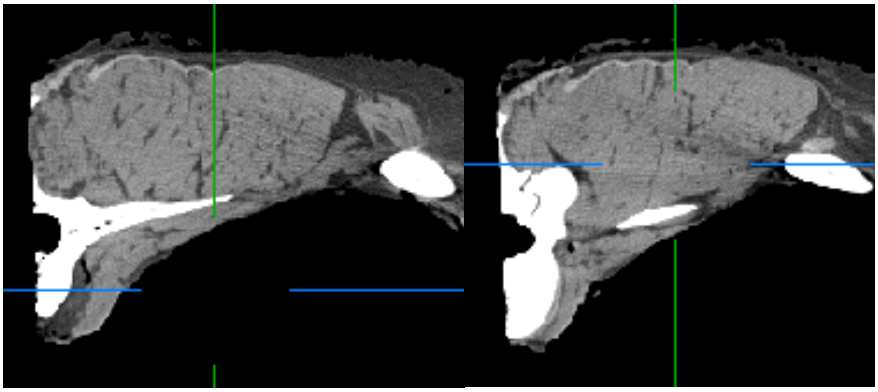

Figure 79 - Protrusions from chine bone into *longissimus dorsi* muscle

This application is challenging for DEXA as the cut is defined by the subsurface 'buttons' along with the chine bone. CT would be the ideal sensing technology as it provides detailed and complete 3D information for the profile that is looking to be cut. This complete information would enable a more robust solution, a higher level of accuracy as well as a greater level of customisation for defining the cut. An algorithm was built characterising this cut by identifying these buttons (Figure 80). The cutting plane can be adjusted by a user-customisable setting for how much 'button' to leave embedded in the loin (as indicated by the yellow and green cut planes in the last image).

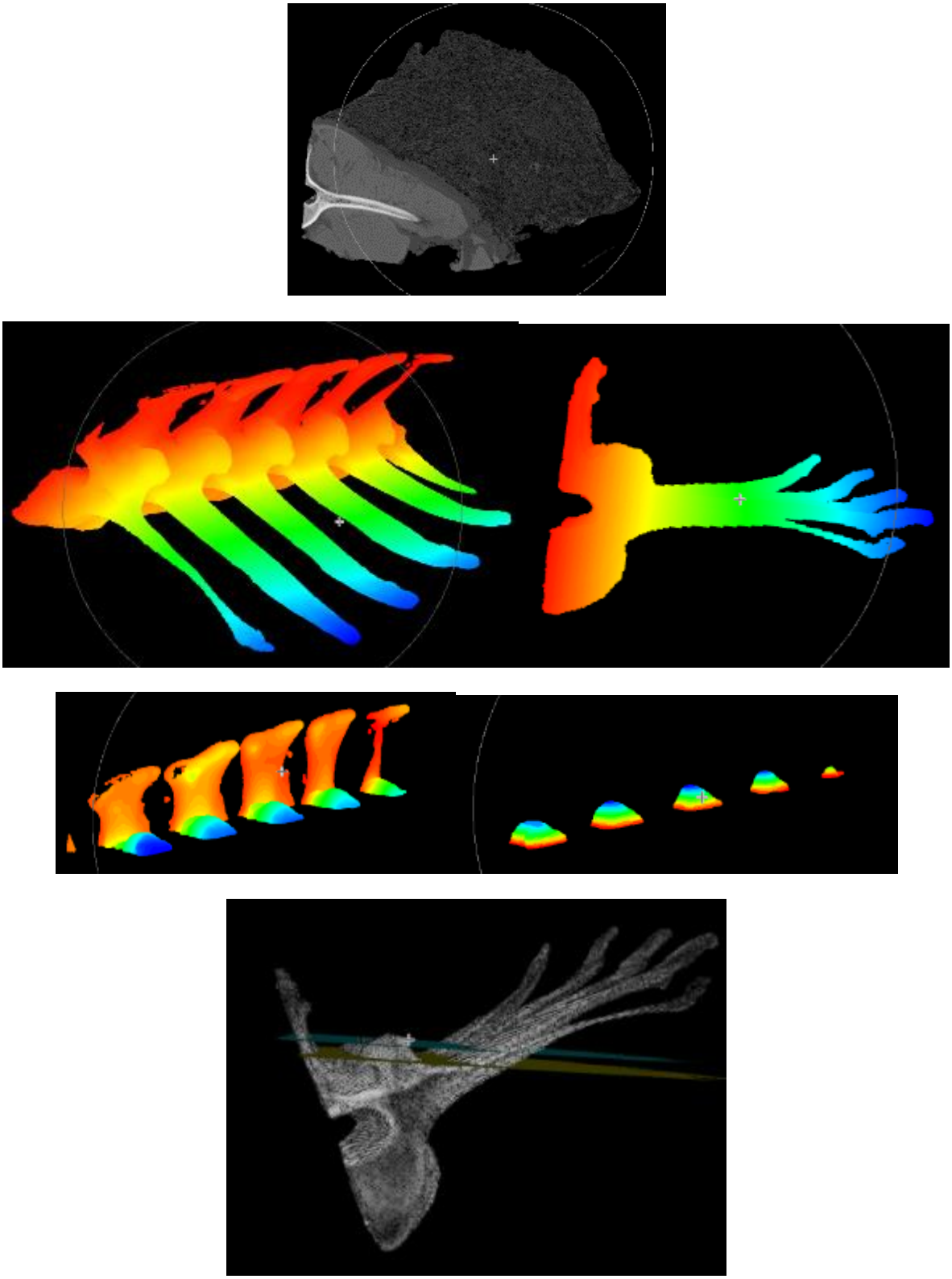

Figure 80 - Identification of chine removal cut paths

CT technology thus offers an opportunity to perform an accurate chine removal cut along with the ability to adjust it for maximal removal of the ‘buttons’, minimal loss of yield or somewhere in between. This would be able to be done dynamically, based on the value of the primal.

7.7 Conclusion

It can be seen that the 3D provided by the CT system makes it an extremely powerful enabler for beef automation. Cuts involving bones in particular are able to cope easily with the degradation in data seen by scanning at the 'fast' setting. Cuts involving non-bone features would have to be evaluated more closely as degradation of image quality affects the ability to differentiate between different soft tissues more noticeably. Further degradation of noise can be introduced manually to investigate their effect on the ability to identify the features of note.

This work forms a baseline for building the confidence that automation tasks which may not be able to be achieved using projective x-ray technology (e.g. DEXA or MEXA) would be achievable with the added data and 3D information presented by a CT system.

8 Beam Hardening Evaluation

8.1 Background

Beam hardening is an effect encountered with CT imaging due to using polychromatic x-rays. As these x-rays pass through an object, the lower energy photons are absorbed preferentially, increasing the net energy of the beam as it passes through. This can result in 'streaking' artefacts around bone. When scanning bone-in primals, streaking artefacts can often be visually recognised, particularly in areas adjacent to ribs (Figure 81).

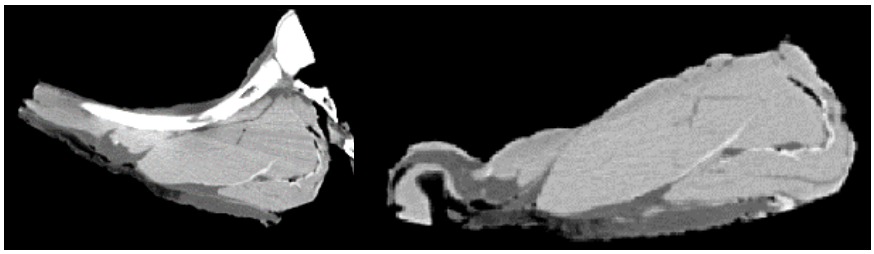

Figure 81 – CT slices of a striploin sample with bone-in (left) and boneless (right)

Work has been completed in this project to predict the intramuscular fat content of the *longissimus lumborum* muscle within boneless striploins. This model was able to achieve an R^2 of 0.82 with an RMSE of 2.01% IMF. This section of the report aims to investigate the effect beam hardening may have on such models to ascertain its effect on intramuscular fat calculation.

8.2 Method

The bone-in ribsets and striploins of four carcases were obtained. They were then CT-scanned with two different scan settings – a 'high-quality' and a 'high-speed' setting. These are the same settings as used during the striploin scanning trials.

The ribsets and striploins were first scanned bone-in. The primals were then boned out and rescanned. Unlike the striploin scanning trials, no portion of the *longissimus thoracis et lumborum* was separated and denuded. Similarly, no chemical testing was performed on these samples. A CT slice for a bone-in versus a boneless scan of the same striploin is shown in Figure 81. Figure 82 and Figure 83 show the striploin being CT scanned before and after boning out.

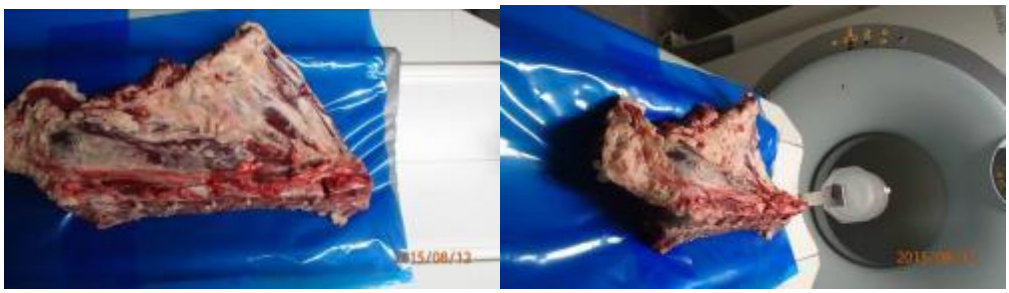

Figure 82 - CT scan of a bone-in striploin

Figure 83 - CT scan of the same striploin as Figure 82 after being boned out

From the CT data acquired, 100 slices were selected from the grading site for each scan. This equates to approximately 6cm. As the product wasn't denuded, the *longissimus thoracis et lumborum* muscle was manually isolated from each slice as carefully as possible (Figure 84). Grey-level histograms were then compiled for each of the samples. The average and standard deviation of the intensity values were also calculated. These data were then compared and contrasted to ascertain what effect, if any, beam hardening caused as a result of scanning bone-in versus boneless.

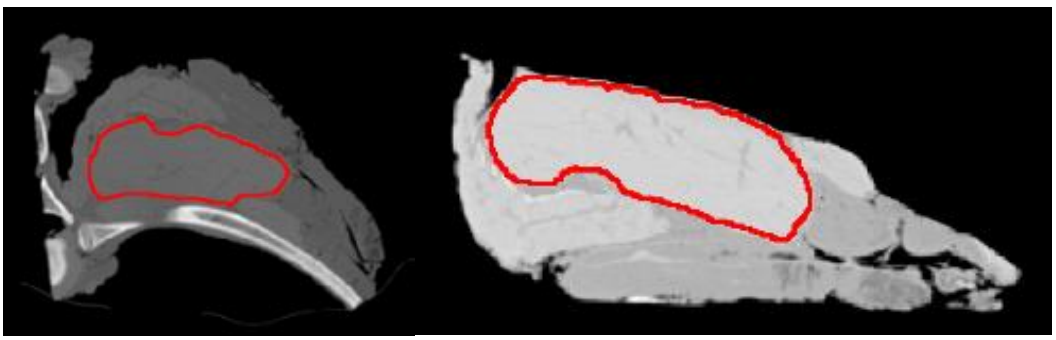

Figure 84 – Isolation of *longissimus dorsi* from CT images for a striploin bone-in (left) and boneless (right).

8.3 Results

Histogram data were obtained for each of the scans, focussing on the soft tissue range (-300HU to 300HU). This data was then normalised and plotted for each of the four carcase samples to visually compare the difference between the intensity distribution between the ribset and striploin for each sample as well as bone-in versus boneless for each. Figure 85, Figure 86, Figure 87, and Figure 88 show these histograms for the high-quality scan data obtained. The histograms for the corresponding high-speed scans can be seen in Figure 88. Statistics describing these data are summarised in

Table 11.

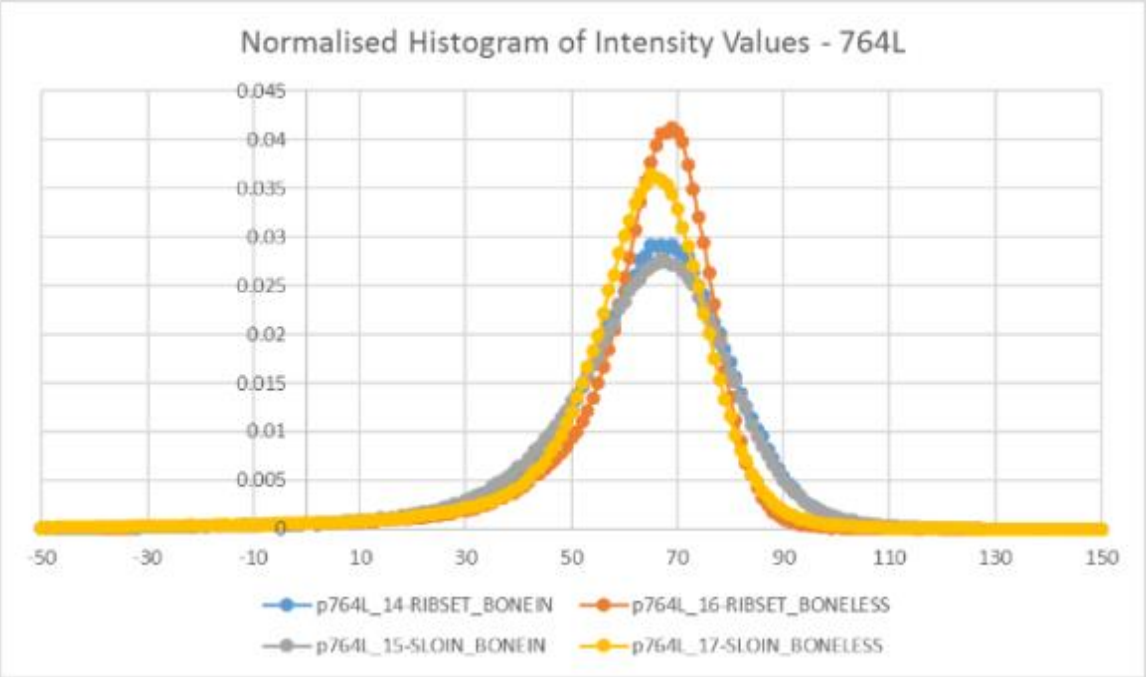

Figure 85 - Normalised Histogram of High-quality CT Scan Intensity Values of a bone-in and boneless ribset and striploin for sample 764L

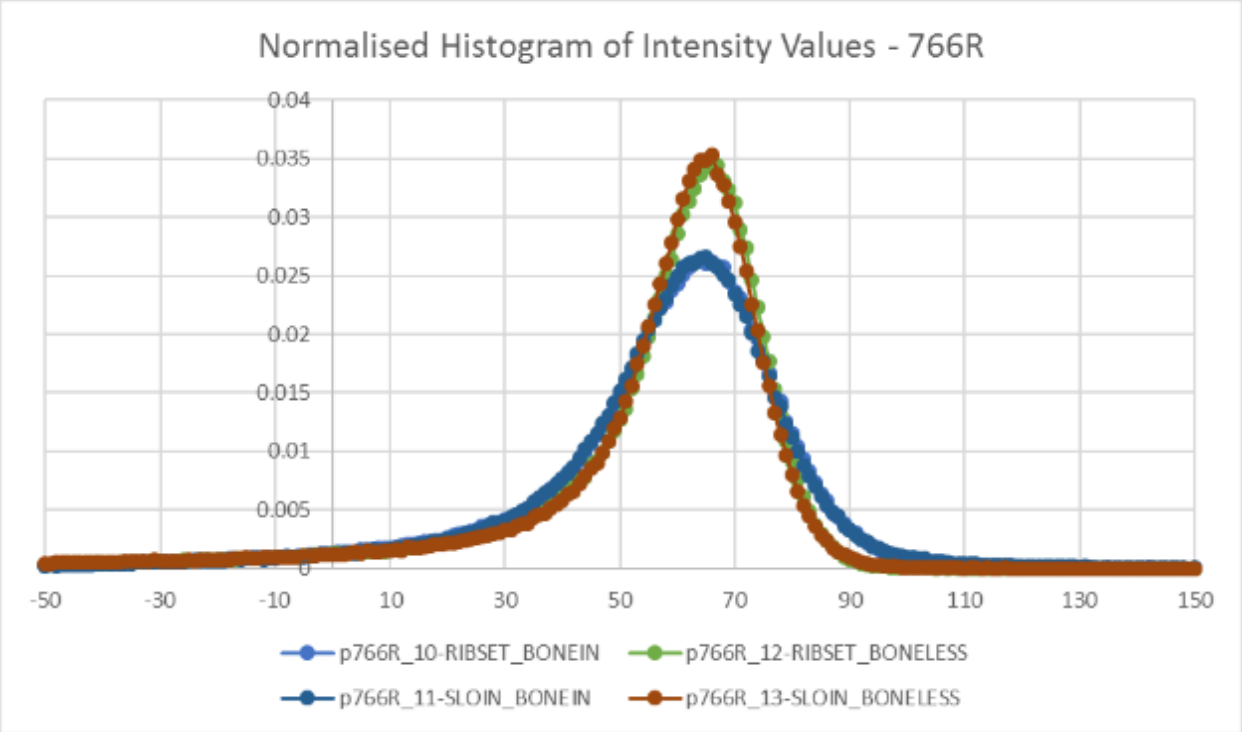

Figure 86 - Normalised Histogram of High-quality CT Scan Intensity Values of a bone-in and boneless ribset and striploin for sample 766R

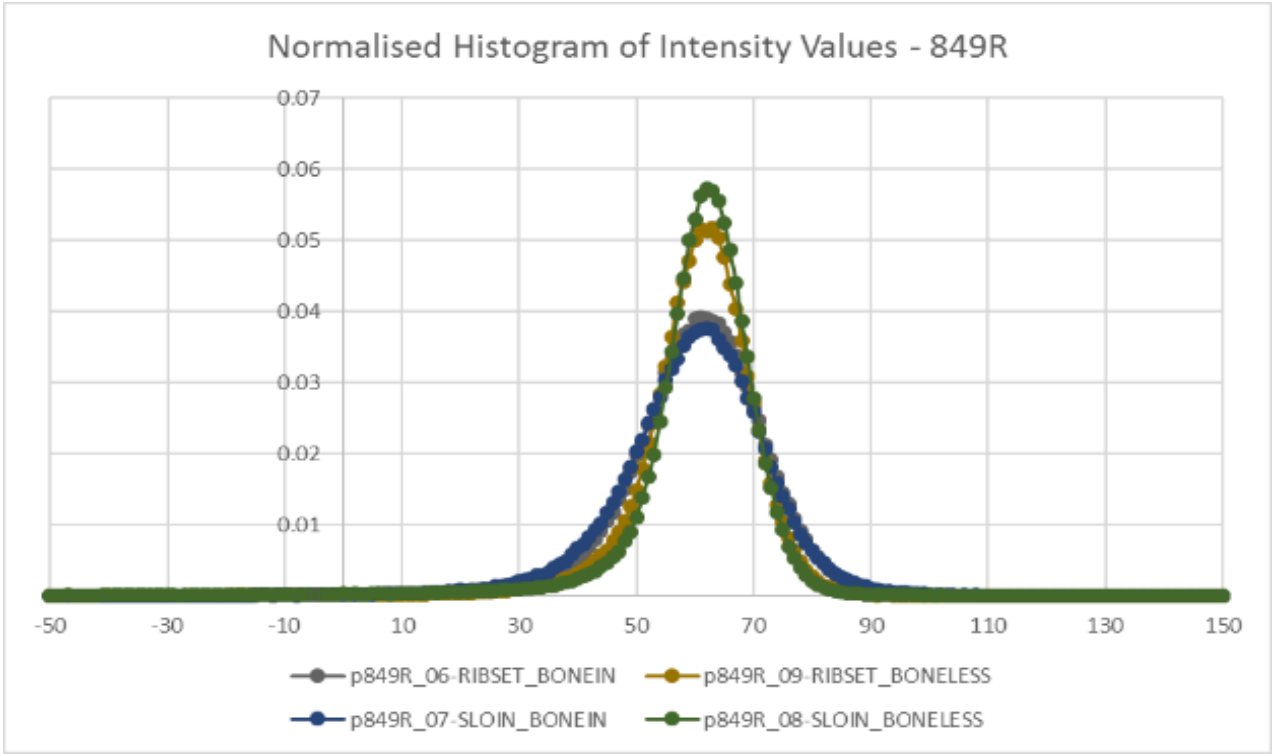

Figure 87 - Normalised Histogram of High-quality CT Scan Intensity Values of a bone-in and boneless ribset and striploin for sample 849R

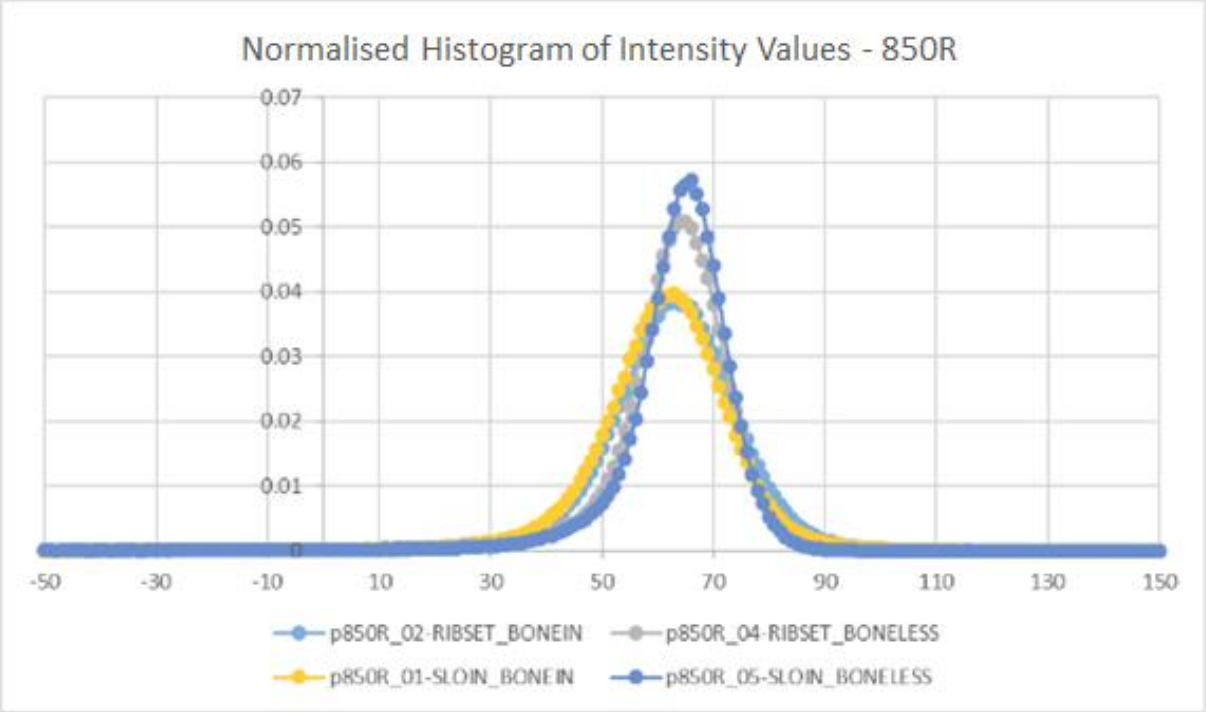

Figure 88 - Normalised Histogram of High-quality CT Scan Intensity Values of a bone-in and boneless ribset and striploin for sample 850R

Table 11 - Mean and standard deviation of intensity values for bone-in vs boneless samples and the difference between the two for each for the high-quality scans.

	Average	Standard Deviation	Difference Average	Difference Std. Dev.
p764L_14-RIBSET_BONEIN	63.5	18.44		
p764L_16-RIBSET_BONELESS	62.8	17.00	-0.7	-1.44
p764L_15-SLOIN_BONEIN	62.1	20.68		
p764L_17-SLOIN_BONELESS	60.6	21.02	-1.5	0.34
p766R_10-RIBSET_BONEIN	56.4	24.20		
p766R_12-RIBSET_BONELESS	56.3	22.70	-0.1	-1.50
p766R_11-SLOIN_BONEIN	56.9	24.47		
p766R_13-SLOIN_BONELESS	54.3	29.27	-2.6	4.79
p849R_06-RIBSET_BONEIN	60.2	12.31		
p849R_09-RIBSET_BONELESS	60.4	10.82	0.2	-1.49
p849R_07-SLOIN_BONEIN	59.7	12.91		
p849R_08-SLOIN_BONELESS	60.2	13.77	0.6	0.85
p850R_02-RIBSET_BONEIN	62.6	12.44		
p850R_04-RIBSET_BONELESS	62.7	10.87	0.1	-1.57
p850R_01-SLOIN_BONEIN	61.0	12.65		
p850R_05-SLOIN_BONELESS	63.5	11.54	0.8	0.68

8.4 Discussion

Observing the histogram data, it appears as though there is a flattening of the curves for all samples when comparing the bone-in data to boneless data. This is supported by the consistent lowering of the standard deviation for the ribset scans for each of the samples, albeit by a very small amount (approximately -1.5HU). Interestingly, this trend doesn't seem to be apparent for the striploin scans. In fact, a slight very increase in standard deviation is seen across all samples. The average HU of the scans hasn't changed significantly for either primal.

The one sample which seems to have exhibited a significant change between the bone-in and boneless scans is the striploin for 766R. The reason for this isn't immediately clear, especially given the equivalent ribset scan doesn't exhibit the same behaviour. Looking at the scans, it doesn't appear that there's any more streaking present than the other samples. It's possible that this stems from an artefact that may have been created from the manual selection of the eye muscle.

Ideally, the data would have been taken using a similar methodology to the striploin trials whereby portions of the striploins were denuded. These portions could then have been placed amongst a rib and the chine to simulate bone-in scanning. This would ensure that the data used is exactly the same for the bone-in and boneless scan data.

It therefore appears as though beam hardening has had minimal effect on the scan data for the eye muscle suggesting that IMF determination on bone-in primals is feasible. As these scans were performed on a commercial helical CT scanner with specialised software, it can be assumed that the beam hardening correction algorithms used by the system are quite advanced. These results serve as a target for IMF determination with an industrial CT scanner which is capable of running in full production. Beam hardening investigation trials should therefore be repeated when assessing such a machine. These can be included with the trials performed to create the IMF determination models.

8.5 Conclusion

The presence of beam hardening doesn't appear to significantly affect the intensity values of the CT images. Being a commercial helical system with specialised software, the beam hardening correction on this machine is likely to be quite complex. Considering this, beam hardening should be investigated again when trialling with an industrial-focussed CT scanner suitable for on-line applications.

9 Attenuation Artefact

9.1 Background

As aforementioned, a study has been performed within this project modelling intramuscular fat content within the eye muscle for beef striploins. For these trials, striploins were placed in a frame and scanned two at a time (Figure 89).

Figure 89 - Scanning arrangement for striploins

While analysing the CT slice images, it was noticed that there appeared to be a consistent attenuation of HU values towards the centre of the CT scanner's field of view. This meant the lower portions of the 'top' samples, and the upper portions of the 'bottom' samples seemed lower than would be expected. In Figure 90, the CT slice for two denuded striploin portions is shown on the left. Pixels with lower HU values were then identified and highlighted in red as shown on the right. Normally these pixels would be identified as fat. It can be seen however that significant regions are highlighted towards the centre of the CT's field of view. This is not due to fat coverage as the anterior and posterior portions of the striploin were denuded. The magnitude of this effect varied across samples.

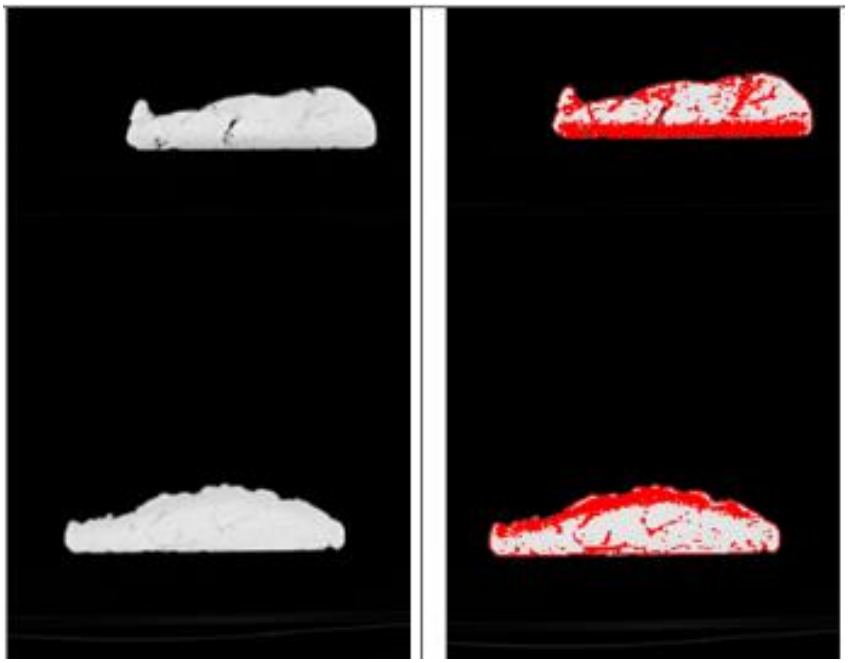

Figure 90 - CT scan image with two denuded striploins (left). HU values lower than a certain value were then highlighted (right). It can be seen that the bottom part of the top sample and the top part of the bottom sample are lower than would be expected.

Trials were therefore conducted in an attempt to quantify the effect of this artefact and how it may have influenced the intramuscular fat modelling.

9.2 Method

In the last round of intramuscular fat modelling trials, eight striploins were scanned. This time however each sample was scanned in both positions – 'top' and 'bottom'. Normalised histograms of these scans were built to compare and contrast between the different scan positions for both the high-quality and high-speed scans. The pixel neighbourhood processing and intramuscular fat algorithm was also applied for comparison.

9.3 Results

Normalised histograms of top and bottom scans for each sample with high-quality and high-speed scan settings are shown in Figure 91 to Figure 98.

Table 12 summarises the mean and standard deviation of the intensity values for each scan.

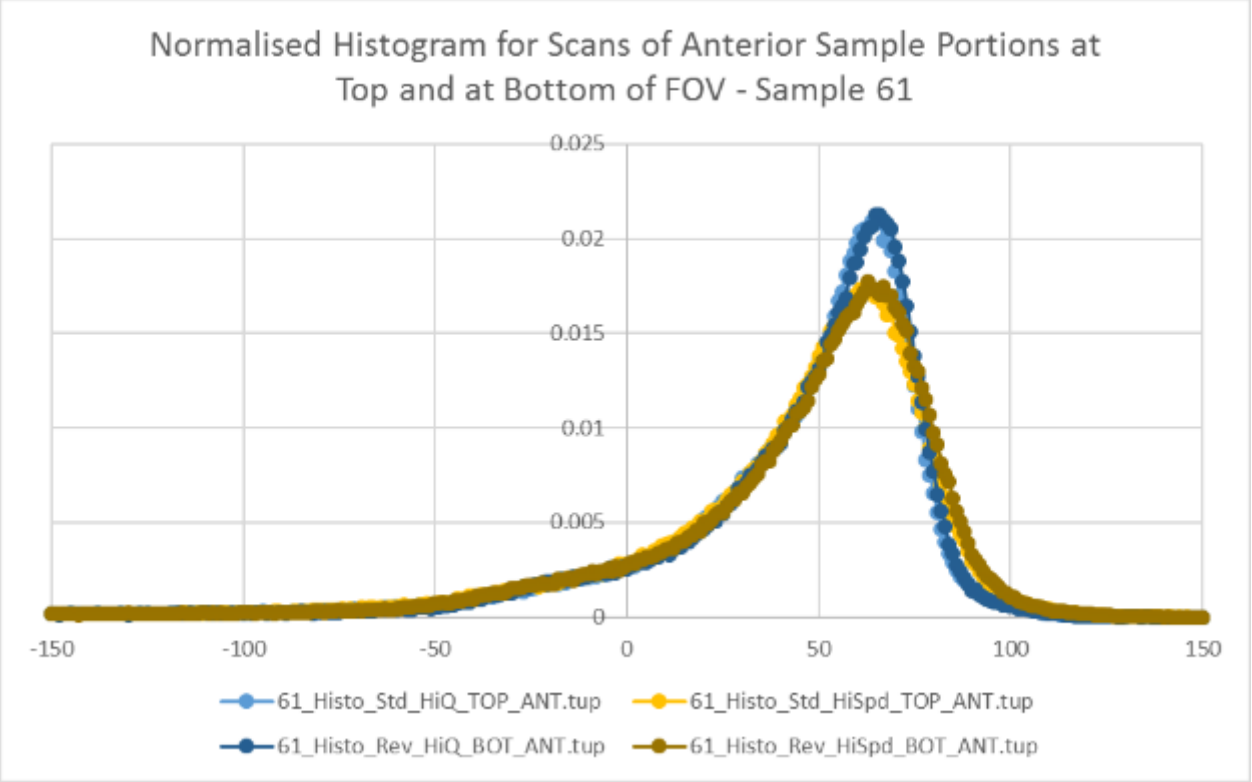

Figure 91 - Normalised Histogram of High-quality and High-speed CT Scan Intensity Values of the anterior portion of sample 61 at two different heights in the CT's field of view.

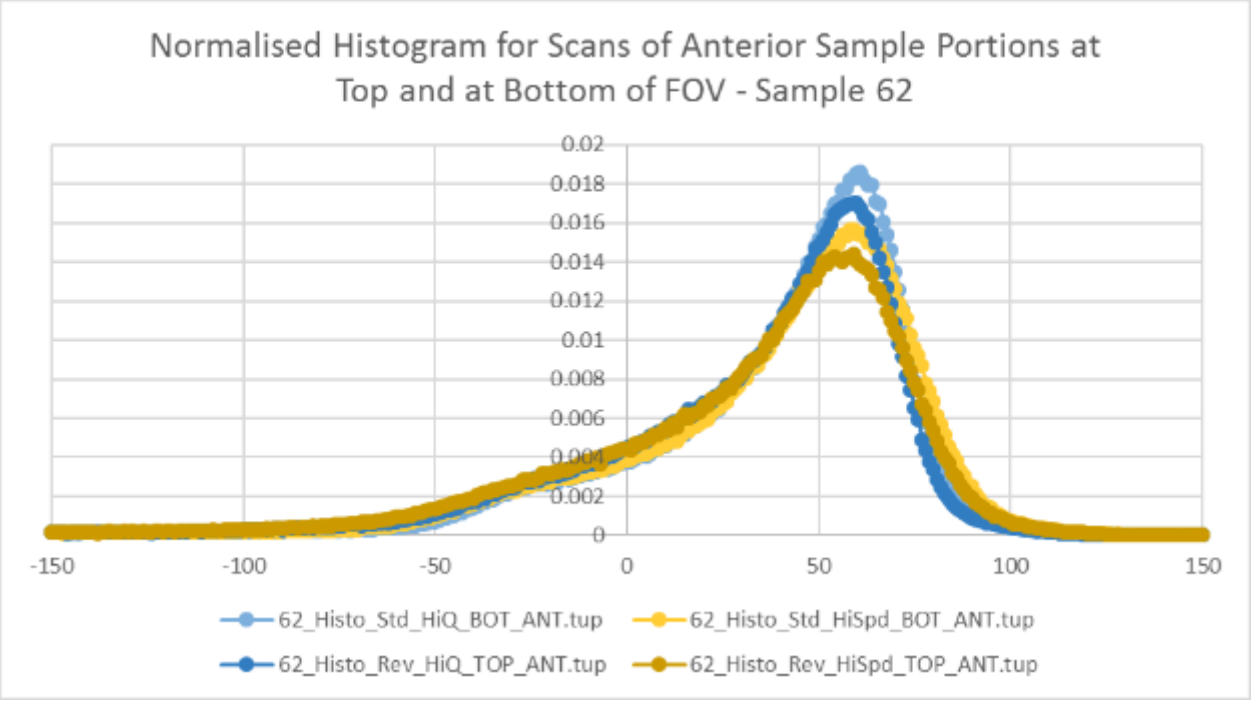

Figure 92 - Normalised Histogram of High-quality and High-speed CT Scan Intensity Values of the anterior portion of sample 62 at two different heights in the CT's field of view.

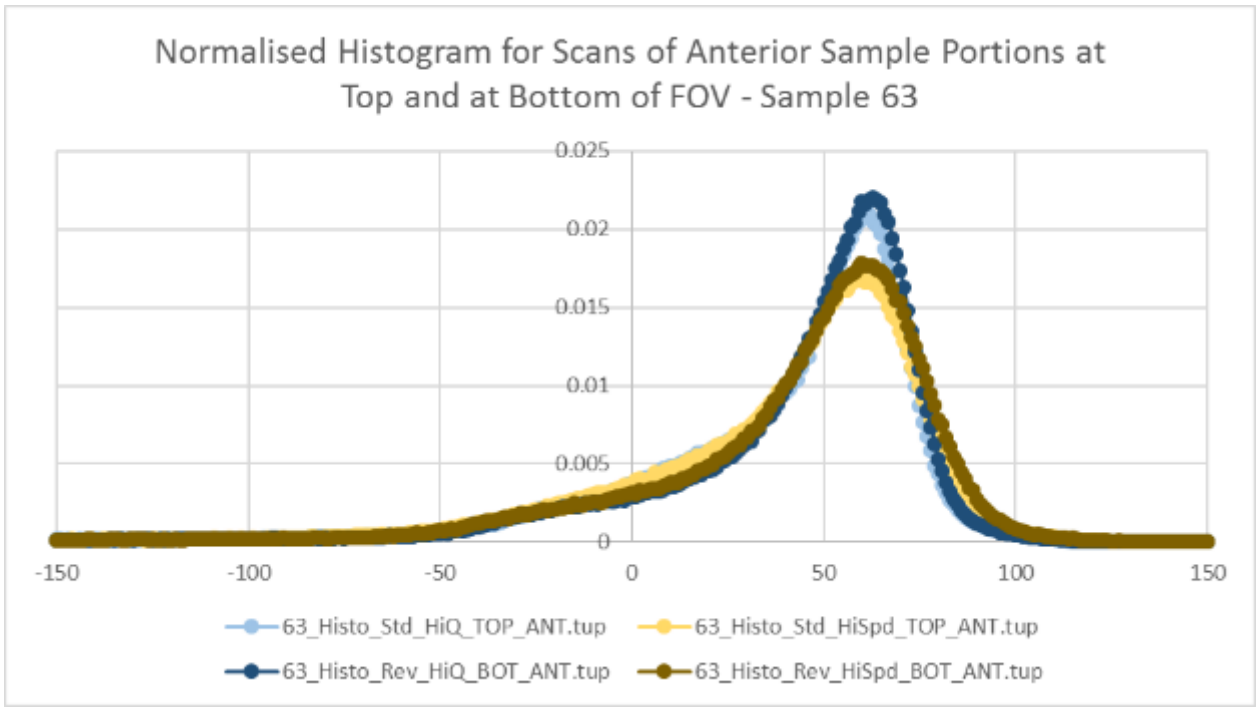

Figure 93 - Normalised Histogram of High-quality and High-speed CT Scan Intensity Values of the anterior portion of sample 63 at two different heights in the CT's field of view.

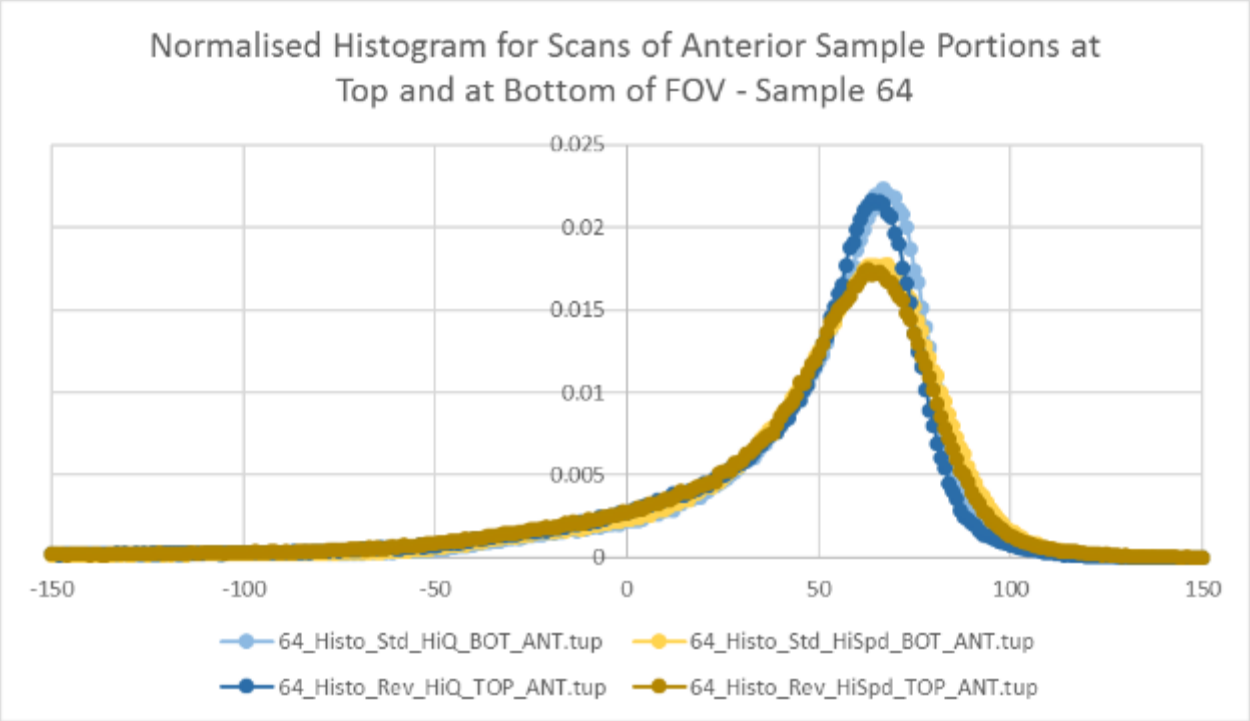

Figure 94 - Normalised Histogram of High-quality and High-speed CT Scan Intensity Values of the anterior portion of sample 64 at two different heights in the CT's field of view.

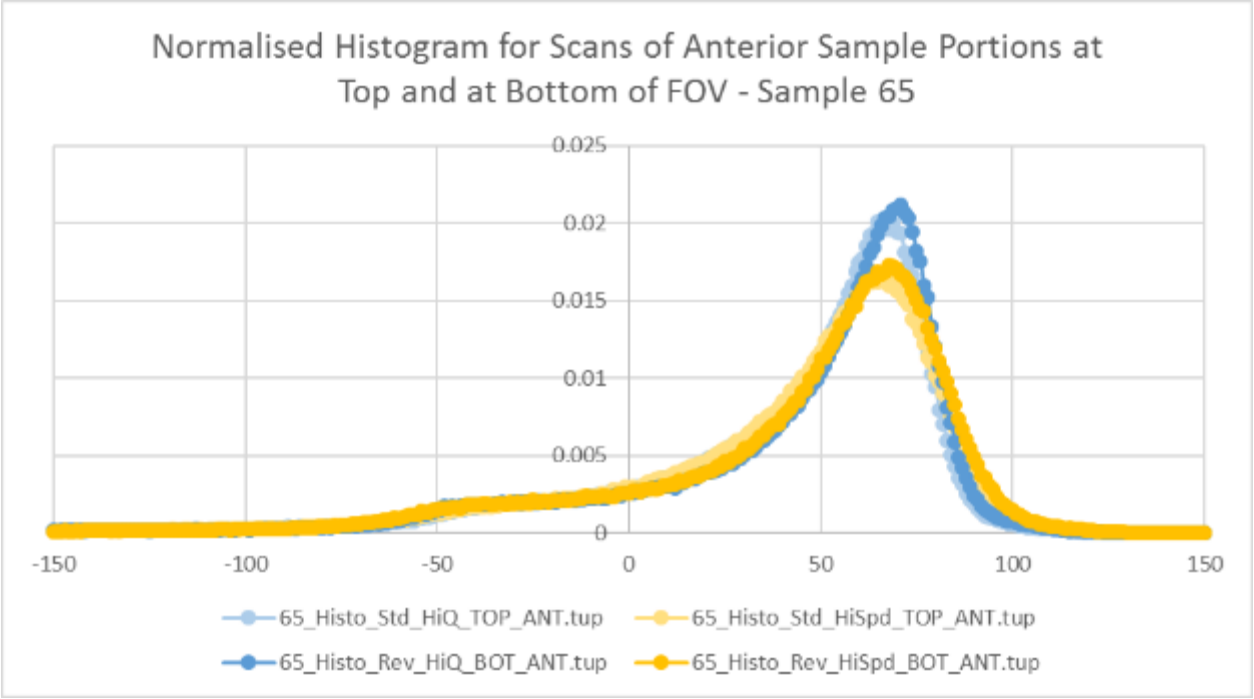

Figure 95 - Normalised Histogram of High-quality and High-speed CT Scan Intensity Values of the anterior portion of sample 65 at two different heights in the CT's field of view.

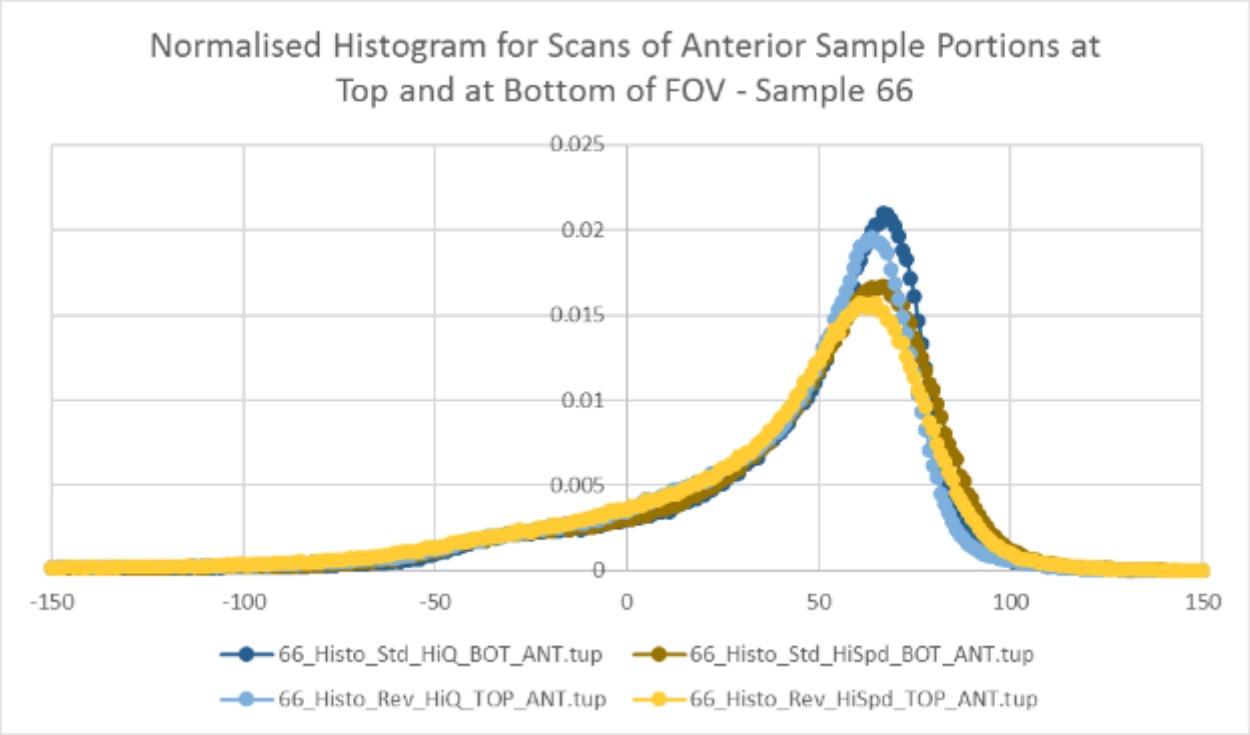

Figure 96 - Normalised Histogram of High-quality and High-speed CT Scan Intensity Values of the anterior portion of sample 66 at two different heights in the CT's field of view.

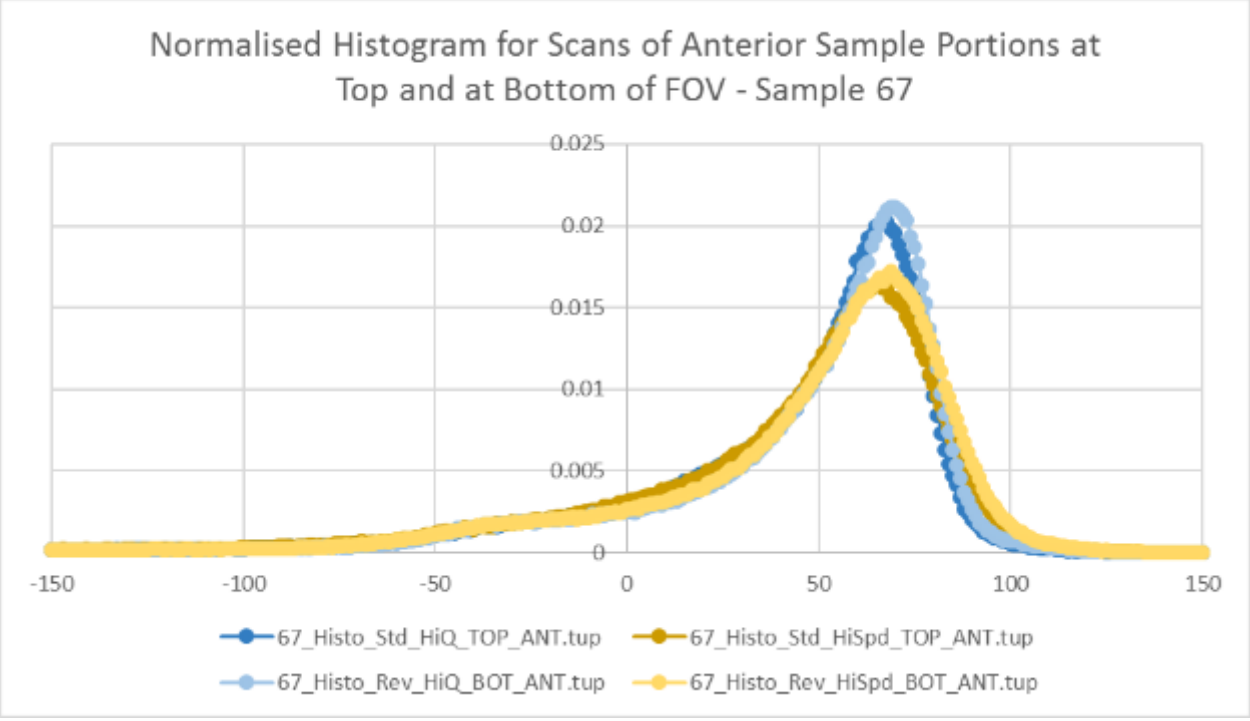

Figure 97 - Normalised Histogram of High-quality and High-speed CT Scan Intensity Values of the anterior portion of sample 67 at two different heights in the CT's field of view.

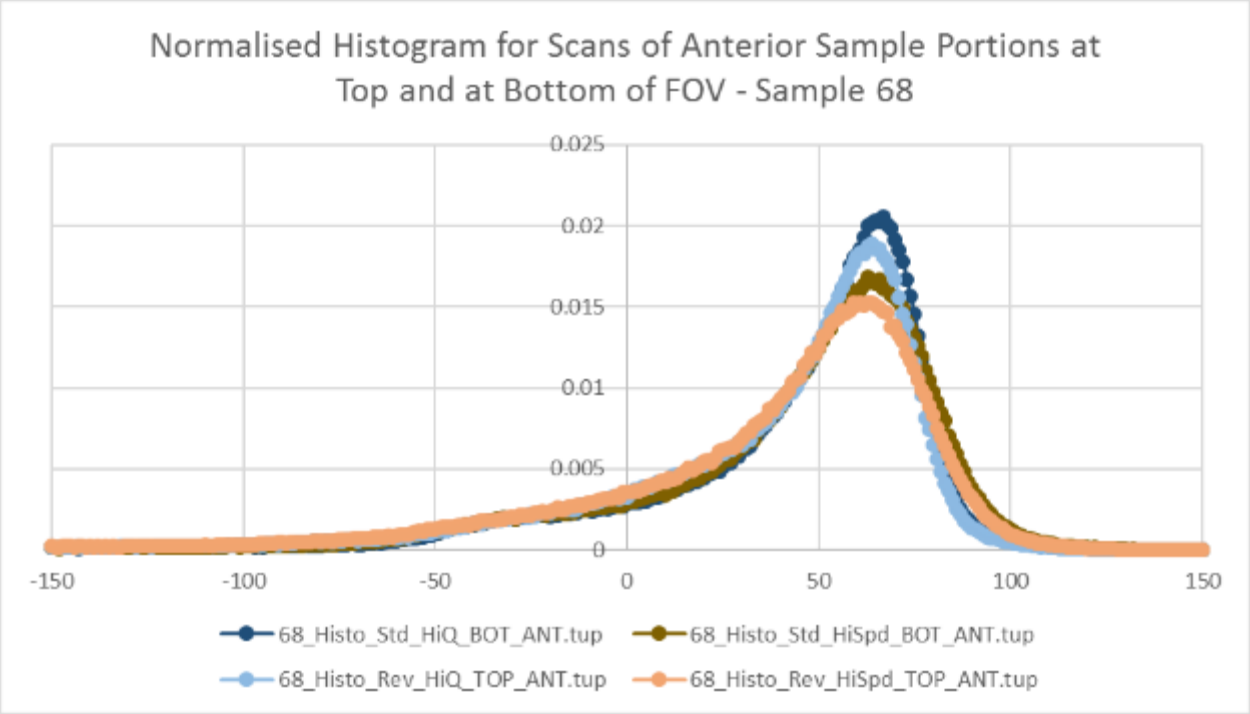

Figure 98 - Normalised Histogram of High-quality and High-speed CT Scan Intensity Values of the anterior portion of sample 68 at two different heights in the CT's field of view.

Table 12 - Mean and standard deviation of intensity values for the anterior portion of eight striploin samples at two different heights within the CT's field of view, and the difference between these values.

Sample	Scan Setting	Scan Position	Portion	Average	StdDev	Difference Ave	Difference StdDev
61	HiQ	BOT	ANT	38.8	52.35		
61	HiQ	TOP	ANT	36.8	54.25	2.0	-1.90
62	HiQ	BOT	ANT	34.0	47.56		
62	HiQ	TOP	ANT	29.1	49.53	5.0	-1.97
63	HiQ	BOT	ANT	38.6	48.31		
63	HiQ	TOP	ANT	34.9	50.07	3.8	-1.76
64	HiQ	BOT	ANT	43.0	52.47		
64	HiQ	TOP	ANT	37.9	54.91	5.1	-2.44
65	HiQ	BOT	ANT	38.2	55.66		
65	HiQ	TOP	ANT	37.0	53.05	1.2	2.61
66	HiQ	BOT	ANT	39.1	49.63		
66	HiQ	TOP	ANT	33.5	52.39	5.6	-2.76
67	HiQ	BOT	ANT	40.9	52.39		
67	HiQ	TOP	ANT	37.2	53.91	3.7	-1.52
68	HiQ	BOT	ANT	38.2	50.50		
68	HiQ	TOP	ANT	32.9	53.94	5.3	-3.44

Data for the high-quality scans of the anterior portions of the striploins were then reprocessed using pixel neighbourhood information. The average and standard deviation of the intensities for

these reprocessed images was then calculated for scans in both 'top' and 'bottom' orientations. The difference in intramuscular fat content as per the derived model between the two cases was also calculated. This data is summarised in Table 13.

Table 13 - Mean and standard deviation of intensity values for the anterior portion of eight striploin samples at two different heights within the CT's field of view, and the difference between these values after pixel neighbourhood masking has been applied. The difference in IMF% is also calculated.

	Scan	Scan				Difference		IMF%
Sample	Setting	Position	Portion	Average	StdDev	Ave	StdDev	diff
61	HiQ	BOT	ANT	48.0	23.43			
61	HiQ	TOP	ANT	46.6	24.95	1.4	-1.53	0.66
62	HiQ	BOT	ANT	39.7	25.36			
62	HiQ	TOP	ANT	35.3	28.61	4.4	-3.25	0.67
63	HiQ	BOT	ANT	45.5	23.48			
63	HiQ	TOP	ANT	42.5	25.50	3.0	-2.02	0.25
64	HiQ	BOT	ANT	52.0	23.73			
64	HiQ	TOP	ANT	47.5	27.60	4.6	-3.87	1.14
65	HiQ	BOT	ANT	46.5	31.07			
65	HiQ	TOP	ANT	45.0	29.56	1.5	1.51	-2.22
66	HiQ	BOT	ANT	45.3	28.13			
66	HiQ	TOP	ANT	40.5	30.93	4.8	-2.79	-0.02
67	HiQ	BOT	ANT	48.5	28.10			
67	HiQ	TOP	ANT	45.4	29.92	3.1	-1.82	0.01
68	HiQ	BOT	ANT	45.1	27.33			
68	HiQ	TOP	ANT	40.8	30.73	4.2	-3.40	0.87

9.4 Discussion

Observing the histograms, it appears as though the curves seem fairly consistent between the 'top' and 'bottom' scans for both the high-quality and high-speed scans. An exceptions to this is sample 68. The difference in average HU value between the 'top' and 'bottom' scans appears to show a trend towards a slight increase, by up to 5.3HU. The standard deviation seems to generally drop slightly.

When the pixel masking is applied and the new averages and standard deviations are calculated, a similar trend exists. When the difference in IMF is calculated between the 'top' scan and the 'bottom' scan, it can be seen that the difference is small and well within one RMSE for the model. It does appear as though the bottom scan does consistently result in slightly higher IMF though. The exception to this is sample 65, which exhibits a much higher error.

While the existence of this artefact is not ideal, it doesn't appear to have compromised the data taken during the striploin trials too drastically. Thus it is not recommended to perform any further trialling with this CT scanner. The next set of trials in this area will likely be performed with a CT scanner which is capable of operating on-line in an abattoir. It will therefore be important when assessing this scanner to first demonstrate homogeneity throughout the scanner's imaging field-of-view. This may require a specialised phantom to verify this and/or correct for any imperfections.

9.5 Conclusion

It doesn't appear as if the HU attenuation artefact identified has affected the data too heavily. However, it does still present an opportunity area for improving the IMF model's performance.

Considering the next step is to investigate CT-technology which is capable of running on-line in an abattoir, no further work needs to be done in examining the effect of this artefact on the beef striploin intramuscular fat modelling trials. However, when a suitable industrial CT machine is tested, homogeneity throughout the CT scanner's entire imaging field-of-view should be assessed with the use of a phantom or similar.

10 Ossification

10.1 Background

It is known that maturity correlates with eating quality (Bonny, et al., 2016). Currently this is graded manually by an operator who assesses each carcase individually to assign an ossification score. A grading card for this process is shown in Figure 99. Recent work has indicated that ossification score is actually a better indicator for eating quality than age (Bonny et al, 2016). This is presumably because ossification better reflects physiological age (i.e. maturity) as opposed to chronological age, the former of which is heavily influenced by nutritional factors and is more influential on eating quality.

While a better measure than age, ossification is still a subjective score delivered by a human operator. Finding an objective means of measuring maturity is therefore desirable to industry. Such measures may be possible using x-ray imaging, including CT.

Currently, bone mineral content (BMC) and bone mineral density (BMD) are measured in humans using DEXA imaging, mainly for the purposes of diagnosing and monitoring health issues relating to bone, such as osteoporosis. Such data also correlates with a person's age (van der Sluis, de Ridder, Boot, Krenning, & de Muinck Keizer-Schrama, 2002). No research appears to be done however specifically investigating how carcase maturity can be measured using CT technology. There is also no published work specifically investigating how BMC or BMD directly correlate with maturity in beef or sheep although (Cake, Boyce, Gardner, Hopkins, & Pethick, 2007) suggest that bone mineral profile, particularly magnesium content, may serve as an indicator for maturity. (Tomkins, Harper, Bruce, & Hunter, 2006) found a significant effect by growth path on bone mineral content in steers, with rapid growing steers having greater bone mineral content ($P<0.05$) than those on a weight loss feeding arrangement. This suggests a positive correlation between BMC and maturity. Work is currently being performed assessing the relationship between DEXA values for bone and maturity in sheep (Anderson, Williams, Boyce, Cook, & Gardner, 2017).

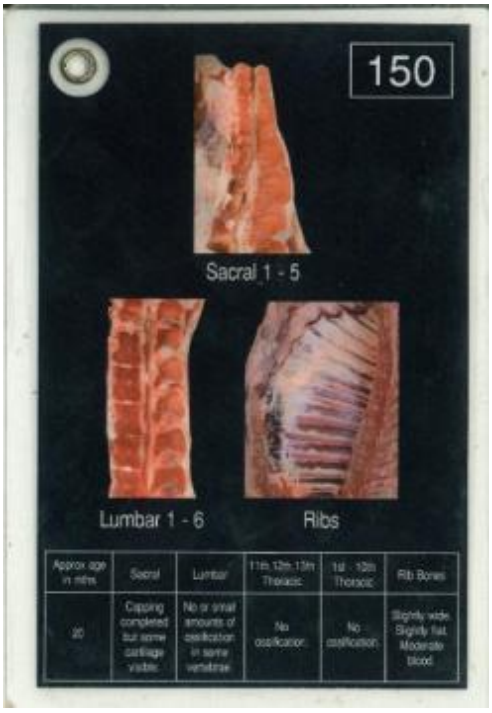

Figure 99 - MSA ossification grading card (reference: Meat Standards Australia, 2004)

A lot of research has also been performed around using CT data to calculate BMD and BMC rather than DEXA imaging (Cann, 1988; Lang, Harris, & Genant, 1999; Link, Koppers, Bauer, Lu, & Rummeny, 2004; Schreiber, Anderson, & Hsu, 2014). Such a technique is referred to as quantitative CT (QCT) and is widely available.

This report outlines a high-level investigation into the use of CT data for determining ossification score.

10.2 Methods

A previous trial performed on another project involved breaking down whole beef sides into a number of smaller primals which were then CT scanned. The MSA grading data for these sides was also recorded, including ossification score. Scans were conducted with the following settings: exposure 150mAs, Voltage 100kV,Current 180 mA, pitch 0.6, slice width 5mm.

The CT data of 12 carcases was collected whose ossification scores ranged from 160 to 590. The scans of the bone-in primals were selected in particular – Ribset, Rib Plate, Chuck, Chuck Ribs, Rump and Loin. Histograms were built from these CT images in order to try and identify any obvious relationships.

10.3 Results

Histograms were first built for each of the primals. Data was limited to HU>175 in an attempt to isolate cartilage and bone. Six primals are displayed in Figure 100 to Figure 105 for the purpose

of clarity – two ‘low oss’, two ‘mid oss’, and two ‘high oss’. Histograms were also built for each of the samples (Figure 106 to Figure 111). The mean and standard deviation of the intensity values for the scans was then calculated (

Table 14).

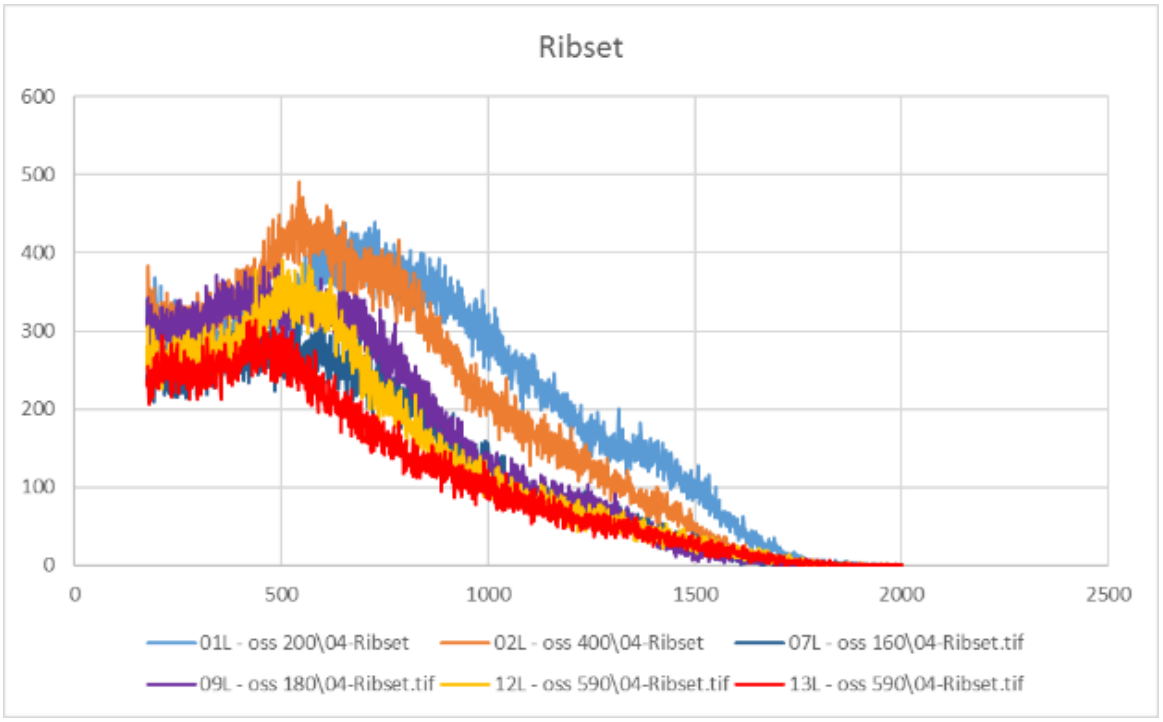

Figure 100 - Histogram for the Ribset in a number of carcases with varying ossification scores

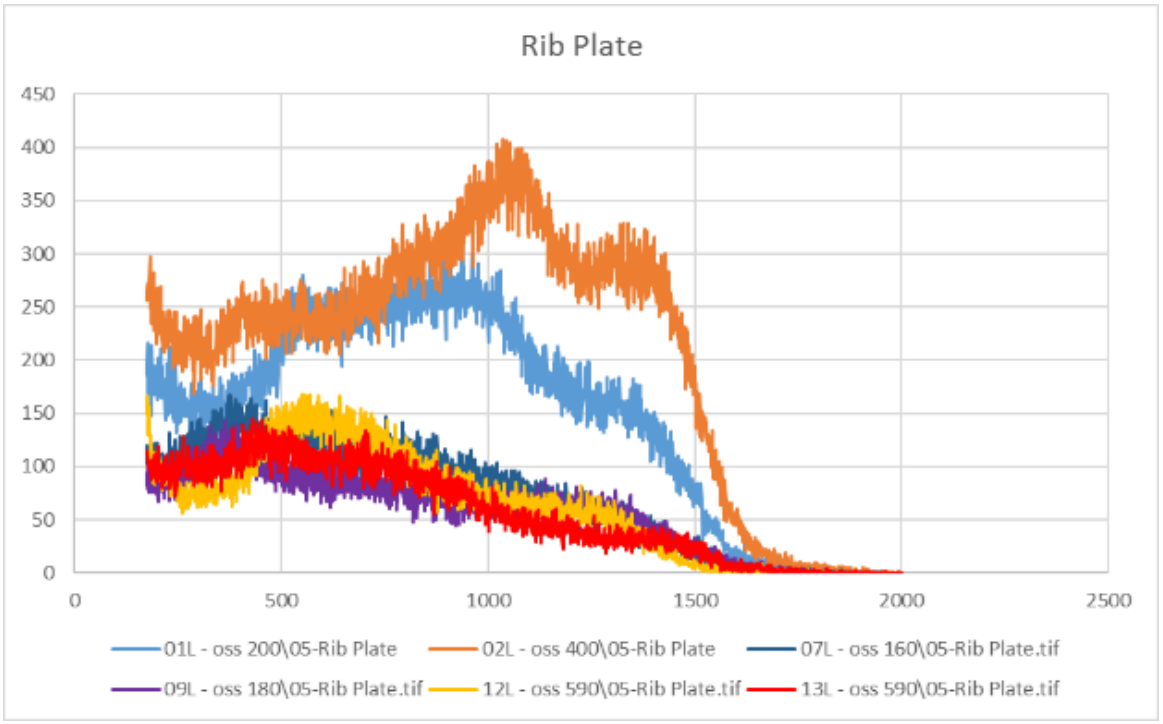

Figure 101 - Histogram for the Rib Plate in a number of carcases with varying ossification scores

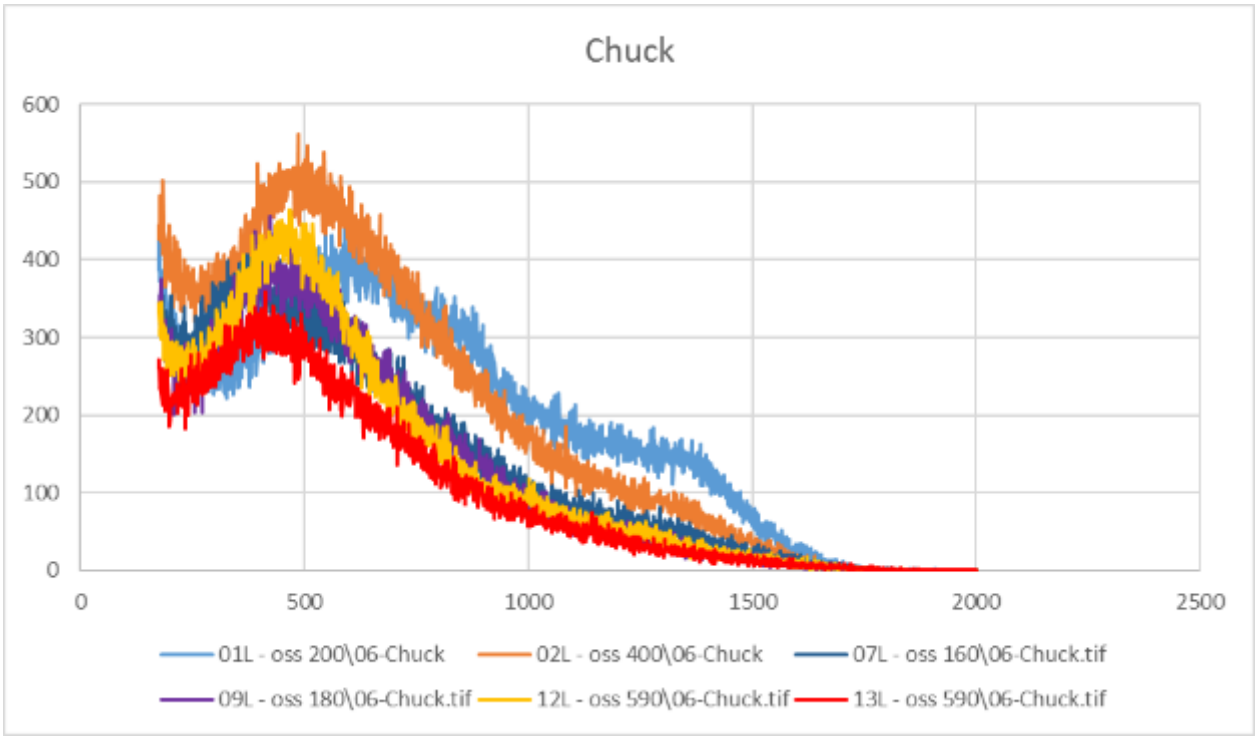

Figure 102 - Histogram for the Chuck in a number of carcases with varying ossification scores

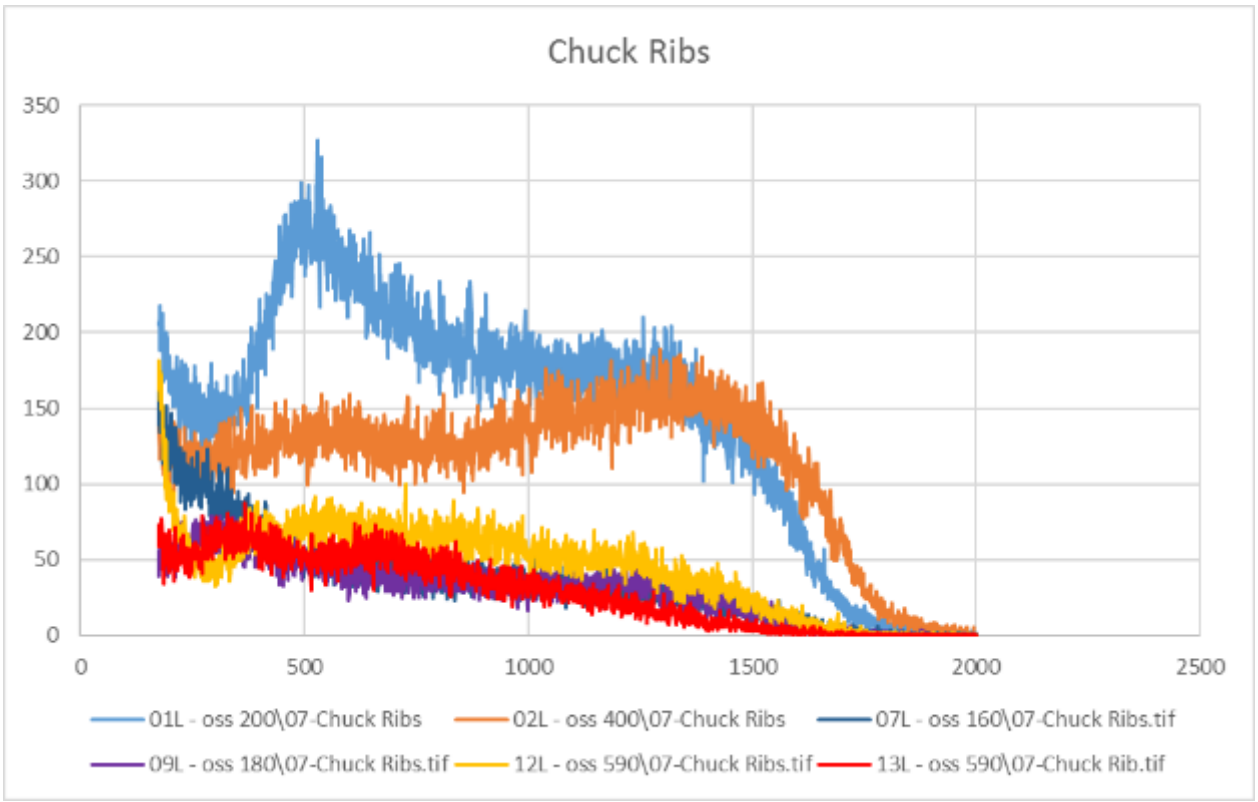

Figure 103 - Histogram for the Chuck Ribs in a number of carcases with varying ossification scores

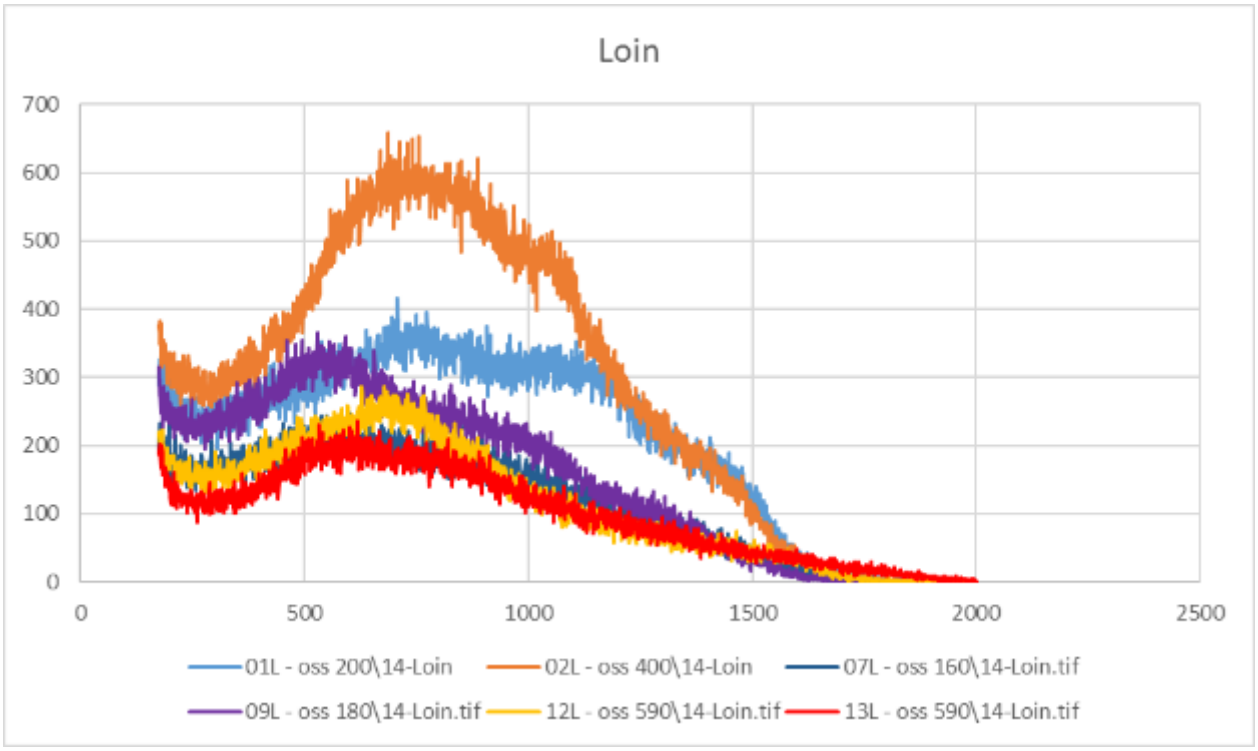

Figure 104 - Histogram for the Loin in a number of carcases with varying ossification scores

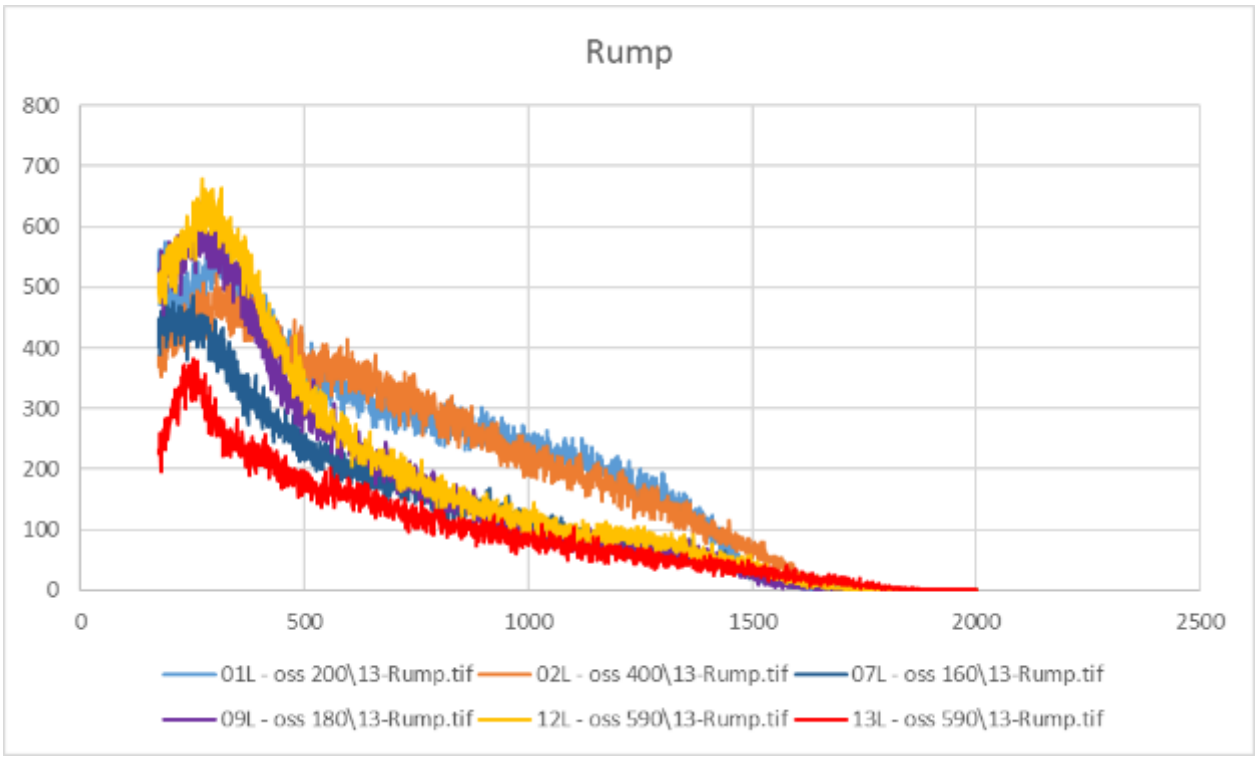

Figure 105 - Histogram for the Rump in a number of carcases with varying ossification scores

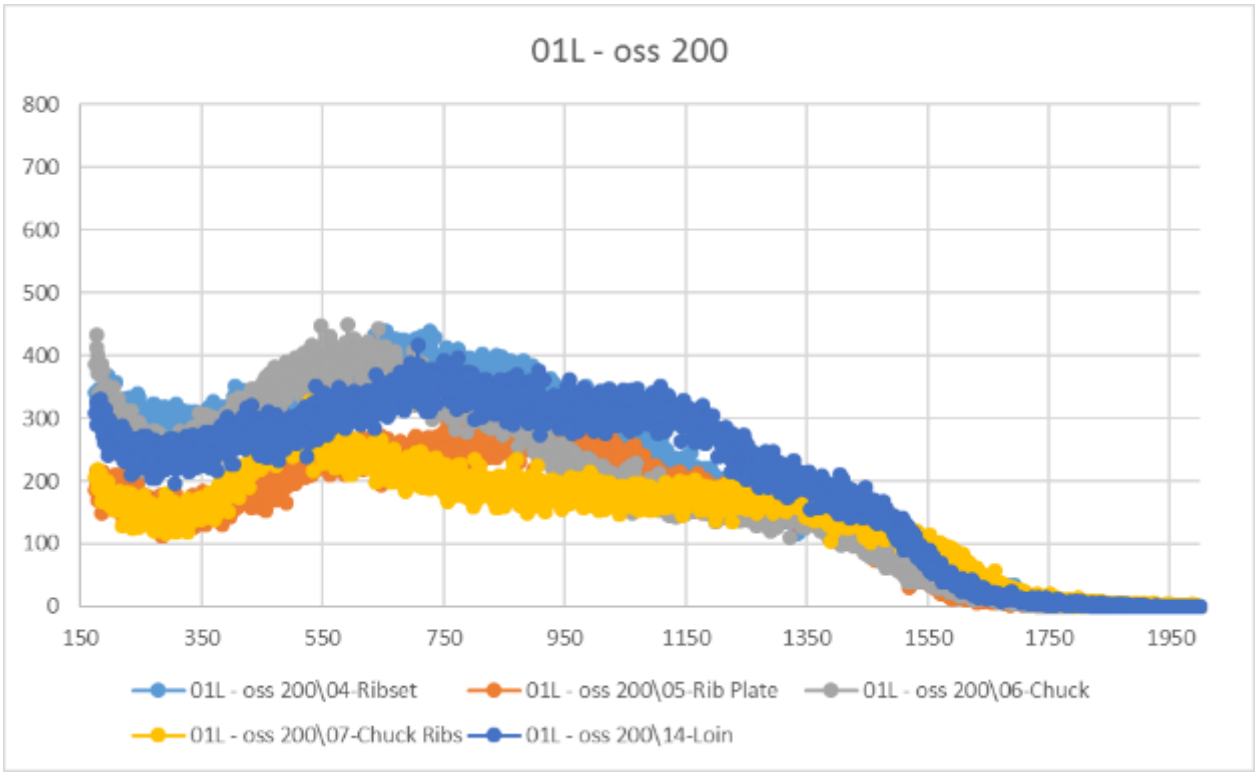

Figure 106 - Histogram for a number of bone-in primals for sample 01L, ossification score 200

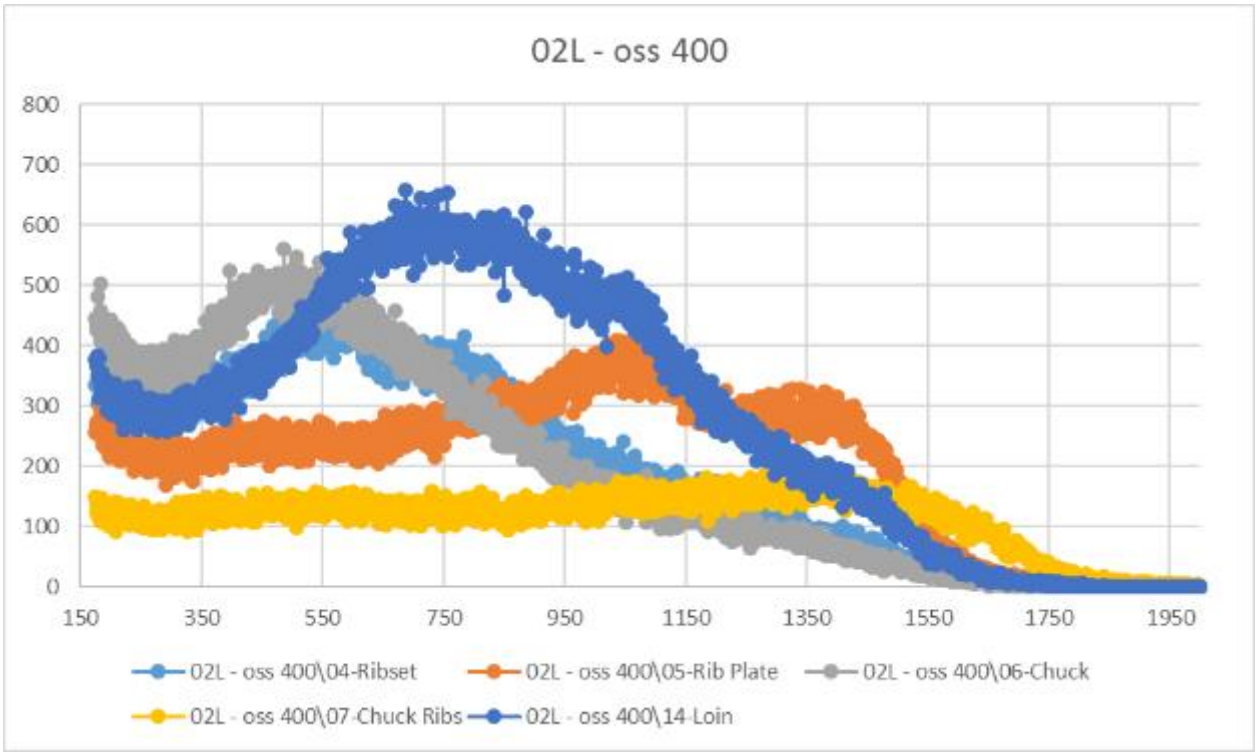

Figure 107 - Histogram for a number of bone-in primals for sample 02L, ossification score 400

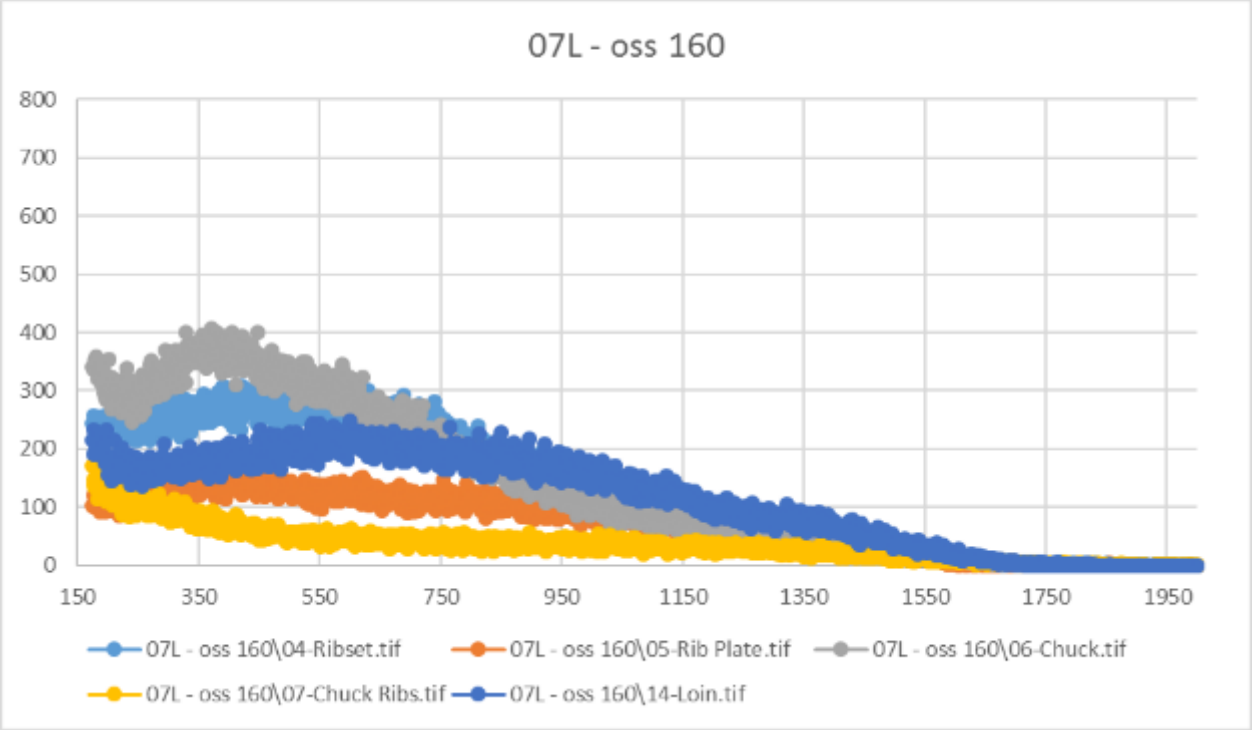

Figure 108 - Histogram for a number of bone-in primals for sample 07L, ossification score 160

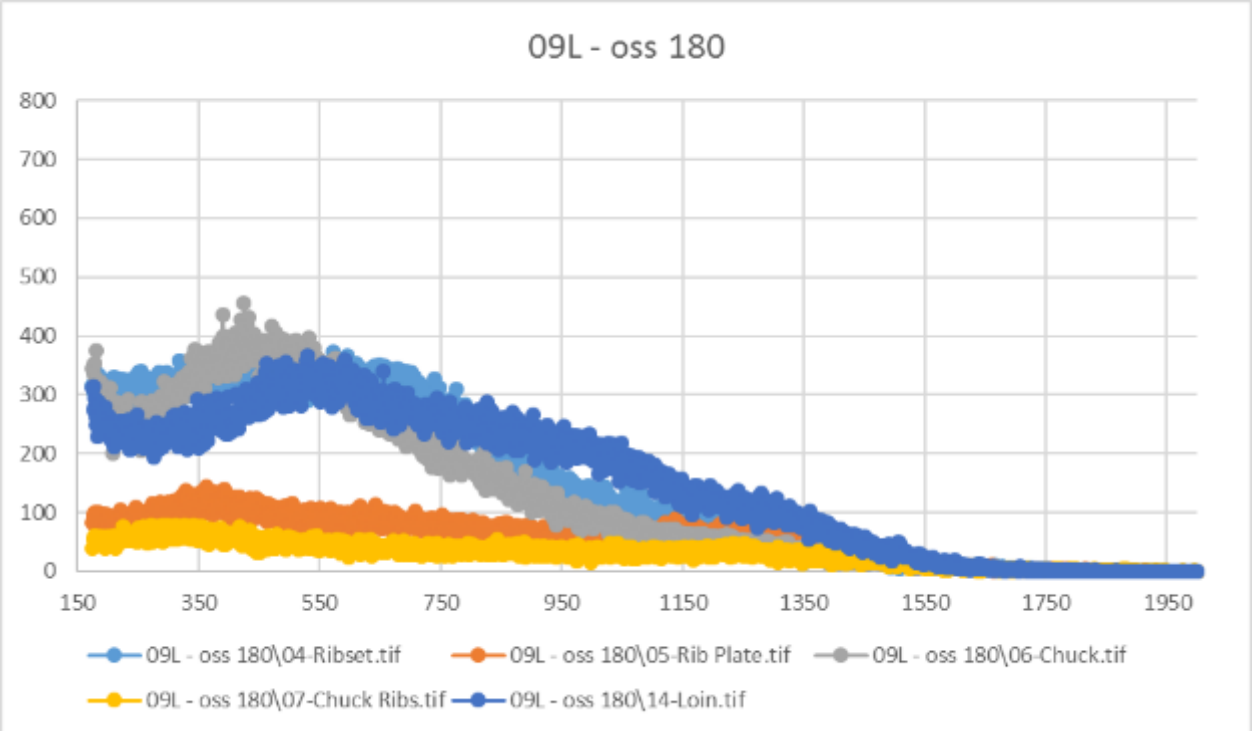

Figure 109 - Histogram for a number of bone-in primals for sample 09L, ossification score 180

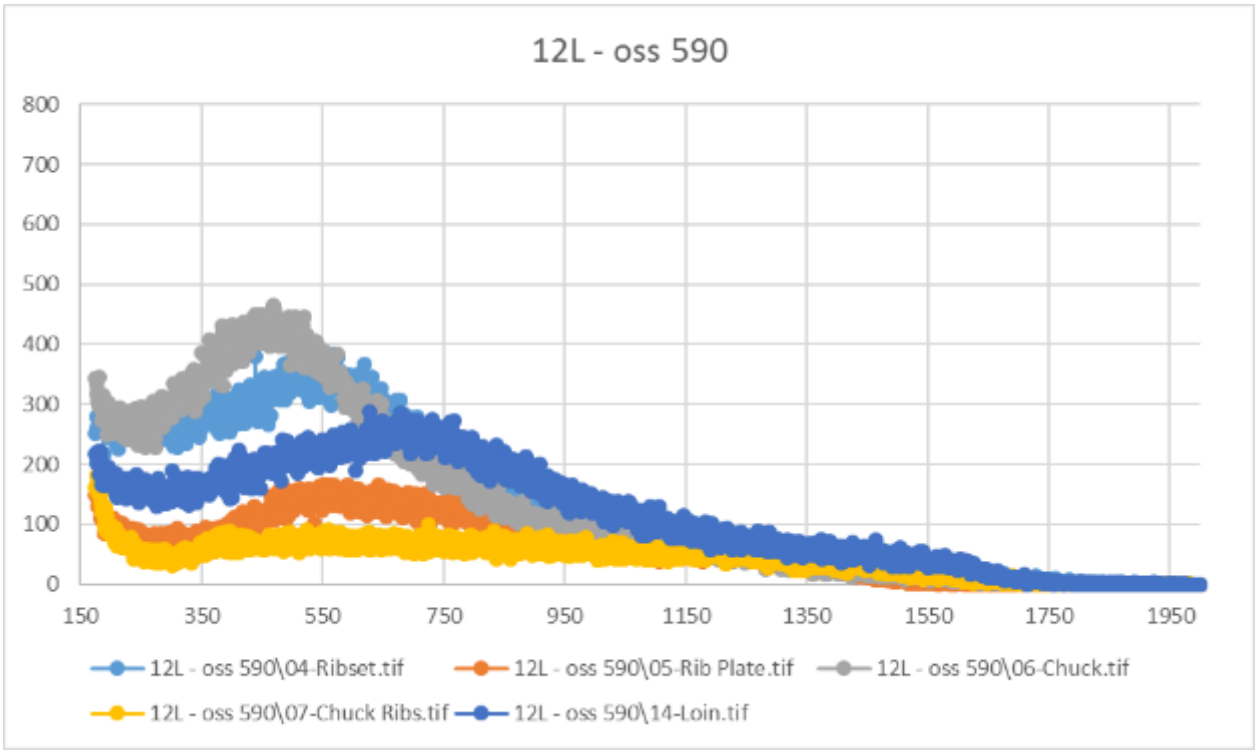

Figure 110 - Histogram for a number of bone-in primals for sample 12L, ossification score 590

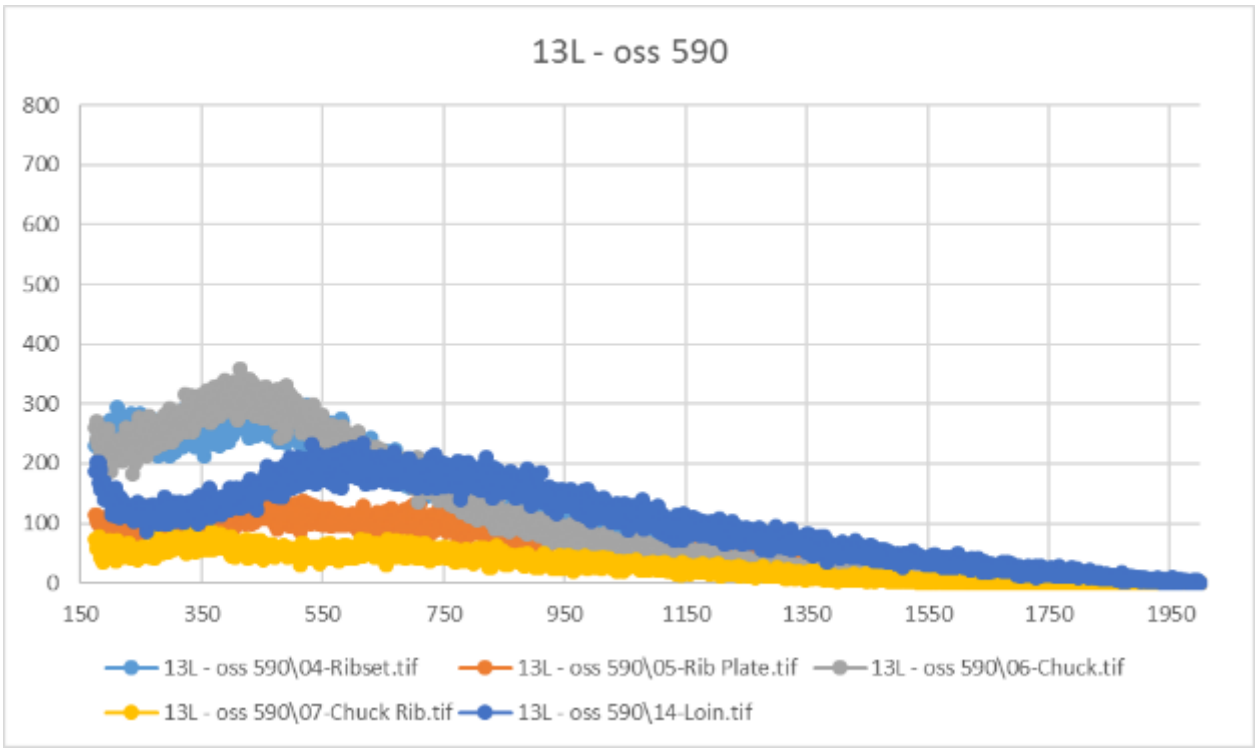

Figure 111 - Histogram for a number of bone-in primals for sample 13L, ossification score 590

Table 14 - Mean and Standard Deviation of HU values for each carcase for each of the different primals

Carc ID	OSS Score	Cut	Mean HU	Standard Deviation
07L	160	Ribset	663.2	327.65
08L	180	Ribset	623.0	309.98
09L	180	Ribset	637.7	312.00
06L	190	Ribset	614.8	311.87
01L	200	Ribset	777.6	363.74
05L	200	Ribset	679.8	343.35
04L	250	Ribset	736.5	388.58
02L	400	Ribset	702.9	334.21
03L	400	Ribset	671.3	337.82
12L	590	Ribset	643.7	326.68
13L	590	Ribset	643.1	341.53
14L	590	Ribset	657.0	340.09
07L	160	Rib Plate	726.3	349.97
08L	180	Rib Plate	751.1	364.73
09L	180	Rib Plate	753.2	379.19
06L	190	Rib Plate	690.8	352.31
01L	200	Rib Plate	828.6	355.46
05L	200	Rib Plate	776.2	348.24
04L	250	Rib Plate	849.3	394.91
02L	400	Rib Plate	896.0	383.27
03L	400	Rib Plate	769.2	363.55
12L	590	Rib Plate	724.1	326.35
13L	590	Rib Plate	707.5	351.26
14L	590	Rib Plate	1056.4	541.64
07L	160	Chuck	615.7	319.19
08L	180	Chuck	582.2	298.43
09L	180	Chuck	594.4	292.04
06L	190	Chuck	609.9	312.23
01L	200	Chuck	743.8	353.41
05L	200	Chuck	642.8	312.92
04L	250	Chuck	697.7	352.67
02L	400	Chuck	643.6	316.34
03L	400	Chuck	639.8	318.72
12L	590	Chuck	588.2	294.69
13L	590	Chuck	586.9	298.87
14L	590	Chuck	639.0	404.49

Carc ID	OSS Score	Cut	Mean HU	Standard Deviation
07L	160	Chuck Ribs	687.3	408.33
08L	180	Chuck Ribs	704.8	361.31
09L	180	Chuck Ribs	751.9	398.78
06L	190	Chuck Ribs	700.5	376.44
01L	200	Chuck Ribs	855.3	398.68
05L	200	Chuck Ribs	677.5	350.97
04L	250	Chuck Ribs	878.9	419.71
02L	400	Chuck Ribs	964.5	437.97
03L	400	Chuck Ribs	828.1	406.78
12L	590	Chuck Ribs	786.9	382.48
13L	590	Chuck Ribs	677.2	336.62
14L	590	Chuck Ribs	825.3	490.77
07L	160	Loin	749.0	354.28
08L	180	Loin	648.4	307.66
09L	180	Loin	713.4	333.00
06L	190	Loin	658.4	329.78
01L	200	Loin	828.7	368.24
05L	200	Loin	736.2	330.06
04L	250	Loin	832.0	397.72
02L	400	Loin	802.2	333.18
03L	400	Loin	760.7	352.06
12L	590	Loin	740.6	348.96
13L	590	Loin	792.8	382.86
14L	590	Loin	742.7	368.69
07L	160	Rump	604.3	350.04
08L	180	Rump	573.5	344.25
09L	180	Rump	559.2	329.04
06L	190	Rump	569.3	352.52
01L	200	Rump	673.2	355.93
05L	200	Rump	614.6	351.82
04L	250	Rump	678.3	427.81
02L	400	Rump	689.6	360.20
03L	400	Rump	673.6	363.93
12L	590	Rump	574.2	342.44
13L	590	Rump	640.9	380.31
14L	590	Rump	595.1	391.98

10.4 Discussion

None of the primals demonstrate an obvious trend for ossification score across the different carcase samples. There is also a lack of an obvious relationship when observing the data when grouped into carcases. Analysing the average and standard deviation metrics also fails to yield an obvious pattern across the 12 samples for all six primals investigated.

As aforementioned, in the medical industry CT-derived BMD and BMC measurements are obtained using a procedure known as QCT. This remains a viable option but requires special knowledge of the area. These methods also generally involve calibrating to a special phantom. Such a phantom may be required to progress with data analysis. Similarly, it's possible that an underlying relationship may be found in the existing data by applying more complex mathematical tools.

One other possible issue may be the CT scanning parameters used. For example, with intramuscular fat determination using CT, it's critical to keep the slice width around 3mm or less. These scans were performed with 5mm wide slices.

10.5 Conclusion

It is known that CT can be used for bone mineral composition and density analysis. This study was unable to demonstrate any obvious trends that may be apparent in the CT data for carcases covering a range of ossification scores. More complex analysis such as that used in the medical industry for QCT may be required. This should be researched further for consideration before designing further trials in this space. As aforementioned, there is currently work being performed around a DEXA-derived indicator for maturity in lambs. Involving CT scanning in future trials presents a worthwhile opportunity.

11 Conclusions and Recommendations

In this project, a CT scanner was successfully installed into a purpose-built room at a dual-species abattoir. A number of red meat industry applications were successfully investigated to assess how CT technology fits into the red meat automation vision and its value proposition. This included building initial algorithms for the following applications:

- Counting of ribs and identification of the rib 1 junction directly;
- Placement of dynamic cutting path for chine removal, allowing for user-adjustable amounts of residual 'buttons' left in the loin;
- Identification of fat trim profile for entire striploins;
- Isolation of the *longissimus thoracis et lumborum* in beef cube rolls and striploins; and
- Calculation of intramuscular fat content in the *longissimus lumborum* muscle within beef striploins;

These applications present a unique value-proposition for CT technology as they cannot be achieved using standard x-ray imaging. Most significantly, commercial factors influencing these algorithms were assessed. This involved taking data and analysing it using different scan settings. The result of this is a set of specifications required of a helical CT scanner to perform these operations. Important lessons were also learnt regarding the nature of the CT data and practical implications associated with the technology.

The knowledge and algorithms developed throughout the course of this project will now be applied directly to commercial projects. This involves evaluating and/or developing CT imaging technology which is able to meet these specifications while operating reliably within an abattoir processing environment. The technology will then be applied in a commercial application, one example being a beef striploin processing machine capable of performing chine removal, fat trim and intramuscular fat grading. The algorithms and trialling methodologies developed in this project will feed into this directly.

A key opportunity area for CT technology is with respect to eating quality grading. Objective measurement of eating quality measures is vitally important to the industry, particularly with the advent of objective yield measurement systems. Moving forward, this will involve re-examining the modelling of intramuscular fat in lambs, something of high-value to the lamb industry in particular given the current lack of eating quality metrics. CT technology may also be assessed for grading of carcase maturity.

CT presents a significant opportunity to the red meat industry and can be seen as a 'quantum leap' improvement over currently available sensing technologies. This project has demonstrated this and provided a key stepping stone towards commercial implementation. Work is now commencing towards translating these outcomes into real-life, production applications in beef and lamb.

12 References

Anderson, F., Pethick, D. W., & Gardner, G. E. (2015). The correlation of intramuscular fat content between muscles of the lamb carcass and the use of computed tomography to predict intramuscular fat percentage in lambs. *Animal, 9*(7), 1239-1249.

Anderson, F., Williams, A., Boyce, M. D., Cook, J., & Gardner, G. E. (2017). THE POTENTIAL FOR DUAL ENERGY X-RAY ABSORPTIOMETRY TO PREDICT LAMB AGE. *63rd International Congress of Meat Science and Technology.* Cork, Ireland.

Bardera, A., Boada, I., Font-i-Furnols, M., & Gispert, M. (2014). Tissue quantification using expectation-maximization algorithms. *Farm Animal Imaging*, (pp. 105-111). Copenhagen.

Bonny, S. P., Pethick, D. W., Legrand, I., Wierzbicki, J., Allen, P., Farmer, L. J., . . . Gardner, G. E. (2016). Ossification score is a better indicator of maturity related changes in eating quality than animal age. *Animal, 10*(4), 718-728.

Cake, M. A., Boyce, M. D., Gardner, G. E., Hopkins, D. L., & Pethick, D. W. (2007). Genotype and gender effects on sheep limb bone growth and maturation: selection for loin depth causes bone hypotrophy. *Australian Journal of Experimental Agriculture, 46*(12), 1128-1136.

Cann, C. E. (1988). Quantitative CT for determination of bone mineral density: a review. *Radiology, 166*(2), 509-522.

Font-i-Furnols, M., Čandek-Potokar, M., Maltin, C., & Prevolnik Povše, M. (2015). Chapter 2: Intramuscular fat and marbling. In *FAIM - A handbook of reference methods for meat quality assessment* (pp. 12-21). EU: COST (European Cooperatin in Science and Technology).

Lang, T. F., Harris, S. T., & Genant, H. K. (1999). Assessment of vertebral bone mineral density using volumetric quantitative CT. *J Comput Assist Tomogr., 23*(1), 130-137.

Link, T. M., Koppers, B. B., Bauer, J., Lu, Y., & Rummeny, E. J. (2004). In vitro and in vivo spiral CT to determine bone mineral density: initial experience in patients at risk for osteoporosis. *Radiology, 231*(3), 805-811.

Navajas, E. A., Richardson, R. I., Fisher, A. V., Hyslop, J. J., Ross, D. W., Prieto, N., . . . Roehe, R. (2010). Predicting beef carcass composition using tissue weights of a primal cut assessed by computed tomography. *Animal, 4*(11), 1810-1817.

Schreiber, J. J., Anderson, P. A., & Hsu, W. K. (2014). Use of computed tomography for assessing bone mineral density. *Neurosurg Focus., 37*(1), E4.

Tomkins, N. W., Harper, G. S., Bruce, H. L., & Hunter, R. A. (2006). Effect of different post-weaning growth paths on long-term weight gain, carcass characteristics and eating quality of beef cattle. *Australian Journal of Experimental Agriculture, 46*(12), 1571-1578.

van der Sluis, I. M., de Ridder, M. A., Boot, A. M., Krenning, E. P., & de Muinck Keizer-Schrama, S. M. (2002). Reference data for bone density and body composition measured with dual energy x ray absorptiometry in white children and young adults. *Arch Dis Child, 87*, 341-347.

Appendix A – Beef Cross Sections

Source: 2006, Handbook of Australian Meat 7th Edition, AUS-MEAT Limited

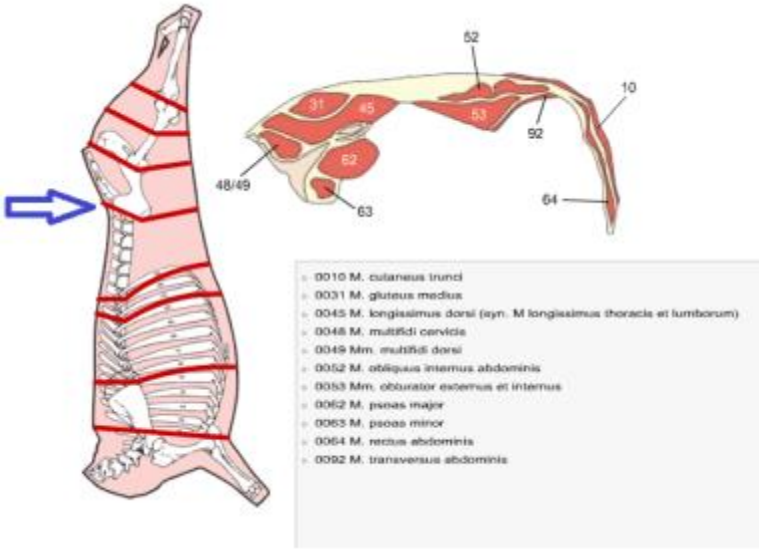

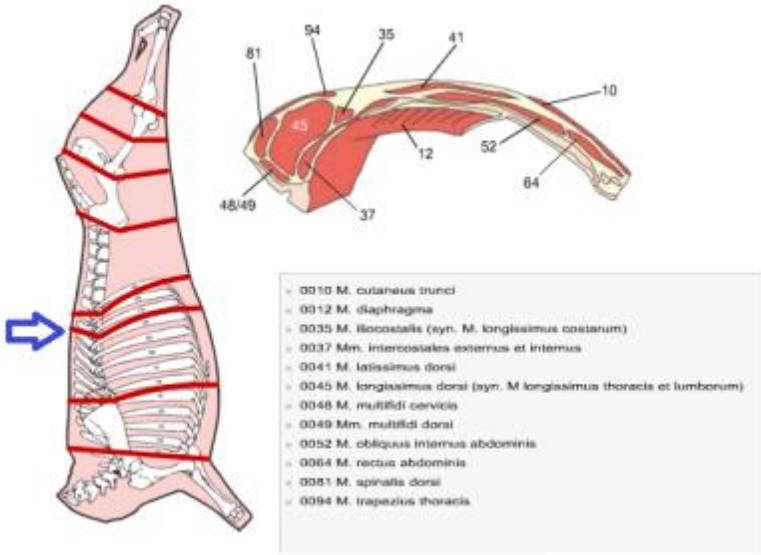

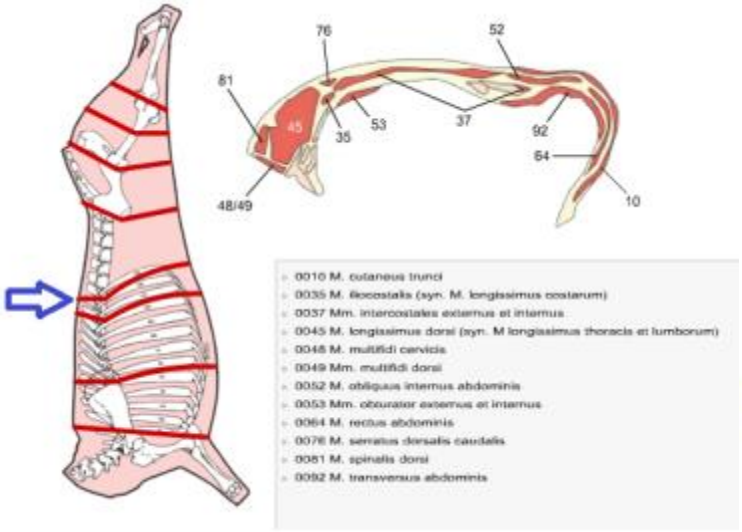

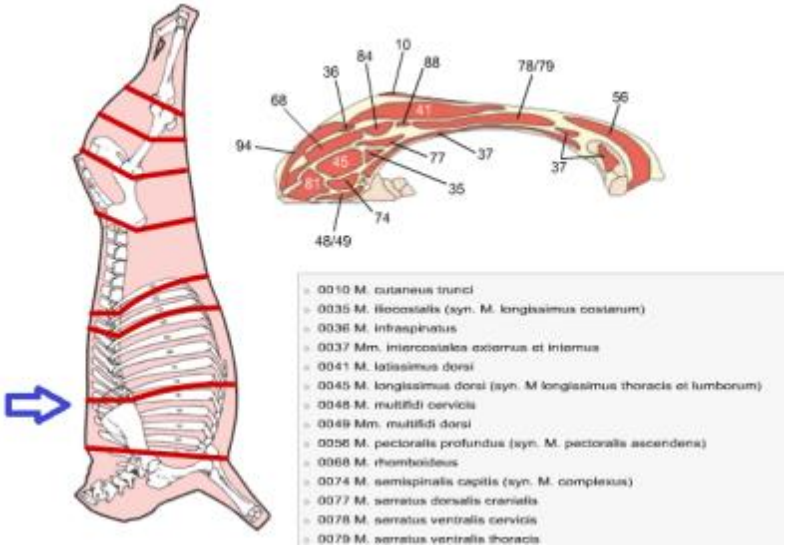

Appendix B – Histograms for high-speed CT scans

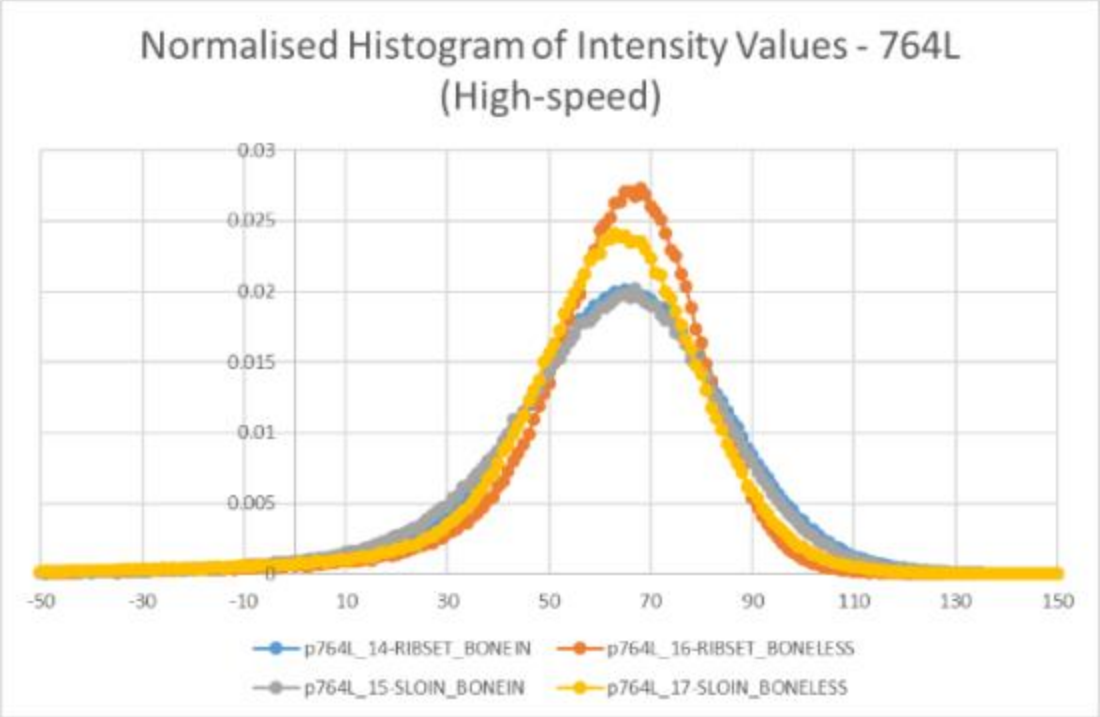

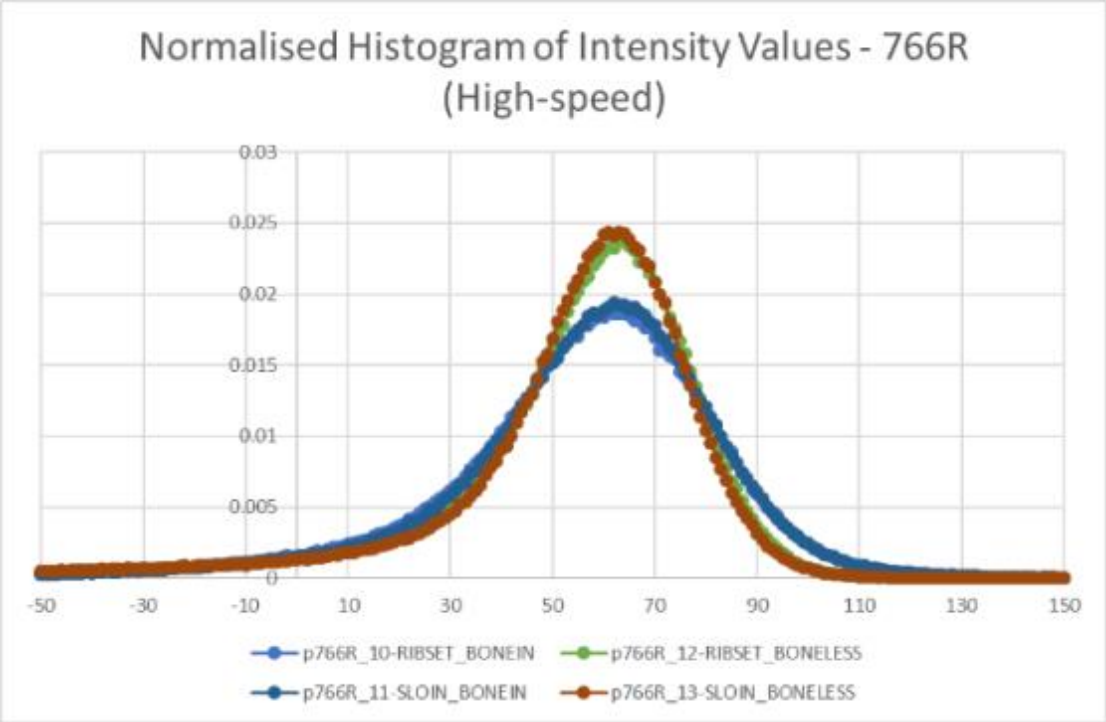

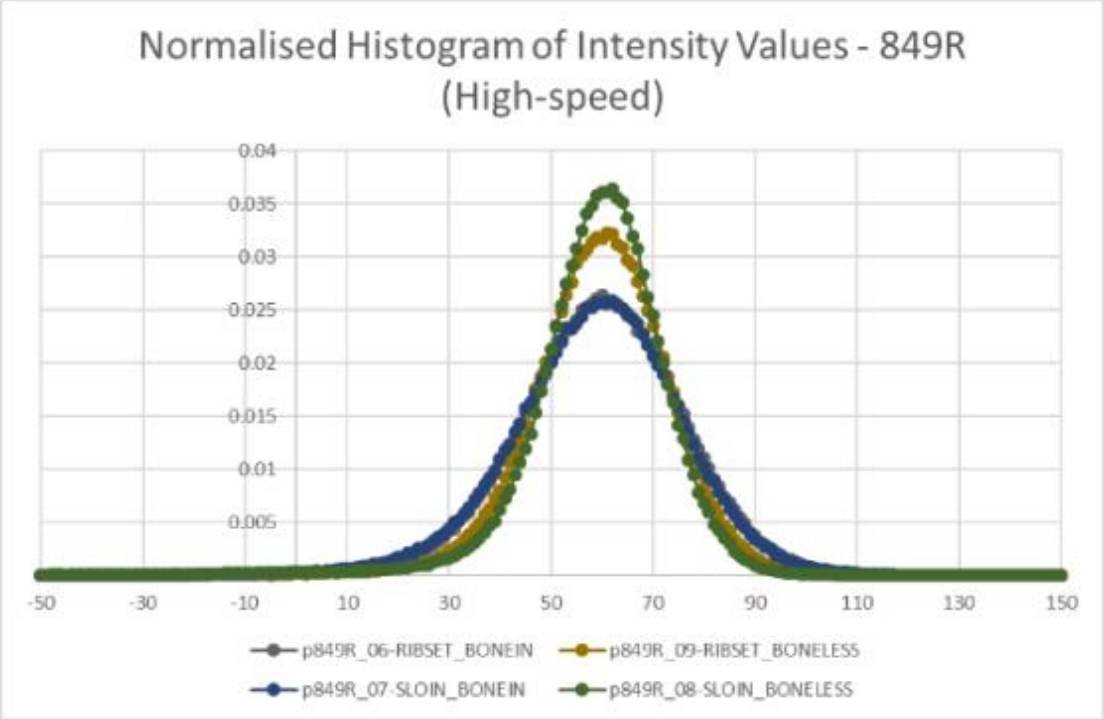
Normalised Histogram of Intensity Values - 849R (High-speed)
0.04
0.035
0.03
0.025
0.02
0.015
0.01
0.005
-50
-30
-10
10
30
50
70
90
110
130
150
p849R_06-RIBSET_BONEIN
p849R_09-RIBSET_BONELESS
p849R_07-SLOIN_BONEIN
p849R_08-SLOIN_BONELESS

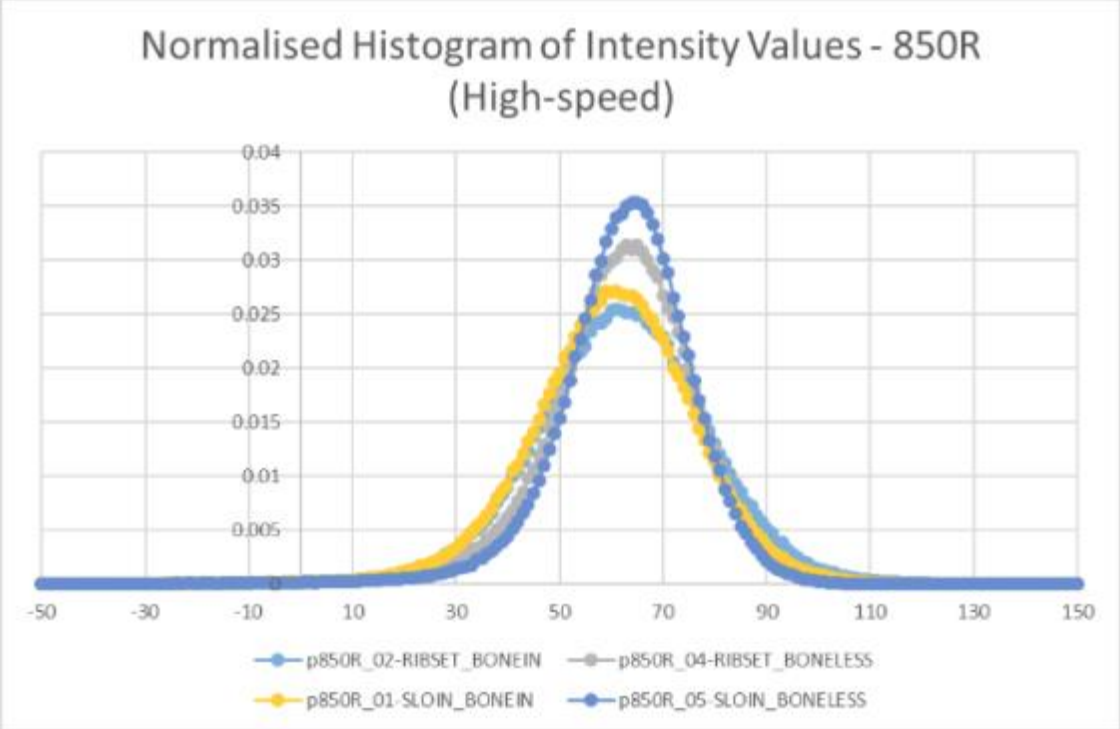
Normalised Histogram of Intensity Values - 850R (High-speed)
0.04
0.035
0.03
0.025
0.02
0.015
0.01
0.005
0
-50
-30
-10
10
30
50
70
90
110
130
150
p850R_02-RIBSET_BONEIN
p850R_04-RIBSET_BONELESS
p850R_01-SLOIN_BONEIN
p850R_05-SLOIN_BONELESS

Appendix C – Striploin Intramuscular Fat Modelling Report (F. Anderson, Murdoch University)

Predicting intramuscular fat using computed tomography in beef.

Prepared by:

F. Anderson[a], J. Cook[b], A. Williams[a], G.E. Gardner[a]

[a]School of Veterinary and Life Sciences, Murdoch University, Western Australia

[b]Scott Automation and Robotics Pty Ltd, 10 Clevedon Street, Botany, NSW

Executive Summary

The average pixel density from the computed tomography scans of the *M. longissimus lumborum* samples varied inversely to the intramuscular fat % of the muscle. Across a relatively small range of IMF% (1.8% to 14.0%), the use of the mean of all image pixels and their standard deviations provided moderate precision (High Speed: $R^2 = 0.31$, RMSE = 3.41 and High Quality: $R^2 = 0.31$, RMSE = 3.40). Using this method, there was very little difference between the High Quality and the High Speed settings. This is useful information as it will allow the CT scanning of samples at a faster rate without any loss in precision for predicting IMF%. When the slice width was increased to 3mm there was minimal change in the prediction of IMF%, however at widths above 3mm there was a more substantial loss in precision, as well as when only one slice was used. Therefore, scanning speed can be increased by using the High Speed settings, potentially with a slice width of up to 3mm. Using the High Quality scan settings across an extended range of IMF% (1.8 to 30.0%) the precision using pixel density and standard deviation was improved in both cranial ($R^2 = 0.79$, RMSE = 2.45) and caudal samples ($R^2 = 0.61$, RMSE = 4.65).

The use of pixel density information from surrounding pixels, in combination with the pixel density of a central pixel (nearest neighbour technique) improved the ability of CT to predict IMF%. The best prediction was achieved in the extended range of IMF% (1.8-30%) in the cranial samples, when the central pixel information was weighted at 10%, with surrounding pixel information weighted at 90% (High Quality settings: R^2=0.86, RMSE=2.01).

The nearest neighbour technique (10% weighting of central pixel) was superior to the visual scoring of marbling using MSA Marbling Score ($R^2 = 0.77$, RMSE = 2.52). The addition of carcass information such as HSCW in both the average of all pixels and the 'nearest neighbour technique' improved the ability of the CT to predict IMF% ($R^2 = 0.88$, RMSE = 1.87).

The intramuscular fat (IMF) % has been shown to vary along the length of the *M. longissimus lumborum* with the caudal sample 1.97 IMF% greater ($P<0.05$) than the cranial sample. Future analysis of the CT images will yield a better understanding of the variation in IMF% along the entire length of the *M. longissimus lumborum*.

Background

The use of MSA grading system is important in beef to determine estimates of eating quality. Marbling score is determined manually in the plant and reflects intramuscular fat (IMF) %. The amount of IMF% is linked to eating quality assessment for tenderness, juiciness and flavour. Marbling score is currently assessed in a number of cuts to attain an MSA marbling score. Rapid and accurate in plant assessment of IMF% would enable better input into the MSA grading system. A helical computed tomography (CT) scanner has been installed at JBS Brooklyn (Siemen's Sensation 64). A model for determining chemical fat (IMF%) in beef using the Brooklyn CT scanner would allow rapid and accurate prediction of IMF% and therefore MSA marbling score.

CT has been used to determine the IMF% content of muscle in beef, lamb and pork with varying degrees of precision. The use of CT scanning alone has been shown to have low to moderate precision for IMF% prediction. Techniques with higher precision generally rely on additional information such as carcass weight and measures of fatness, making independent and rapid analysis of muscle for IMF% generally poor. This experiment has used the CT scanner in the Brooklyn plant to scan 64 beef *M. longissimus lumborum* samples using a number of different settings. A key aim was to determine if CT scanning can accurately determine IMF%, and what aspects of image quality can be eroded yet still achieve an adequate prediction.

There is evidence to suggest that the IMF% changes along the length of the striploin (*M. longissimus lumborum*). This study determines the magnitude of this change in IMF%, with future analysis able to improve the description of these changes in IMF% along the *M. longissimus lumborum*. This would allow for adjustments to be made to the weighting of the MSA marbling scores taken along the length of this muscle to improve the accuracy of the eating quality assessment of this muscle.

A CT scanner at the Brooklyn plant was used to scan 64 striploin samples. A 6cm section at the cranial and caudal ends of these striploins was then removed, the *M. longissimus lumborum* isolated and the IMF% chemically determined. The ability of the CT scanner to predict IMF% was determined, with the impact that scanner specifications have on prediction precision also investigated. The specific aim was to determine the most appropriate scan settings and slice width to accurately predict IMF% at an acceptable speed. This study describes the potential for determining the IMF% of beef using computed tomography. It also assesses the most rapid and precise methods for determining IMF%. It also investigates and determines how the IMF% of the striploin alters from the cranial to the caudal ends.

Method

Striploins were obtained from 32 steers and 32 cows processed at the Brooklyn plant across a range of Meat Standards Australia (MSA) marbling scores, hot carcass weights (HSCW) and ossification scores. The hot standard carcass weight (HSCW), striploin lengths, ossification score, and MSA Marbling Scores are reported in Table 1. Following slaughter, striploins were dissected to remove the *M. longissimus lumborum* in isolation and the length of this muscle was measured.

Table 1. Carcass data including mean ± standard deviation, minimum and maximum values for shortloin length, hot standard carcass weight (kg), hump height (mm), eye muscle area (cm^2), ossification score, and Meat Standards Australia (MSA) marbling score.

	Shortloin length (mm)	Hot standard carcass weight (kg)	Hump height (mm)	Eye muscle area (cm2)	Ossification score	MSA Marbling Score
Mean ±SD	452 ± 31.9	318.6 ± 56.3	50.2 ± 14.4	73.5 ± 10.1	259.1 ± 172.2	425.5 ± 253.7
Min, Max	390, 555	224.0, 443.0	20.0, 85.0	40.0, 94.0	130.0, 590.0	253.7, 1120.0

Prior to CT scanning the cranial and caudal 6 centimetres of the *M. longissimus lumborum* were removed and trimmed of fat. The samples were then placed on the scanning table as shown in Figure 1. The scan settings used were chosen to represent settings compatible with either fast processing speed and therefore lower image quality (High Speed) or slower processing speed but higher image quality (High Quality).

Figure 1. Beef striploin, and the sample prepared for computed tomography scanning adjacent to it.

Immediately following scanning the cranial and caudal samples were vacuum packed and frozen, before being sent to Murdoch University for IMF% determination. Samples were freeze dried using a ScanVac CoolSafe™ freeze drier (Labogene™, Vassinerod, Denmark) and IMF % of each muscle sample determined using a near infrared procedure (NIR). NIR measurements were taken using a Spectro Star 2400 and all samples were subsequently calibrated against chloroform solvent extraction as detailed by (Perry *et al.* 2001).

Image J was used to process the images with pixel information obtained from all slices. CT images were captured consecutively along the length of the muscle sample with a voxel depth of 0.6mm. The CT image information was used in a variety of ways to determine the impact of image analysis on IMF% prediction:

1. The impact of voxel depth using mean and standard deviation of all pixels.
2. The use of thresholding techniques.

3. The impact of using surrounding pixel information at various weightings (nearest neighbour technique).

Methods 1 and 3 also determined the impact htat using high speed and high quality setting had on IMF% prediction.

Voxel depth

To determine the impact that voxel depth had on IMF% prediction, for each muscle sample (both cranial and caudal ends) the image sets were reconstructed to obtain equivalent images with voxel depth of 3mm or 6mm. This was done by taking the mean of 5 (for a 3mm reconstruction) or 10 (for a 6mm reconstruction) matching voxels within adjacent images which were originally captured at 0.6mm voxel depths. This resulted in 3 separate image-sets for each muscle sample, one at 0.6mm, one at 3mm, and one at 6mm voxel depth. Within each image-set the mean voxel density and standard deviation of voxel densities was then calculated using all images with that image-set. Lastly a single image was selected from each of the 0.6mm image-sets that corresponded to the mid-point of the muscle sample. The mean voxel density and standard deviation of voxel densities was calculated for this single image. Thus mean voxel density and standard deviation of voxel densities was available for each muscle sample for a variety of different image acquisition methods, including high speed or high quality scanning.

The pixel density information and standard deviation of pixel density from the different image acquisition methods was used to predict chemical IMF% in a general linear model (SAS Version 9.1, SAS Institute, Cary, NC, USA). Within each model, the mean voxel density and standard deviation of voxel densities was used as a covariate. Each model was then tested with hot carcass weight (HCWT) as an additional covariate. Thus separate models were constructed for a variety of different image acquisition methods, including high speed or high quality scanning, with multiple consecutive images of voxel depths of 0.6, 3, or 6mm, or a single image captured at 0.6mm.

Thresholding

Using thresholding to determine the number of fat and lean pixels, other parameters were established to investigate techniques for predicting IMF%. A pixel was defined as being fat if its density was less than 970 units which is the average pixel density of fat in the samples. Based on the number of fat and lean pixels determined by thresholding the following were parameters were calculated:

- Ratio of number of fat:lean pixels.
- Average density of fat pixels.
- Average density of fat pixels.
- Percentage weight of fat in the sample – calculated by multiplying the pixels categorised as fat or lean by the density of each tissue, summing and dividing by the calculated total tissue weight.

A correlation matrix was constructed between the above variables and the average and standard deviation of all pixels within a sample. The variables with lower correlations with average and standard deviation of pixel density were include in a general linear model to determine if they offered improved precision of IMF% prediction. Additionally these variables were included individually in a general linear model to determine their precision of prediction.

Nearest neighbour technique

A third method was used to calculate pixel density values based on the weighted impact of the surrounding pixel densities (nearest neighbour technique). For example if the pixel was weighted at 100%, then only the pixel information was used, compared to a weighting of 50% where the original pixel information was weighted at 50%, with the surrounding pixel information weighted at 50% to calculate a new pixel density. A range of weightings were used to calculate pixel density: 75, 50, 25 and 10%. The mean and standard deviation of all calculated pixel densities from every slice for each sample was then used in general linear models as previously described to predict IMF%. This was repeated for both the High Speed and High Quality CT scan settings.

A general linear model used MSA grading score as a covariate to predict IMF% enabling the comparison of the CT analysis methods with the current industry method.

Results

Raw data distribution

Initially, a total 125 samples were analysed for IMF% with the raw mean ± SD of IMF% being 8.4 ± 6.3 (see Table 2). The mean±SD, minimum, and maximum for pixel average density and pixel standard deviation for the 101 images are shown in Table 3. The average pixel density for each sample, and the standard deviation of the pixels in these samples are shown in Figure 2 and Figure 3.

Table 2. Intramuscular fat % of the cranial and caudal 6 centimetre sections of the *M. longissimus lumboru*m in beef.

	Number of samples	mean ± SD	min	max
Cranial samples	51	5.19 ± 2.68	1.77	14.1
Caudal samples	50	6.45 ± 2.90	2.4	14.
All samples	101	5.82 ± 2.85	1.77	14.12

Table 3. Mean ± SD, maximum and minimum of sample average pixel density and their standard deviations for CT images using all slices (0.6mm voxels), all slices with 3mm reconstructed voxels, all slices 6 mm reconstructed voxels and 1 slice (0.6mm voxels).

	Pixel density		Standard deviation of pixels	
	Mean ± SD	Min, Max	Mean ± SD	Max, Min
All slices: 0.6 mm voxels	1039.6 ± 11.88	1006.8, 1062.7	103.6 ± 8.9	82.8, 130.6
All slices: 3mm reconstructed voxels	1034.2 ± 10.6	1014.7, 1055.7	113.2 ± 6.1	97.8, 128.5
All slices: 6mm reconstructed voxels	1021.7 ± 11.0	998.4, 1046.7	128.0 ± 6.3	108.3, 146.5
1 slice; 0.6 mm voxels	1046.1 ± 17.5	876.5, 1071.6	96.7 ± 13.1	74.3, 163.7

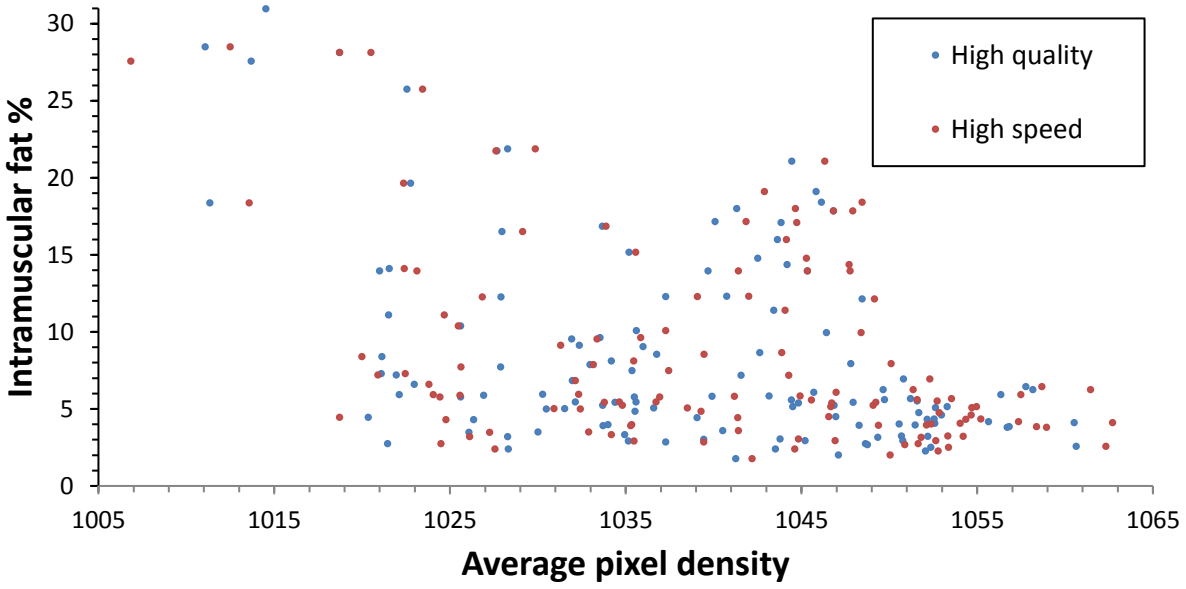

Figure 2. Raw data of the intramuscular fat % in beef of the *M. longissimus lumborum* as it relates to average computed tomography pixel density of all samples pixels from all slices at 0.6mm voxels.

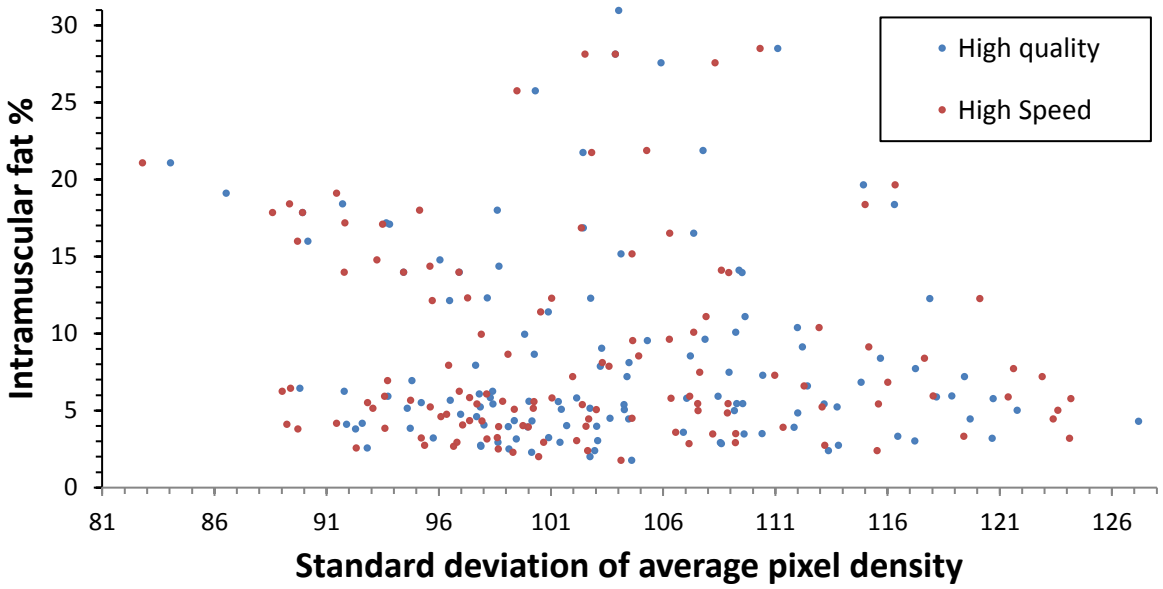

Figure 3. Intramuscular fat % in beef of the *M. longissimus lumborum* as it relates to standard deviation of pixel density of all sample pixels from all slices at 0.6mm voxels.

IMF% positional analysis

The IMF% varied between the cranial and caudal ends ($P<0.05$), with the average IMF% of the caudal end 1.97 IMF% greater than the cranial sample in the extended range of IMF samples (Table 7). The IMF % of the cranial and caudal samples were highly correlated (correlation coefficient 0.96)

Prediction of IMF%

This analysis was initially performed on 52 samples with an IMF % range of 1.8% to 14.1%, with the results reported in parts 1 to 4 of "Prediction of IMF%" below. After obtaining the new samples that extended the data range we then repeated this analysis with the results reported in part 5 below.

Part 1: Use of all pixels and carcass information

There was a negative linear relationship ($P<0.01$) between IMF% and CT pixel density. The IMF% was initially predicted using all pixels from all slices and the standard deviation of these pixels. The ability of CT to predict IMF% was moderate and similar for both High Quality (Model 4, Table 4: $R^2 = 0.31$, RMSE = 2.40) and High Speed (Model 5, Table 4: $R^2 = 0.31$, RMSE = 2.41). The inclusion of hot standard carcass weight (HSCW) in the model improved the ability to predict IMF% in both High Speed and Quality scans (Table 4, Models 6 and 7). However, this was still not as high as the ability of MSA Marbling Score to predict IMF%, with $R^2 = 0.50$, RMSE = 2.0 (Table 4, Model 1). The use of HSCW alone offers relatively poor prediction of IMF% , with $R^2 = 0.19$, RMSE = 2.56 (Table 4, Model 2). The inclusion of other parameters such as ossification score and eye muscle area did not improve the ability to predict IMF% in either the High Speed or High or High Quality Scans.

Part 2: Slice reconstruction

When slices were reconstructed at 3mm voxels the ability to predict IMF% was very similar to when every slice was used (0.6mm voxel widths) for both High Speed (Model 8, Table 4: $R^2 = 0.31$, RMSE = 2.42) and High Quality (Model 9, Table 4: $R^2 = 0.32$, RMSE = 2.39). This was moderately reduced

when the slice widths were 6mm, with the High Speed settings resulting in the greatest decrease in the ability to predict IMF% (Model 11, Table 4: R^2=0.24, RMSE = 2.5) compared to the High quality settings (Model 10, Table 4: R^2=0.27, RMSE = 2.47). As would be expected the ability to predict IMF% was further reduced when the information from only one slice was included in the model and was poor for both High Quality (Model 12, Table 4: R^2=0.21, RMSE = 2.57) and High Speed settings (Model 13, Table 4: R^2=0.17, RMSE = 2.62).

Table 4. F-values, coefficient, intercept, coefficient of determination (R-square), and root mean square error (RMSE) for models predicting intramuscular fat % in beef using average computed tomography pixel density, standard deviation, hot carcass weight, and Meat Standards of Australia Marbling Score (IMF range 1.77% to 14.1%).

	Model 1	**Model 2**	**Model 3**	**Model 4**	**Model 5**	**Model 6**	**Model 7**	**Model 8**	**Model 9**	**Model 10**	**Model 11**	**Model 12**	**Model 13**
				All slices: 0.6mm voxels				**All slices: 3mm reconstructed voxels**		**All slices: 6mm reconstructed voxels**		**One slice: 0.6mm voxel**	
Scan Type	**NA**	**NA**	**NA**	**High Quality**	**High Speed**	**High Quality**	**High Speed**	**High Quality**	**High Speed**	**High Quality**	**High Speed**	**High Quality**	**High Speed**
						F Values							
Average pixel density	-	-	-	42.29*	39.71*	46.75*	43.27*	40.2*	42.82*	35.76*	30.99*	25.67*	20.02*
Standard Deviation	-	-	-	24.78*	24.17*	20.89*	19.85*	21.14*	24.39*	18.42*	15.81*	18.86*	14.01*
HCWT	-	47.25*	1.69	-	-	32.29*	31.1*	-	-	-	-	-	-
MSA Marbling Score	100.36*	-	123.3*	-	-	-	-	-	-	-	-	-	-
						Coefficients and intercept							
Average pixel density	-	-	-	-0.28	-0.28	-0.26	-0.26	-0.25	-0.27	-0.2	-0.19	-0.2	-0.17
Standard Deviation	-	-	-	-0.29	-0.27	-0.24	-0.22	-0.32	-0.36	-0.27	-0.238	-0.17	-0.14
HSCW	-	0.03	0.004	-	-	0.024	0.024	-	-	-	-	-	-
MSA Marbling score	0.01	-	0.01	-	-	-	-	-	-	-	-	-	-
Intercept	1.7	-1.65	0.62	326.9	327.2	290.86	289.86	305.94	326.69	246.39	227.86	230.82	198.28
						Precision estimates							
R^2	0.50	0.19	0.50	0.31	0.31	0.48	0.47	0.30	0.31	0.27	0.24	0.21	0.17
RMSE	2.02	2.56	2.02	2.40	2.41	2.09	2.1	2.42	2.39	2.47	2.5	2.57	2.62

* P<0.01

MSA: Meat Standards Australia; HSCW: Hot Standard Carcass Weight

Part 3: Use of surrounding pixels

When pixel density was calculated using the nearest neighbour technique (use of surrounding pixel information) the prediction of IMF% varied depending on the original pixel weighting. As the weighing of the central pixel was reduced, the prediction of IMF% improved (see Figure 4). Hence the best prediction of IMF% were those achieved at the High Quality scan settings with a 10% central-pixel weighting (Model 26, Table 5: R^2=0.44, RMSE=2.15).

There was a difference between the ability of High Quality and High Speed scan settings to predict IMF%, with High Quality scan settings having a small advantage over the High Speed settings (Table 5). The difference in R^2 remained relatively constant, with the High quality settings 0.01 greater than the High Speed settings.

When HSCW was included in the model along with mean pixel density and standard deviation, the prediction of IMF% improved. For example, at the High Quality settings at 10% pixel weighting the R^2 was greater with inclusion of HSCW (Model 28, Table 5: R^2=0.56, RMSE=1.95) compared to without (Model 26, Table 5: R^2=0.34, RMSE=2.35).

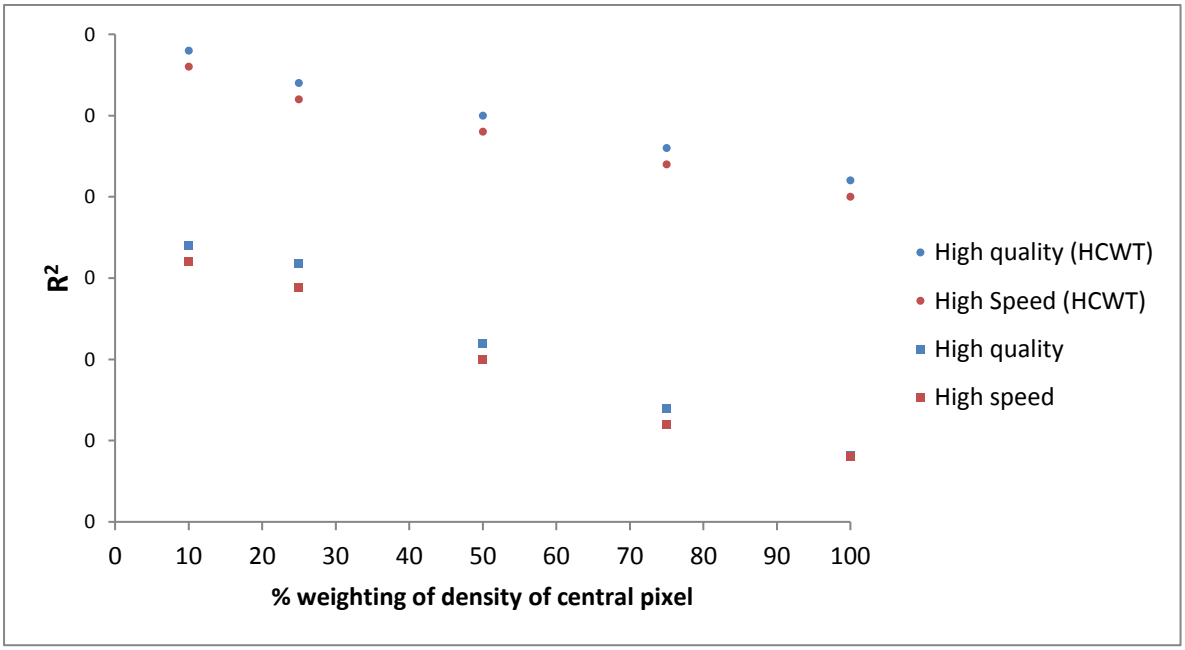

Figure 4. R squared of CT prediction of beef IMF% as it related to the weighting of the density of the central pixel at High Quality and High Speed settings, with and without inclusion of hot standard carcass weight in the model.

Table 5. F-values, coefficient, intercept, coefficient of determination (R-square), and root mean square error (RMSE) for models predicting intramuscular fat % in beef using average computed tomography pixel density, standard deviation, hot carcass weight with 75, 50, 25 and 10% weighting of the central pixel. (IMF range 1.77% to 14.1%)

	Model 14	**Model 15**	**Model 16**	**Model 17**	**Model 18**	**Model 19**	**Model 20**	**Model 21**	**Model 22**	**Model 23**	**Model 24**	**Model 25**	**Model 26**	**Model 27**	**Model 28**	**Model 29**
	75% weighing of central pixel				**50% weighing of central pixel**				**25% weighing of central pixel**				**10% weighing of central pixel**			
Scan Type	**High Quality**	**High Speed**	**High Quality**	**High Speed**	**High Quality**	**High Speed**	**High Quality**	**High Speed**	**High Quality**	**High Speed**	**High Quality**	**High Speed**	**High Quality**	**High Speed**	**High Quality**	**High Speed**
	F Values															
Average pixel density	49.1*	47.0*	53.03*	48.63*	59.06*	55.93*	60.8*	55.48*	73.45*	67.47*	71.77*	64.03*	78.22*	73.7*	75.4*	68.97*
Standard Deviation	31.31*	31.3*	26.1*	24.65*	42.01*	39.47*	34.1*	30.24*	54.81*	50.73*	42.5*	37.76*	63.08*	57.07*	48.26*	42.24*
HCWT	-	-	31.17*	28.8*	-	-	25.58*	26.81*	-	-	25.98*	24.11*	-	-	24.48	22.91
	Coefficients and intercept															
Average pixel density	-0.29	-0.30	-0.27	-0.27	-0.25	-0.31	-0.28	-0.28	-0.33	-0.33	-0.3	-0.3	-0.34	-0.34	-0.3	-0.3
Standard Deviation	-0.34	-0.33	-0.28	-0.26	-0.32	-0.39	-0.34	-0.31	-0.48	-0.45	-0.4	-0.36	-0.52	-0.47	-0.43	-0.38
HSCW	-	-	0.02	0.02	-	-	0.02	0.02	-	-	0.02	0.02	-	-	0.02	0.02
Intercept	344.5	349.1	305.14	305.84	375.3	373.8	330.1	325.2	405.7	398	354.4	345.3	413.7	406.5	361.8	353.2
	Precision estimates															
R^2	0.34	0.33	0.5	0.49	0.38	0.37	0.52	0.51	0.43	0.41	0.54	0.53	0.44	0.43	0.56	0.55
RMSE	2.35	2.35	2.05	2.07	2.28	2.28	2.01	2.03	2.18	2.21	1.95	1.98	2.15	2.17	1.93	1.95

* P<0.01

HSCW: Hot Standard Carcass Weight

Part 4: Thresholding techniques

Pixels were categorised as being fat or lean as previously described in the methods, with a number of parameters used to describe proportions of fat and lean or weight of fat and lean in each sample. A correlation matrix (Table 6) was used to highlight which of these calculated measures were highly correlated with the average and standard deviation of all pixel densities and therefore would offer little extra precision when predicting IMF% beyond that already described. Importantly, those that had low correlations were more likely to provide independent description of the variance in IMF%. These variables were therefore tested in general linear models predicting IMF% along with the mean and standard deviation of all pixel values. In this case average lean pixel density was used, however it added no further improvement to the model and on its own had very poor precision for predicting IMF% (R^2= 0.14, RMSE =2.66).

Table 6. Simple correlation coefficients of the computer tomography derived parameters used to determine IMF% in beef: mean and standard deviation of all pixel densities, ratio of fat:lean pixels, average density of fat pixels, average density of lean pixels and percentage weight of fat.

	Mean of all pixel densities	Standard deviation of all pixel densities	Ratio of number fat:lean pixels	Average density of fat pixels	Average density of lean pixels	Percentage weight of fat
Mean of all pixel densities	1	-0.87	0.945	0.93	-0.54	0.93
Standard deviation of all pixel densities	-	1	-0.89	-0.64	0.28	-0.87
Ratio of number fat:lean pixels	-	-	1	0.79	-0.66	0.99
Average density of fat pixels	-	-	-	1	-0.56	0.79
Average density of lean pixels	-	-	-	-	1	-0.68
Percentage weight of fat	-	-	-	-	-	1

Part 5. Extended IMF% range.

After analysing the initial samples with a more limited IMF% range, additional IMF% samples were obtained and included (IMF% 1.8% to 31%), with mean, standard deviation, maximum and minimum reported in Table 7.

Table 7. Intramuscular fat % of the cranial and caudal 6 centimetre sections of the *M. longissimus lumboru*m in beef for the extended range of intramuscular fat % (1.8 to 31%).

	Number of samples	mean ± SD	min	max
Cranial samples	63	7.32 ± 5.2	1.8	21.1
Caudal samples	62	9.46 ± 7.1	2.4	31.0
All samples	125	8.40 ± 6.3	1.8	31.0

Table 8. F-values, coefficient, intercept, coefficient of determination (R-square), and root mean square error (RMSE) for models predicting intramuscular fat % in beef using the High Quality settings and MSA marbling score, average computed tomography pixel density, standard deviation, hot carcass weight with 100 and 10% weighting of the central pixel in cranial and caudal end of the *M.Longissiums lumborum* (IMF% range 1.8% to 30.0%).

	Model 30	**Model 31**	**Model 32**	**Model 33**	**Model 34**	**Model 35**	**Model 36**	**Model 37**	**Model 38**	**Model 39**	**Model 40**
				100% weighing of original pixel				**10% weighing of original pixel**			
Cranial v caudal sample from *M.longissimus lumborum*	**Cranial**	**Cranial**	**Cranial**	**Cranial**	**Caudal**	**Cranial**	**Caudal**	**Cranial**	**Caudal**	**Cranial**	**Caudal**
						F Values					
Average pixel density	-	-	-	160.5*	75.9*	140*	76.9*	197.2*	108.5*	185*	105.5*
Standard Deviation	-	-	-	1176.4*	45.2*	102.6*	31.6*	356*	148.8*	217.2*	90.7*
HCWT	-	56.66*	1.0	-	-	14.3*	20.7*	-	-	10.4*	8.59*
MSA marbling score	208.9*	-	107.1*	-	-	-	-	-	-	-	-
						Coefficients and intercepts					
Average pixel density	-	-	-	-0.7	-0.67	-0.63	-0.60	-0.54	-0.58	-0.51	-0.55
Standard Deviation	-	-	-	-0.98	-0.69	-0.81	-0.53	-0.93	-1.17	-0.82	-1.00
HSCW	-	0.06	0.01	-	-	0.023	0.04	-	-	0.02	0.03
MSA marbling score	0.018	-	0.02	-	-	-	-	-	-	-	-
Intercept	-0.33	-11.79	-2.23	832.2	774.4	735.96	670.8	674.1	738.7	622.2	679.3
						Precision estimates					
R^2	0.77	0.32	0.78	0.79	0.61	0.83	0.71	0.86	0.77	0.88	0.80
RMSE	2.52	5.34	2.52	2.45	4.65	2.22	4.02	2.01	3.56	1.87	3.35

* P<0.01

HSCW: Hot Standard Carcass Weight

Using pixel density and standard deviation from the CT images, the nearest neighbour method (10% weighting on the central pixel) yielded the greatest precision in both the cranial (Model 37, Table 8: R^2=0.86, RMSE=2.01) and caudal (Model 38, Table 8: R^2=0.77, RMSE=3.56) samples compared to using only the central pixel information (i.e the equivalent of 100% central pixel weighting). The nearest neighbour method within the cranial samples had superior precision to using MSA marbling score (Model 30, Table 8: R^2=0.77, RMSE=2.52) to predict IMF.

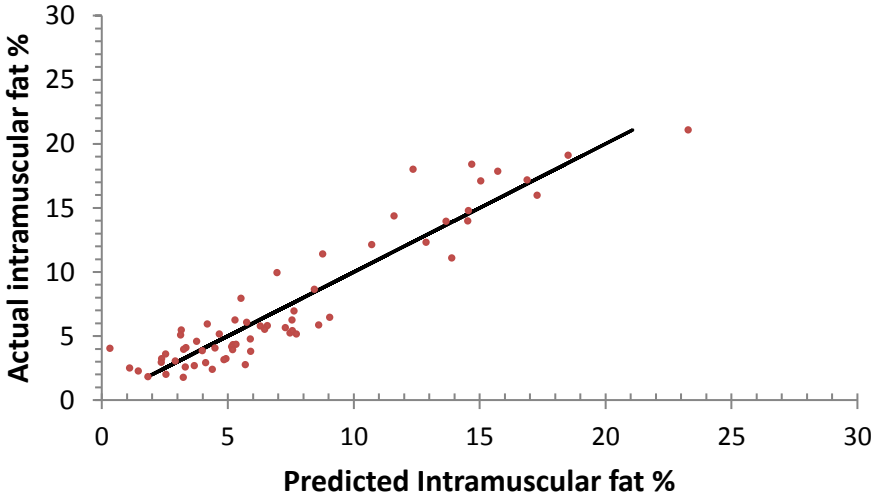

Figure 5. The prediction of intramuscular fat % in the cranial 6cm samples of beef *M. longissimus lumborum* using computed tomography and the nearest neighbour technique (10% weighting of central pixel) and hot standard carcass weight. Solid line represents perfect prediction, with red dots representing residuals to this relationship.

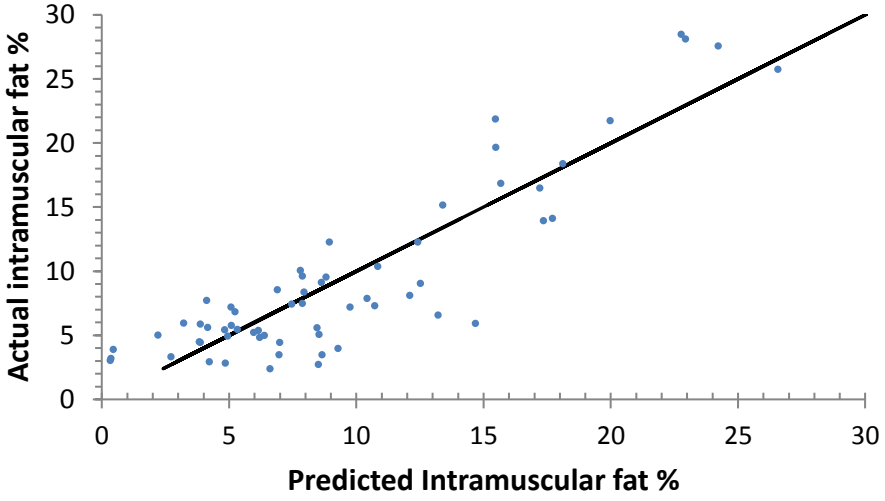

Figure 6. The prediction of intramuscular fat % in the caudal 6cm samples of beef *M. longissimus lumborum* using computed tomography and nearest neighbour technique (10% weighting of central pixel) and hot standard carcass weight. Solid line represents perfect prediction, with blue dots representing residuals to this relationship.

The best precision was achieved by inclusion of HCWT to the nearest neighbour models for both cranial (Model 39, Table 8; Figure 5: R^2=0.88, RMSE=1.87) and caudal samples (Model 40, Table 8; Figure 6: R^2=0.80, RMSE=3.35).

Discussion and conclusions

Intramuscular fat %.

The cranial portion of the *M. longissimus lumborum* was significantly lower in IMF% than the caudal portion: 5.19 ± 2.68 compared to 6.45 ± 2.90. Given the two points sampled we cannot determine whether this change occurs in a linear fashion along the length of the *M. longissimus lumborum*, however further analysis of changing CT density across consecutive images may provide some indication. This lower IMF% in the cranial region of the muscle is in contrast to the predicted eating quality scores of this region using the MSA model, which are consistently higher than the caudal region. Intramuscular fat% is of course only one of multiple components that contribute to the eating quality of a muscle.

The ability to predict intramuscular fat %

High v low scan settings:

The ability of the CT scanner to predict IMF% in the *M. longissimus lumborum* using average pixel density and standard deviation of all pixels at 0.6mm slices was moderate (see Table 4, Models 4 & 5) and similar for both the High Speed and High quality Scan protocols. The lack of improvement in the ability to predict IMF using the high quality settings suggests that future scanning protocols can make use of the high speed settings to reduce scanning times. This will be further investigated under scenarios where greater voxel depths are employed, however this may imply that similar accuracies can be achieved by further lowering the exposure time enabling greater product through-put in future commercial prototypes.

The impact of voxel width on the ability to predict IMF%.

When using computed tomography to predict IMF%, the best prediction was obtained when using average pixel density and standard deviation from all slices (voxel width 0.6mm). When images were reconstructed into voxel widths of 6mm the prediction of IMF% using average pixel density and standard deviation was reduced, however at voxel widths of 3mm this reduction in precision was only small. This indicates that image capture using larger voxels will still provide good prediction of IMF%, an advantage due to decreased image processing times.

Using other data

In contrast to the CT methods the industry standard MSA Marbling score provided the most precise prediction of IMF%. However if data such as HSCW was included in the CT pixel density/standard deviation models then the ability to predict IMF improved markedly, approaching similar levels of precision to the visual scoring system. By contrast when HSCW was included with MSA marbling score there was no further improvement in the prediction of IMF%.

Therefore it appears that a combination of CT scanning and HSCW could be used to predict IMF%, with levels of precision approaching that of the visual MSA Marbling score. However the advantage is that the CT method is likely to be more repeatable compared to a human grader, and could probably be used on "Hot" carcasses and therefore employed sooner after processing. Both of these factors require further investigation in future experiments.

One factor worth noting is the processing time taken to determine average pixel values and pixel standard deviations for each muscle sampled. Conversion of the 100 sets of images into the corresponding numbers currently takes several hours. Carefully written Fortran code is likely to overcome this issue, but it will be required prior to delivery of a commercial prototype.

The inclusion of surrounding pixels to calculate adjusted pixel density and the impact on IMF% prediction. The use of information from surrounding pixels in an image, 'nearest neighbour technique', improved the ability of CT to predict IMF%. As the weighting of the central pixel was reduced from 100% down to 10% the R^2 increased from 0.31 (High Speed and High Quality) to 0.44 (High Quality settings) and 0.43 (High Speed settings). Across the data range in this study, and when using the nearest neighbour technique to predict IMF%, there was little difference between the High and Low Quality settings. Therefore as a 'stand-alone' technique for predicting IMF% from CT images, the nearest neighbour method has a significant advantage over using only the raw pixel values (i.e 100% weighting on the central pixel), and the scanning settings (High Speed versus High Quality) make little difference.

When this same method was applied to the larger dataset containing samples that extended across the range of IMF%, the nearest neighbour (10% weighting on the central pixel) prediction of IMF was still the best performed method. Furthermore, the precision of the IMF% prediction in cranial samples using the nearest neighbour technique (10% central pixel weighting) was superior when compared to the visual MSA marbling score. Across all image analysis techniques the precision of prediction in the cranial samples was better than in the caudal samples. Given the small size of the data set, this could well be a reflection of random sampling error as opposed to some systematic increase in variance in the caudal region, therefore we will not over-interpret this result at this point.

When HCWT was included in the models, the accuracy of IMF% prediction was improved. Using the nearest neighbour technique in the extended range of IMF% was superior to using MSA marbling score. However, ideally the IMF% method should rely on direct information, rather than phenotypically correlated information from other traits such as carcase weight. This is because future breeding values need to control these traits independently, thus predicting IMF% using carcase weight limits the capacity to select for a high carcase weight and high IMF% animal independently. None-the-less, as the level of paying producers for the phenotype delivered, HCWT is likely to be useful for further improving the precision of this feedback.

These results indicate the potential for CT technology to be used to predict IMF% and therefore eating quality in the MSA grading system. We can speculate that the use of CT will provide a more repeatable and accurate result in a commercial setting than the visual MSA marble score which is likely to vary between graders and within graders between days due to human error. Thus in a commercial setting where MSA marbling score is assessed by a range of graders of varied skill levels and at greater speed, the accuracy of IMF% prediction using MSA marbling score may diminish. Furthermore, there is anecdotal evidence that the visual grading system loses precision/accuracy at lower IMF% levels, a limitation which may be less likely to be encountered by using CT. To evaluate this in more detail a greater number of samples across a large range in IMF% need to be analysed by a range of graders in a commercial setting.

Image acquisition issues.

One peripheral observation was that there appears to be an image defect in the images acquired, whereby the bottom portion of the images on the upper shelf and the upper portion of the images on the bottom shelf of the CT scanning frame had lower densities, as depicted in Figure 7. This phenomenon was not due to fat being present on the outside of the samples as they were trimmed of subcutaneous and intermuscular fat. The reason for this irregularity and the potential impact on the results is difficult to ascertain. At a population level, the effect is likely to be structured across all samples scanned, thus producing a fixed effect across all samples. However, within an image this may have affected the association with chemical IMF% thus influencing precision. Simple thresholding of the lower density pixels is not a suitable solution as the variation in pixels density required to determine IMF% in the remainder of the image will be lost. Further investigation is required to understand this effect.

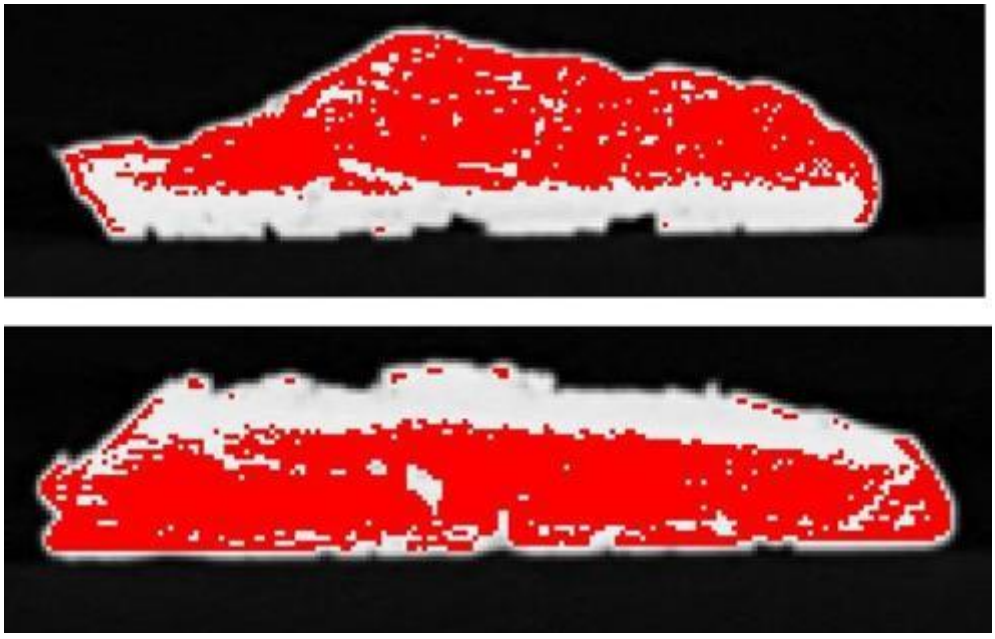

Figure 7. Computer tomography images showing low density pixels (<1077 units) in white.

Conclusions and future analysis

The use of CT to determine IMF% in a commercial setting is a realistic proposition for the future. The precision to which CT predicts IMF% in this data set is better than the current industry standard which utilises MSA marbling score. CT offers a rapid and moderately precise method for prediction of IMF%. The use of CT with the settings described in this report predict IMF% in the *M. longissimus lumborum* with moderate to high precision, with the 'nearest neighbour technique' using the High Quality settings offering the best prediction. Future investigations may involve alternative methods of data analysis such as a 3 dimensional nearest neighbour calculation or the use of alternative scan settings to improve precision and or speed of scanning.

The precision and accuracy of IMF% prediction under commercial grading conditions, where grading is performed at higher speeds and the technique may be affected by variation is grader accuracy. Future work could focus on extending the range of IMF/MSA marbling score of samples to determine the precision of IMF% prediction across this extended range in a commercial setting for both CT and MSA marbling score.

The methods used to predict IMF% needs validation in hot samples, and transportability within a larger data set also requires investigation.

Future work will need to establish whether adjustments to pixel density information is necessary due to the image acquisition irregularities previously described. This may require the scanning of a phantom in various locations within the CT scanner to determine the impact that sample placement in the CT machine has on image acquisition.